Gamma-Ray Burst Afterglows: Constraining Physical Parameters and Fireball Model Assumptions

Thesis by

Sarah Anne Yost

In Partial Fulfillment of the Requirements

for the Degree of

Doctor of Philosophy

California Institute of Technology

Pasadena, California

2004

(Submitted August 29, 2003)

Abstract

Gamma-ray bursts (GRBs) are the most luminous events in the high-energy sky. Occurring at cosmological distances, they are cataclysmic events presumed to be associated with the endpoints of massive stars' lives. They are produced by relativistic ejecta. As the ejecta encounters the surrounding medium it slows and emits lower-energy emission known as the GRB afterglow. The evolution of the shock in this phase depends upon the medium encountered as well as on such basic parameters of the event as energy and collimation. Afterglow studies can shed light upon the physics of relativistic shocks and the GRB environment(s), providing indirect clues to the progenitors. These parameters can be determined by fitting afterglow data sets to a model of the event, here, the fireball model. If the model assumptions are correct, the parameters providing a good fit will correspond to those of the event.

We develop a fireball model starting from its analytic, asymptotic behaviour parameterized by its fundamental parameters (energy, collimation, density, and microphysics). We find good fits to four of the best-sampled broadband afterglow data sets, with simple assumptions concerning the unknown microphysics and circumburst density profile. We present the resulting fit parameters, showing reasonable energies, densities similar to those of diffuse clouds, and a large spread in such microphysical parameters as the fraction of shock energy used to generate magnetic fields.

We also present results where the model fit showed degeneracies and other data sets that are not well-fit by this model. Motivated to determine the model's inherent uncertainty from the adoption of physical assumption, we consider some changes to these. We present our results: that a range of magnetic energy fraction variation with shock strength is permissible, and that afterglow fits are not sensitive to steeply rising circumburst power law density profiles. We demonstrate that the fitted parameters change when the assumptions are changed; this may be by a small fraction, or up to an order of magnitude.

Contents

List of Figures

List of Tables

Chapter 1

Introduction: A Recently Discovered Phenomenon

"Who ordered THAT?" – attributed to Isidor Rabi upon the discovery of the muon

Gamma-ray bursts (GRBs) are an example of an unexpected discovery made while scientists searched for something else. GRBs are the most luminous events in the universe, each lasting from a fraction of a second to tens of seconds, a flash that drowns out the rest of the gamma-ray sky. While transients in the optical sky (e.g., novae, supernovae, variable stars) have been seen and studied for centuries, the detection and study of higher-energy radiation was not possible until the modern era. These γ-ray transients are a relatively newly identified phenomenon, discovered in the late 1960s. The research undertaken in this thesis is to further our understanding of GRB physics and environments.

During the Cold War era, the nuclear test ban treaty forbade atmospheric and outer space nuclear weapon tests. The US *Vela* satellite program was designed to verify Soviet adherence to the treaty. The satellites carried γ-ray detectors, as well as instruments capable of studying highly energetic charged particles and neutrons. The *Vela* instruments were sensitive to the characteristics (such as γ-rays) from clandestine nuclear tests, and also useful for solar studies and searches for γ-rays from supernovae.

A new phenomenon soon appeared: bright γ-ray flashes that were not characteristic of nuclear weapon detonations. These γ-rays were neither correlated with observed supernovae nor solar activity. Klebesadel, Strong & Olson (1973) reported bursts lasting 0.1–30 seconds that were not of local origin—neither from the Earth nor the Sun. Timing differences (for the onset, features, etc.) between two detectors on different spacecraft constrain the source position as they correspond to a distance difference to the photon source. Knowing the actual relative position of the two crafts gives an angle for the source relative to the mutual baseline of the spacecraft, and this traces out a circle on the sky that intersects the source. Uncertainty in the time differences will define an annular width to the circle. With three spacecraft, there are two independent timing differences. The intersections of the two annuli define two patches on the sky where the source may be. For events with sufficient timing information, Klebesadel, Strong & Olson (1973) determined that the possible GRB source positions did not include the Earth or Sun. The bursts were also not coincident with novae or supernovae.

So one of the legacies of the Cold War was the mystery of GRBs, whose study did not progress much for two decades. The characteristics of the γ-ray emission of GRBs varies too widely (in duration, pulse shape, having one or several peaks) for generalizations to lead to a clear picture; the uncertainty in their positions encompassed multiple field stars and background galaxies so no probable sources could be identified. The events' cause was so obscure that the ratio of hypothesized theories to known GRBs was about 1:2 (e.g., Strong, Klebesadel & Evans, 1975). Ruderman (1975) reviews theories ranging from flares on common F and G stars to relativistic dust grains composed of iron in the interstellar medium.

In 1991, the Compton Gamma-Ray Observatory (1991-2000) was launched with its Burst and Transient Source Experiment (*BATSE*) instrument. *BATSE* developed a large statistical sample (detecting approximately 2000 events Paciesas *et al.*, 1999), which indicated the distribution of GRB sources. These and other GRBs are identified by a standard nomenclature that had developed earlier as significant numbers of GRBs were detected. Each GRB is named by the (Universal Time) date of its observation at the Earth. The convention is to call a GRB "GRByymmdd", with yy=last two digits of the year, mm=month, dd=day; if more than one GRB are found in a day, a letter (A, B...) is appended to the names.

BATSE consisted of eight independent γ-ray detectors forming an octahedron. The relative fluxes at each detector depend upon the angles between the detector planes and the beam of incoming photons. GRB positions were determined by count-rate differences among the detectors (the *BATSE* web site[1] gives further details). With eight detectors, the locations were resolved to single patches on the sky, albeit only to within a few degrees.

The most significant result from this sample was the convincing demonstration of the isotropy and inhomogeneity of GRB events to faint flux levels (Meegan *et al.*, 1992). This research showed that there is no concentration in GRB numbers, peak energies or fluences on the sky, and no significant dipole or quadrupole moment in their distribution (verified more stringently by, e.g., Briggs *et al.*, 1996). Moreover, the intensity distribution is inconsistent with a homogeneous distribution of sources in space; there are fewer faint bursts than would be expected. Together, these properties of isotropy and inhomogeneity determined that we reside at the center of an isotropic distribution of GRB sources, with an edge. Meegan *et al.* (1992) suggested a natural explanation is that GRBs are of cosmological origin, with the edge formed by the finite nature of the universe.

The cosmological scenario gives a possible distance scale. It indicates the γ-ray luminosities would be extreme, especially in light of GRBs' rapid ($\lesssim$ msec) variability and non-thermal spectra (Band *et al.*, 1993). The variability timescale is expected to indicate the light-crossing time of the source in order that the source as a whole changes its emission. The observed variability requires a small size. The implied energy density would be opaque to pair formation and the resulting spectrum should be of a thermal source. This requires a highly relativistic emitter, with Lorentz factor $\Gamma \gtrsim 100$, to beam the emission. The relativistic beaming boosts the photons' energy and contracts the emitter's size in the observer frame, allowing an optically thin emitter with the observed variability (see for example Krolik & Pier, 1991; Brainerd, 1992; Fenimore, Epstein & Ho, 1993, and references therein).

A consequence of relativistic outflows is longer-lived lower frequency "afterglows", radiation produced by the expanding, cooling shock between the slowing outflow and the surrounding medium.

---

[1] http://cossc.gsfc.nasa.gov/batse/index.html

These afterglows were predicted and their theory developed before their discovery (e.g., Paczyński & Rhoads, 1993; Katz, 1994).

In 1997, a new era opened up in GRB studies with the discovery of these afterglows, enabled by the X-ray detectors of the *BeppoSAX* satellite (1996-2002). *BeppoSAX* had instruments monitoring γ-ray emissions, as well as several X-ray instruments, including wide-field cameras (sensitive to the hard X-ray tail of the GRB itself) and narrow-field instruments with angular resolutions down to a radius of one arcminute (for details, see Boella *et al.*, 1997). An observed burst could be detected simultaneously in the wide-field cameras with a resolution of ≈ 5', sufficiently accurate to reorient the spacecraft, bringing the narrow-field instruments to bear on the position. In this manner the burst of February 28, 1997 (GRB970228) was identified with its X-ray afterglow (Costa *et al.*, 1997b). Identifying the transient in the wide-field cameras, moving the narrow-field instruments to bear and determining the afterglow position would typically take about eight hours. However, the resulting positional uncertainty was small, (~ 1'), which permitted optical observers to search the entire field to deep (faint) flux levels. Groot *et al.* (1997) identified the optical afterglow. Soon afterwards, the bright afterglow of GRB970508 was identified (Costa *et al.*, 1997a; Bond, 1997) and Metzger *et al.* (1997) found cosmologically redshifted lines in its spectrum at z=0.835. The redshift determinations of this and other afterglows validated the cosmological nature of these GRBs.

It must be noted that the GRBs for which afterglows have been identified to date belong to only one class of events. An important *BATSE* discovery was that there are two major phenomenologically distinct subclasses of GRBs, known as “Long” and “Short”, or “Long/Soft” and “Short/Hard” classes (Kouveliotou *et al.*, 1993). There is a definite bimodal distribution in burst durations, with Long bursts ($>$ 2 s) peaking in number around 26 s, and Short bursts peaking around 0.33 s (in the “T_{90}” duration measure of Kouveliotou *et al.*, 1993, during which 5% through 95% of the γ-ray counts above the background are recorded). The Short bursts tend to have a harder γ-ray spectrum than the Long bursts. The *BeppoSAX* instruments identified a GRB trigger by comparing the flux averaged over a short time interval, 1 s, to a longer background interval; the result was quite insensitive to Short GRBs (Feroci *et al.*, 1997).

At present, there are γ-ray detectors that can potentially detect Short GRBs, but precise, rapidly disseminated positions are rare. The Interplanetary Network (IPN) is a network of spacecraft used for other scientific missions that carry γ-ray detectors on board to also detect GRB events (for one resulting GRB catalog, see Atteia *et al.*, 1987). These detectors are capable of triggering on Short GRB events (e.g., Hurley *et al.*, 2002). The timing-difference principle, as used by the *Vela* satellites, determines the positions. The IPN includes missions beyond the Earth-Moon system. The resulting baselines are longer and thus produce far more accurate positions than the *Vela* satellites. IPN data must be returned from several spacecraft with different telemetry schedules, so the resulting positions are usually at least one day old. At this time, the afterglow has significantly faded, beyond flux depths reachable by many optical searches. This problem especially hinders searches for fainter afterglows (see the discussion of the detection of nearly "dark" bursts in Fynbo *et al.*, 2001b; Berger *et al.*, 2002). In addition, the *HETE* satellite has co-aligned X-ray instruments designed to detect the X-ray emission of GRBs and constrain their position with observations in the soft Xrays. This arrangement permits prompt localizations, potentially contemporaneous with a burst (see Kawai *et al.*, 1999; Vanderspek *et al.*, 1999; Fenimore & Galassi, 2001, for some discussion of the satellite's instruments and capabilities). Nevertheless, Short GRBs have less fluence and therefore a lower signal and so are detected less often and with larger errors by such instruments as *HETE*. No GRB that is definitively a member of the Short class has had an identified counterpart, and Short GRBs may have a different physical origin from the Long ones. This thesis deals only with modelling of Long GRB afterglows, and hereafter reference to a 'GRB' refers to a burst of the Long class.

GRBs and their afterglows offer a unique opportunity to study ultra-relativistic to trans-relativistic shocks, which are not easily accessible in the laboratory. GRB progenitors are theorized to be the result of the deaths of massive stars (Paczyński, 1998; MacFadyen & Woosley, 1999) or the coalescence of compact objects such as neutron star binaries (Goodman, 1986; Eichler *et al.*, 1989; Mészáros & Rees, 1997), with the attendant formation of a central compact object such as a black hole or magnetar. The GRB could be powered by accretion onto the object or extraction of its energy via a method such as the Blandford-Znajek mechanism (Blandford & Znajek, 1977). Mészáros (2002) gives a review of the present state of the theory. Thus, studies of GRBs, their afterglows, and their environments potentially allow brief glimpses into supermassive stellar deaths, the formation of compact objects, and the extraction of energy from them.

Afterglows provide more diagnostic information than the prompt GRB emission. First, afterglow evolution is observable for much longer–from fractions of days to a year. Second, afterglows are observable over a wider range of wavelengths, giving a broader picture of the event. It is through optical spectra that crucial information such as GRB redshifts are routinely determined. Third, afterglows, observed in the X-rays, optical, and radio (by instruments with very good spatial resolution), can be used to determine the GRB's association with other nearby objects, such as a host galaxy. Fourth, afterglows are generally observed to behave in a well-defined manner. They decay as a power law in the optical to the X-ray, and initially rise, then fall as a power law in the radio, with possibly an observed break in the power law index. This smooth evolution is much more easily modelled than the bursts of γ-rays. The smooth afterglow evolution would arise naturally in the hypothesized "internal-external shocks" scenario, wherein a nonuniform, highly relativistic flow collides within itself to produce the erratic GRB prompt emission. The flow would be highly smoothed when the external shock's interaction with the surrounding medium produces the afterglow.

Afterglows are usually interpreted in a "fireball" model (from early work, e.g., Waxman 1997, and as reviewed more recently by Mészáros 2002) that accounts for their relatively smooth evolution. Their broadband spectra appear to consist of broken power law segments, suggesting synchrotron emission. This model, which will be described in more detail in Chapter 3, takes a shock in self-similar expansion with no dependence upon the details of the initial conditions, and describes its hydrodynamical evolution and its emission in terms of basic quantities such as the energy in the shock, the density of the surrounding medium, and the shock microphysics governing the acceleration of the radiation-emitting electrons. The model rests upon several assumptions concerning the shock physics, but if they are reasonably accurate, afterglow observations will allow the determination of physical properties of highly relativistic shocks and their surroundings. It is therefore quite important to address how much any uncertainty in the model may affect the estimates of the physical quantities associated with an event.

This thesis adds to the study of GRB afterglows; it examines the fit of afterglow data sets to the fireball model and addresses the uncertainties in both the fitted results derived from comparison of afterglow events to the fireball model, and in the afterglow fireball model's assumptions. First, this thesis discusses our understanding of afterglows in the context of the basic fireball model. Chapter 2 describes a typical afterglow data set and addresses efforts to secure comprehensive afterglow data sets. Chapter 3 describes the afterglow emission of, and our implementation method for, the fireball model in the context of other types of modelling efforts. Chapter 4 describes the fits to four high-quality data sets, performed with the basic model. Chapter 5 compares these results. Chapter 6 addresses good quality data sets that did *not* result in good fits with the basic model. Then this thesis investigates the constraints placed on some of the basic model's assumptions by the data of the four events that resulted in good fits. Chapter 7 considers whether the fraction of energy in the post-shock magnetic field can evolve as some power of the bulk Lorentz factor. Chapter 8 investigates the range of possible matter density gradients in the circumburst medium. Chapter 9 examines what possible afterglow observations could discriminate between presently equally good fits with different model assumptions. Chapter 10 summarizes the conclusions.

Chapter 2

The Milder Face of GRBs: Afterglow Observations

The quality of an afterglow data set is crucial to its ability to constrain the model. Here we present the typical discovery and followup methods for a GRB afterglow, beginning from the GRB "trigger", and the consequent sampling and quality of broadband afterglow observations.

GRB followup begins when a reasonable position for afterglow searches is disseminated to the community of interested observers. The positions and related information concerning gamma-ray bursts, from the various incarnations of the Interplanetary Network (IPN), to the more recent *BeppoSAX*, *HETE*, and *Integral* missions, have been distributed by the unrefereed *Gamma-Ray Coordinate Network* notices (GCN Notices)[1] (originally the BACODINE system to connect *BATSE* alerts to ground-based observers, Barthelmy *et al.*, 1995). Any interested person can sign up to receive GCN Notices by e-mail.

With a GRB's coordinates, the new event's positional error box is observed (typically at optical wavelengths). This may be done via observers contacting telescope users and requesting that images be taken. In addition, several automated telescopes are used by groups worldwide to investigate various astronomical questions. The GCN maintains several distribution methods[2] for GRB alerts. Standard-format "socket" messages[3] distribute the positions directly to a list of computer addresses (as requested by observers). These are automatically parsed by some automated telescopes, enabling

---

[1] available at http://gcn.gsfc.nasa.gov/gcn/, written and maintained by S. Barthelmy

[2] described at http://gcn.gsfc.nasa.gov/gcn/gcn_describe.html#tc7

[3] method detailed at http://gcn.gsfc.nasa.gov/gcn/tech_describe.html#tc17

them to immediately abort their ongoing programs and search for a transient.

Since no single observatory is capable of responding to GRB events in all parts of the sky (or at all times), the large number of independent GRB investigators is important for the discovery and subsequent study of the afterglows. For this purpose, we initiated the *REACT* network in 1999. This was an informal effort to bring optical astronomers interested in GRB afterglow searches appropriate information, and so to improve the afterglow discovery rate by extending the number of observatories involved worldwide. My involvement was to manage the distribution of GRB trigger information, with the intent to simplify the acquisition of information useful in afterglow searches. This involved the creation of a script which, given the burst error box, produces pages giving coordinates, archival images with the error box superposed, as well as nearby standard stars, estimates of the Galactic extinction of light by dust in its direction and information on the times the position is visible at each observatory. Observers could consult the pages for any event, and the comparison of times when the position is visible at observatories help to sort out whom to contact. For those collaborating with the Caltech GRB group, a data upload page is conveniently linked there.

Once an image covering the error box is available, the afterglow may be discovered (if bright) as a new object relative to archival images such as the (optical) Digital Sky Survey[4] by eye, or by scaling the image sizes and blinking between them. If the afterglow is not obvious, either due to a crowded field or a faint flux relative to the archival images' depth, a second exposure (later in the night, the following night or by comparison with another observatory whose night ends later) can reveal afterglow candidates by image subtraction. A fading source is likely an afterglow. This will also confirm that a "new object" missing in archival data is not simply brighter at the observed wavelength than at the band used for the archival image. In all cases, further observations to confirm the fading will eliminate other variable source types. Given the large number of optical observatories relative to those for other wavelength ranges, in the majority of cases the confirmation of a fading transient will be in the optical.

Information concerning afterglow searches (and followup) can be submitted as a GCN Notice,

---

[4] available at http://stdatu.stsci.edu/dss/index.html; The Digitized Sky Survey was produced at the Space Telescope Science Institute under U.S. Government grant NAG W-2166. The images of these surveys are based on photographic data obtained using the Oschin Schmidt Telescope on Palomar Mountain and the UK Schmidt Telescope.

and immediately given, unrefereed, to the community. Positions of afterglow candidates and early measures of magnitudes or fluxes are commonly disseminated in order to verify a candidate and to determine the quality of the event (i.e., whether the optical afterglow is bright, or whether there is a radio afterglow visible). Precise photometry of the field for comparisons is often announced to allow observers to properly compare their flux determinations of candidate objects. GCN Notices may also simply announce a rare observation (such as the times an X-ray observatory will image the afterglow), to urge observational coordination.

During the *BeppoSAX* era, the result from this network would give response times to get "on source" of approximately a day. With e-mail alerts to cellular phones and socket messages submitting positions to automated telescopes, the followup response can be near-instantaneous to the distribution of a γ-ray position. The *HETE* satellite is capable of determining GRB positions in minutes to a few hours; response times are now typically a fraction of a day (even 0.1 days) post-GRB, and there are some events observed within ten minutes of the GRB trigger.

Small telescopes are first used to image the GRB field, as their fields of view encompass the initial GRB (or X-ray afterglow) positional error box. Once these instruments determine an accurate afterglow position, generally to a precision of $\sim 1''$, larger observatories can come to bear on the position. These provide more sensitive observations. These more sensitive views may be acquired for the early afterglow with fast GRB triggers and small telescope followup.

The resulting afterglow data show behaviour much simpler than the highly variable prompt GRB emission, with power laws (whose indices do not vary by large amounts from event to event) describing the spectrum and the rise or decay of the flux at various wavelengths. The typical brightness of an afterglow is at most about 1 mJy[5]. The overall appearance of an afterglow at a point in time roughly resembles a broken power law in spectral flux density from the radio ($\sim$ GHz) to the X-ray ($\sim$ keV $\leftrightarrow 10^{18}$ Hz). We show examples in Chapter 3 (Figure 3.4) and Chapter 4 (Figures 4.8, 4.9). For further information, van Paradijs, Kouveliotou & Wijers's (2000) Table 1 gives an overview of observed afterglow properties. These afterglow characteristics can be seen even

---

[5] 1 Jy = 10^{-23}erg cm^{-2} s^{-1} Hz^{-1}

in the many events for which only a small amount of data is collected, such as a faint afterglow only visited a few times in the optical. The characteristics are far clearer in well-studied events.

Given the numerous optical observatories, most observations in an afterglow data set will usually be in optical and near-infrared (NIR) wavelength bands. These also tend to be the earliest observations, although in some cases *BeppoSAX*'s dedicated response could produce more rapid followup. A well-studied event may have ~ 100 optical-NIR data points. As the afterglow is usually discovered in the optical, these observations begin early, somewhat less than or near one day post-burst. A well-observed event will include data in several optical-NIR bands. The most popular observational band is R and it is almost invariably the most densely sampled; lesser sampling is often performed with such filters as $BVIJHK$. There may be only a couple of points in some bands (such as NIR, where J and H appear to be used less often than K), and a dozen or more in others (such as B or V). The power law spectral shape is seen in comparisons of observations across these bands. At these frequencies, the afterglow is observed to decay in time as a power law, often consistent with a single decay power law that can be explained by the synchrotron emission from a single "fireball" source. The optical transient will become significantly fainter than the flux from its host system after one week to one month; observations cease to be useful for studying the afterglow at that time.

Typically the radio is the next wavelength range in which the afterglow is observed. With fewer radio observatories, radio observations of a well-studied event will be less densely sampled than optical observations but generally cover a far longer time span. As the radio is below the afterglow spectral peak around one day post-burst, its flux is increasing at that time. The radio flux generally rises to a peak, then decays, as a power law. This peak can be seen to pass, as time progresses, through different radio wavelengths towards the low frequencies. We show examples in Chapter 4 (Figures 4.7, 4.11). (The submillimeter may also be below the spectral peak but its behaviour is less clear as present instruments have uncertainties at ~ 1 mJy, comparable to the afterglow's flux.) Radio observations may begin a few days after the GRB and last for several months, even more than a year post-GRB. The radio Very Large Array (*VLA*) instruments can measure flux at a few frequencies (around 1, 5, and 8 GHz) simultaneously, so several dozen (even up to a hundred) data points over two or more radio wavelengths can be obtained in good cases. The optical tends to be initially bright enough to get low flux uncertainties (at the [few] percent level) for most of the data, whereas much of the radio data is only detected with a signal to noise of a few.

Finally, a "well-studied event" will most likely include X-ray observations as well as those in several optical-NIR and a few radio wavelength bands. The X-ray region's spectral shape is best fit by a power law with absorption at low energies by Galactic material along the line of sight. X-ray flux is expected to be absorbed by the column of gas in the Galaxy. Dickey & Lockman (1990) provide a map of Galactic column densities; the *w3nh*[6] web-based tool provides column depths for specified coordinates. As X-ray frequencies are above the spectral peak at the times of observation, the afterglow is observed to decay as a power law, as it does in the optical. Sometimes the X-ray decay has a steeper power law index than that of the optical, suggesting a spectral break between these two spectral regions (see the discussion of the 990510 X-ray afterglow, Kuulkers *et al.*, 2000). These decays, scaling with time t as t^{-n}, often have $n \sim 1$. In many cases an apparently achromatic steepening can be seen to $n \sim 2$.

The X-ray flux level of the afterglow for the first few days may be ~ 0.1 μJy for a bright case. The X-ray afterglow is too faint for detection after a couple of weeks. Typically there is far less X-ray data for a well-studied event than either of the previously described wavelength ranges. For events that were discovered by *BeppoSAX*, its observations provide X-ray afterglow fluxes at a fraction of a day. For events where such a dedicated satellite response is not available, the *Chandra* and *XMM* observatories may provide X-ray afterglow observations. Due to the high demand upon these facilities and the time required to reschedule for a new target, these satellites typically visit the afterglow once or twice for periods of several tens of kiloseconds. X-ray instruments record each detected photon, binning the results (in energy or time) to measure the flux accurately. A good GRB afterglow observation may have as little as three to five independent X-ray measurements binned from the data. These measurements are determined for one or two frequencies across the X-ray range (effectively about 0.3-10 keV with present instruments).

---

[6] http://heasarc.gsfc.nasa.gov/cgi-bin/Tools/w3nh/w3nh.pl

As these broadband data sets develop, the record of GCN Notices illustrates certain observational issues. There are a great number of optical observers who take measurements; a typical good event will be observed by approximately ten telescopes, and an exceptionally bright afterglow may have more than 30 observers. Even those reporting data acquisition in the same filter (for instance, "R"), may be using slightly different variants. (Fernie 1983 discusses the transformation between two different VRI systems; Bessell 1990 details some of the general problems, indicating the pass-bands of several commonly used $UBVRI$ filters.) This filter variation limits the accuracy across data sets. Observers may also use different photometry methods (such as different comparison stars). Even results reported by a single observer, such as X-ray fluxes presented for the purpose of getting a view of the afterglow behaviour, may be incomplete in the GCN Notices. Notices often lack uncertainties or data reduction methods, or give only rough times of observation.

One method to avoid photometric calibration offsets is by having a collaborating group take a consistent data set with a uniform photometry method in the optical, even comparing the results for the same standard stars at different sites to bring the photometric systems into agreement at sub-percent accuracy. For optical followup, the Caltech GRB group has programs at the Palomar and Keck observatories and collaborates with observers in Australia (at Mt. Stromlo and Siding Springs) and Israel (at the WISE observatory).

During the early years of afterglow searches, since it is unlikely that a GRB would be detected precisely during an individual's assigned observing time, the Caltech GRB group reached somewhat informal arrangements with observers at the Caltech telescopes. The arrangements exchanged time during upcoming runs of the GRB group for immediate observations by the observer on site. The 60" telescope at Palomar, increasingly under-subscribed in recent years, has also been used during times when no observer was scheduled, sending a group member on an emergency run to the mountain. Even engineering time at the Hale 200" telescope has been used for GRB afterglow searches.

Such processes at Caltech became increasingly organized as the field matured. GRBs are one class of objects demonstrating the importance of rapid followup of transient events, and so by the year 2000, the Palomar Time Allocation Committee developed a Target of Opportunity (TOO) proposal class. Such programs are assigned a finite amount of override time. When a TOO is used, the regularly assigned Palomar observers must abort their observations and perform observations for the TOO program. Informal arrangements are still made when TOO overrides are not advisable, such as when a long period of followup is required. With aid from collaborators who automated the Australian 50" Mt. Stromlo telescope, the Caltech GRB group has also connected the Palomar 48" telescope to the socket message network, where GRB observations are an allowed override to the usual asteroid-search sky patrol.

A consistently observed and reduced optical dataset does not eliminate all observational issues for a rapid broadband view of the afterglow. Other wavelength regions have incompletely reported data. While the Caltech GRB group has a radio program at the *VLA* and has at times had a Target of Opportunity program on the *Chandra* X-ray telescope, these observations can be difficult to compare to other reported radio and X-ray data, often given as rough estimates with no associated uncertainties. Once a paper is published many of these issues are resolved, yet reasonable uncertainty estimates may still need to be applied to some data only reported on the GCN. With sufficient cause, we allow extra uncertainty above that reported while compiling a data set, even applying additional uncertainty to all the data as a “calibration uncertainty”, since the systems to convert observations in the X-ray, various optical filters, and the radio to flux densities are not universally cross-calibrated.

In some data sets there are deviations from the smooth spectral and temporal power laws described here. Some abnormalities may be attributable to cross-calibration offsets amongst observers, for example, the scatter seen beyond two days in the GRB 970508 afterglow data set (one of the broadband data sets discussed at length in Chapter 4 of this thesis). Other, more complex cases are discussed in detail within the context of individual events in Chapter 6.

Chapter 3

The Afterglow Model: Fireballs and What to Do with Them

The basic ingredients of the fireball model of afterglows are a relativistic blast-wave and synchrotron emission.

Blandford & McKee (1976) first developed the theory for the hydrodynamic evolution of a highly relativistic shock. When a large amount of energy is placed in a small volume, the result is an explosion that sweeps a strong shock into the surrounding medium. Under many circumstances the shock reaches a phase sufficiently disconnected from the explosion that its evolution no longer depends upon the explosion's details, but only on the energy involved and medium encountered. Such a situation can be scaled to these quantities in a "similarity" solution. The Blandford & McKee (1976) solution finds the similarity solution for the shock motion (and distributions of pressure, velocity and density of material behind the shock) for a spherical relativistic shock with a variety of surrounding density profiles and energy supplies or losses.

The Blandford & McKee (1976) solution's time dependence of the shock's Lorentz factor, γ, provides much of the emission's expected behaviour. The other key element is the emission mechanism for material entrained in the flow. Observations of afterglows show broken power law spectra (see Chapter 2); the emission is clearly non-thermal. This behaviour requires a non-thermal emission mechanism such as inverse Compton scatters of ambient low-energy photons gaining energy off the relativistic entrained electrons, or synchrotron radiation by the oscillation of these electrons in a magnetic field. It is not clear what would produce the ambient photons that interact with the shocked electrons in the Comptonized picture. Synchrotron emission is considered far more likely, although some Compton upscatters of these photons may contribute to the spectrum. Synchrotron emission provides a natural explanation for the broken power law spectrum, which is produced by a population of electrons with a power law distribution of energies. A power law energy distribution can result from an acceleration process where the particles have a constant escape probability for each acceleration cycle, such as Fermi acceleration.

Synchrotron radiation is the radiation emitted by relativistic electrons spiralling around magnetic field lines. Its basic properties are discussed at length in textbooks such as Rybicki & Lightman (1979). Each electron's power peaks strongly at a characteristic energy-dependent frequency. The electron's spectral power density rises as a power law proportional to $\nu^{1/3}$ below the characteristic frequency and drops exponentially above that peak frequency. Properties of the synchrotron radiation of a distribution of electrons are determinable from those of a single electron. The spectral flux density is proportional to the sum over spectral power densities.

If the electrons have a minimum energy, there is a minimum in the peak frequencies of the electrons that produce the synchrotron radiation. Below that frequency, ν_m, the spectral power densities are all proportional to $\nu^{1/3}$, and the resulting spectrum is also proportional to $\nu^{1/3}$. If above the minimum electron energy the electron energies are distributed as a power law, $N(E) \propto E^{-p}$, the spectrum is a sum of the spectral powers of each electron in the power law distribution. Each electron's power peaks at its characteristic frequency, and the total spectral power is dominated by the power law distribution of these peak powers. The resulting spectrum is also a power law ($\nu^{(1-p)/2}$).

Figures 3.1 and 3.2 show typical broadband synchrotron spectra, with the minimum electron energy spectral break ν_m as well as two other breaks. There is a cooling break at ν_c, which corresponds to emission from electrons with energies at which radiative losses over the shock's lifetime are significant. Above ν_c the electrons have less energy to radiate and the spectrum steepens. The self-absorption break ν_a is where the spectrum becomes optically thick at low frequencies. If the minimum energy electrons emit at a peak frequency above the self-absorbed regime, the spectrum

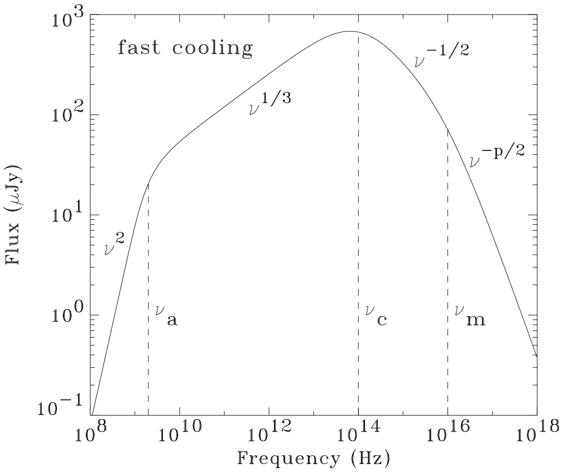

Figure 3.1: Synchrotron spectrum for fast-cooling electrons for illustrative self-absorption (ν_a), cooling (ν_c), and minimally accelerated electron energy (ν_m) spectral breaks. In this situation, all electrons can radiate and cool significantly in the lifetime of the shock, and there are cooled electrons at energies below the minimum shock-accelerated energy (those radiating with peak frequencies $\nu_c < \nu < \nu_m$). For electron distribution $P(\gamma) \propto \gamma^{-p}$ (here $p = 2.5$), the spectrum above the peak is proportional to $\nu^{-p/2}$ for $\nu > \nu_m$, and to $\nu^{-1/2}$ for $\nu_c < \nu < \nu_m$. Below the peak, the spectrum is proportional to $\nu^{1/3}$. This results from the synchrotron emission, proportional to $\nu^{1/3}$, from each electron below its peak frequency. At low frequencies the spectrum is self-absorbed, with the flux proportional to ν^2.

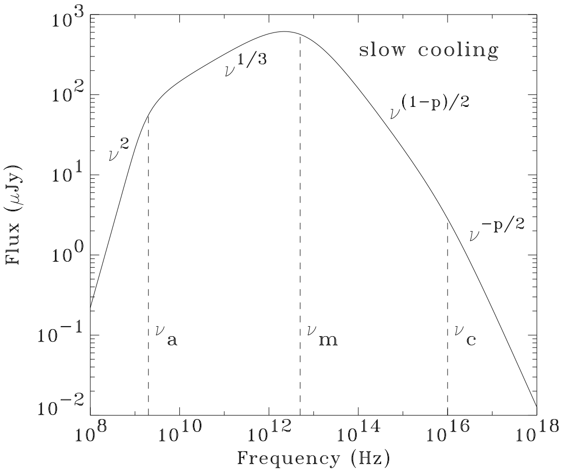

Figure 3.2: Synchrotron spectrum for slow-cooling electrons for illustrative self-absorption (ν_a), cooling (ν_c), and minimally accelerated electron energy (ν_m) spectral breaks, with accelerated electron distribution $P(\gamma) \propto \gamma^{-p}$, $p = 2.5$. Electrons that can radiate and cool significantly in the shock lifetime have peak emission frequencies above ν_c. Those whose emission peaks below ν_c cannot cool significantly on the shock's timescale; their energy is not available to radiate. This contrasts with the fast cooling case where all electron energy is available to radiate. The regimes differ in energy loss rates; the transition is important to the energy correction calculations. The spectral slopes are as in Figure 3.1, save that for $\nu_m < \nu < \nu_c$, it is proportional to $\nu^{(1-p)/2}$.

below ν_a is proportional to ν^2, resembling a blackbody with effective temperature corresponding to that minimum energy. If electrons are emitting within the optically thick regime, the effective temperature is a function of frequency and the spectrum is proportional to $\nu^{5/2}$ where $\nu > \nu_m$, and proportional to ν^2 where $\nu < \nu_m$ (see Rybicki & Lightman, 1979).

The synchrotron spectral shape depends upon the electron energy distribution. The energies imparted by a relativistic shock must be by a collisionless acceleration mechanism. However, the mechanism of collisionless shock acceleration is obscure, as seen for example in the discussion by Pelletier & Marcowith (1998) of various plasma instabilities that may drive plasma waves and couple ambient protons to the flow. The details of imparting energy to the shocked electrons by the shock acceleration process are unknown. Hence the electron energy distribution cannot be theoretically determined. The input spectrum of electron energies must be assumed, but if it occurs in a probabilistic manner, the result would resemble a distribution with minimum energy and greater energies distributed as a power law of constant index. There is precedent for such an energy distribution as it is analogous to the power laws observed in emission from supernova remnants, modelled as synchrotron emission from particles accelerated by these strong shocks (e.g., Asaoka & Koyama, 1990; Koyama *et al.*, 1995). Simulations assuming conditions for diffusive shock acceleration, where charged particles are repeatedly scattered by magnetic irregularities, give a power law distribution for the accelerated particles even for ultra-relativistic shocks (e.g., Bednarz & Ostrowski, 1998; Kirk *et al.*, 2000; Achterberg *et al.*, 2001).

The method of producing sufficiently strong magnetic fields and the field distribution in the shock are also not well known. Currently the shock physics is improving as more comprehensive magnetohydrodynamic simulations are produced (see the review by Kirk & Duffy, 1999, and references therein). At this time there are no results for the magnetic fields that reduce to analytic solutions from first principles without assuming significant simplifications. With sufficiently constraining data it should be possible to test the validity of these model assumptions, or at least test the range over which they describe the data. With a large number of model parameters, only a few GRB data sets are of sufficient quality for that purpose.

The hydrodynamic evolution of a relativistic shock is subject to many uncertainties, such as the environment's effects. The afterglow model is further uncertain as it relies upon microphysical assumptions to produce the observed broken power law spectra. Nevertheless, early afterglow fits, even with quite simple assumptions concerning the fireball, successfully described data sets (e.g., Wijers, Rees & Mészáros, 1997), suggesting that the model is broadly correct.

Examples of power law spectra as produced by the fireball model are illustrated in Figures 3.1 and 3.2, with the break frequencies described above in the typical range for GRB afterglows. The fireball model spectrum evolves in time, as the shock expands and cools (adiabatically or radiatively). The peak shifts to lower frequencies, but the behaviour of the break frequencies and peak height depend upon the precise assumptions concerning the fireball and its surroundings. For instance, a denser environment will cause the shock to slow more quickly as it transfers energy to the swept-up particles. A spatial gradient in the density can also produce a smooth change with time in the hydrodynamic behaviour. The surrounding density profile has great effect upon the shock evolution. The differences between the "Wind" (r^{-2}) and "ISM" (constant over r) density profiles will be further elaborated in later sections.

Changes in other parameters also produce a variety of different shock behaviours. But, with a set of parameters and assumptions, the fireball model emission can be determined. We adopt assumptions for the density profile of the circumburst medium, the shock geometry, and the shock microphysics including the distribution of electron energies, as described in detail in the next section. The model also accounts for the effects upon the received spectrum of the medium through which the radiation passes en route to the observer.

3.1 General Physical Assumptions: The Basic Afterglow Model

Early work (as in Wijers, Rees & Mészáros, 1997) on the fireball model provided a reasonable description of many data sets using very simple assumptions for the unknown aspects of the model. These aspects include the microphysics of the shock and the distribution of material in the surrounding circumburst medium. The fireball model with these simple assumptions is what we term the "basic afterglow model". These simple assumptions will be tested in further sections of the thesis.

The basic model generally considers two types of physical environment. The simplest is a constant circumburst matter density n, called the "ISM-like" case, since the interstellar medium (ISM) can be uniform over great distances. A constant mass-loss rate and wind speed gives an r^{-2} profile, termed the "Wind-like" case. A wind-driven medium is considered a likely form for the circumburst environment, in the context of hypothesized GRB progenitors. Due to the explosive (non-repeating) nature and energies of GRBs, progenitor candidates include the deaths of massive stars (MacFadyen & Woosley, 1999). Massive stars are known to alter their environment by shedding mass through winds (as in the significant mass-loss winds of Wolf-Rayet stars, whose properties are reviewed by

Abbott & Conti, 1987). The constant mass-loss Wind-like case is an approximation to true wind-enriched environments that is suitable for the hydrodynamic similarity solutions for the shock.

The basic model also allows either an isotropic shock or collimated ejecta. For collimated ejecta, the standard assumption is a top-hat distribution in solid angle with half-opening angle θ. The collimated shock behaves as though isotropic until it slows sufficiently to expand in its rest-frame (Rhoads, 1999; Sari, Piran & Halpern, 1999). The collimation becomes evident from the expansion in the rest-frame as well as the shock deceleration which decreases the relativistic beaming angle, allowing the jet "edge" to be seen as a flux deficit in the evolution. These effects occur at nearly the same time, and the time t_{jet} is calculated as $\gamma(t_{jet}) = 1/\theta$. This relation is the condition for relativistic beaming to reveal the jet edge; γ is the shock Lorentz factor and the assumption is that the observer's line of sight is nearly along the jet axis.

With the pre-jet evolution equivalent to the isotropic case, it is often best to parameterize the basic model in terms of its isotropic-equivalent energy and correct for such collimation when discussing the fitted energy value. Our application of the basic model also includes calculations of the expected radiative losses, which can modify the shock dynamics (Sari, 1997). These are detailed further later in the chapter.

The standard microphysics of the "basic model" has several assumptions. First, it assumes that the shock imparts a constant fraction of its energy (ϵ_e) to the set of swept-up electrons, and a constant fraction (ϵ_B) goes into amplifying magnetic fields. It also assumes that the electrons are accelerated into a simple power law distribution of energies above a minimum value

$$P(\gamma_e) \propto \gamma_e^{-p},\ \gamma_e > \gamma_m \tag{3.1}$$

The electron energies correspond to their Lorentz factors γ_e and the electron energy index p is constant. This distribution, Equation 3.1, can only be valid for $p > 2$. As $p \rightarrow 2$, the energy per logarithmic interval reaches equality and the total energy, without an upper limit to the distribution, diverges to infinity. The behaviour of the upper energy cutoff would dominate the results for $p < 2$.

3.2 Before It Gets Complicated: Simple Fireball Scalings

The basic set of parameters for the fireball model are the shock energy E, a surrounding density parameter (the constant number density, n, if ISM-like or A, where the density $\rho = Ar^{-2}$, if Wind-like), the collimation half-angle θ, and the microphysical ϵ_B, ϵ_e, and p. Each spectral break (ν_a, ν_m, ν_c) depends upon these quantities in different ways. The basic parameter set produces the initial set of spectral breaks. The spectrum's evolution in time is chiefly determined by the density profile, and whether the observations are pre- or post-jet. The sources of the detailed calculations are enumerated in §3.4, but the basic behaviour can be explained by order of magnitude calculations. In the following we take units where $c = 1$ and determine only proportionalities. This basic treatment is similar to those of Sari, Piran & Narayan (1998) (ISM-like) and Mészáros, Rees & Wijers (1998) (including the Wind-like case).

First, the basics of the hydrodynamics can be understood by calculating the evolution of the shock Lorentz factor γ in time as perceived by the observer. With the effects of relativistic beaming, the time emission is received at the observer is

$$t \propto r/\gamma^2 \tag{3.2}$$

when the emission is from a distance r from the event in the frame at rest with respect to the unshocked environment. (This is the observer's frame, apart from cosmological redshift.) In the relativistic limit, with mass M, the energy $E = M\gamma^2$. The matter gains a factor of γ from the relativistic frame boost (in the shock's frame, the upstream unshocked material has a Lorentz factor γ), and another from the fluid's relativistic shock jump condition. The mass M is from the swept-up region and, depending upon the density profile ρ, for either $\rho = m_p n$ (m_p the proton mass) or $\rho = Ar^{-2}$, the energy is

$$E \propto nr^3\gamma^2, \text{ or } E \propto Ar\gamma^2\,.$$

Substituting for r from Equation 3.2, the result for the shock is

$$\gamma \propto (E/n)^{1/8} t^{-3/8}, \text{ or } \gamma \propto (E/A)^{1/4} t^{-1/4} .$$

The magnetic field strength governs synchrotron emission. The magnetic field energy density $B^2/8\pi = \epsilon_B \gamma^2 n(r)$, which results in a magnetic field strength of:

$$B \propto \epsilon_B^{1/2} E^{1/8} n^{3/8} t^{-3/8}, \text{ or } B \propto \epsilon_B^{1/2} E^{-1/4} A^{3/4} t^{-3/4} .$$

Given the microphysical assumptions enumerated above, the relations between γ and the Lorentz factors of the electrons are calculable. We determine the Lorentz factor corresponding to the minimum electron energy by first relating it to the average electron Lorentz factor and the distribution $N(\gamma_e) \propto \gamma_e^{-p}$, so $< \gamma_e >= \gamma_m (p-1)/(p-2)$. The energy in the shock and the electrons is then related by $m_e < \gamma_e >= \epsilon_e m_p \gamma$. Thus,

$$\gamma_m \propto \epsilon_e (E/n)^{1/8} t^{-3/8}, \text{ or } \gamma_m \propto \epsilon_e (E/A)^{1/4} t^{-1/4} .$$

The cooling break is determined by an electron that would lose all its energy if it radiated the synchrotron power for the shock lifetime t. The power in the frame of the emitter is proportional to $\gamma_e^2 B^2$ (see Rybicki & Lightman, 1979), and this power is boosted by γ^2 into the observer frame. The energy of the electron is proportional to its Lorentz factor γ_c and is boosted by γ, so the result is

$$\gamma_c \propto \epsilon_B^{-1} E^{-3/8} n^{-5/8} t^{1/8}, \text{ or } \gamma_c \propto \epsilon_B^{-1} E^{1/4} A^{-5/4} t^{3/4} .$$

The peak emission frequency, boosted into the observer frame, is $\nu(\gamma_e) \propto \gamma \gamma_e^2 B$. This gives the observables, the break frequencies:

$$\nu_m \propto \epsilon_e^2 \epsilon_B^{1/2} E^{1/2} t^{-3/2}, \text{ or } \nu_m \propto \epsilon_e^2 \epsilon_B^{1/2} E^{1/2} t^{-3/2}$$

$$\nu_c \propto \epsilon_B^{-3/2} E^{-1/2} n^{-1} t^{-1/2}, \text{ or } \nu_c \propto \epsilon_B^{-3/2} E^{1/2} A^{-2} t^{1/2}.$$

The peak of the (optically thin) spectrum is at the lower of these frequencies. The spectrum's peak at ν_m is proportional to the spectral power density (power per unit frequency) of electrons with energy $\gamma_m m_e$ (m_e the electron mass) at their characteristic frequency ν_m. This quantity is approximately the total power emitted by these electrons (at all frequencies), divided by the characteristic frequency.

The total power emitted by one electron is proportional to $\gamma_e^2 B^2$ (e.g., Rybicki & Lightman, 1979) and is boosted by γ^2 in the observer frame. The characteristic frequency is, as explained above, proportional to $\gamma\gamma_e^2 B$ in the observer frame. The total power requires the number of shocked electrons ($\sim nr^3$ or Ar). Including all these factors, the result is a peak flux density:

$$F_{\nu,max} \propto \epsilon_B^{1/2} n^{1/2} E, \text{ or } F_{\nu,max} \propto \epsilon_B^{1/2} A E^{1/2} t^{-1/2}.$$

We note that it is constant in the ISM-like case, but drops as it encounters less material further from the burst in the Wind-like case. (By substitution for $r \sim \gamma^2 t$ in $\rho = Ar^{-2}$, we see that the encountered density $\sim t^{-1}$ with respect to time in the observer frame.)

Synchrotron flux becomes optically thick at low frequencies. If self-absorption is important at frequencies above the optically thin peak, the observed peak value will be lower than the peak calculated above, the value of the optically thin flux density at the self-absorption frequency.

The synchrotron self-absorption frequency is calculated by accounting for the source function, the intensity of an optically thick source. The source function is approximately a phase space factor times a mean energy for the source radiating at the frequency considered (kT for a thermal source). When the optically thick part of the spectrum is below the minimum peak emission frequency ν_m, the optically thick emission is dominated by the low-frequency emission from the electrons at the peak, with energy $\gamma_m m_e$. The source function at those frequencies is that of a blackbody of effective temperature corresponding to the energy $\gamma_m m_e$. Thus the self-absorption frequency is found by equating the synchrotron spectrum with a blackbody spectrum where $kT = \gamma_m m_e$. For the effective blackbody flux density, we note that this energy is boosted by a factor of γ in the observer frame, and that the effective surface area $\sim (r/\gamma)^2$.

The effective blackbody flux density is equated with the flux density for $\nu < \nu_m$ at ν_a. This ν_a is strictly for the ordering $\nu_a < \nu_m < \nu_c$, but ν_a under other orderings may be calculated from these break frequencies, as shown in Appendix A. For this simple ordering the resulting self-absorption frequency is

$$\nu_a \propto \epsilon_e^{-1} \epsilon_B^{1/5} E^{1/5} n^{3/5}, \quad \text{or} \quad \nu_a \propto \epsilon_e^{-1} \epsilon_B^{1/5} E^{-2/5} A^{6/5} t^{-3/5}\,.$$

This is constant in the ISM-like case. It drops in the Wind-like case as the average density decreases.

The basic spectral behaviour is deduced by calculating the flux density in various regions of the spectrum. We calculate the flux density, f_ν, by extrapolating the spectrum from the peak. For instance, just below the peak, $f_\nu = F_{\nu,max}\,(\nu/\nu_m)^{1/3}$. At each spectral break, the flux calculation acquires another factor. Continuing the example, further below the peak, $f_\nu = F_{\nu,max}\,(\nu_a/\nu_m)^{1/3}\,(\nu/\nu_a)^2$. The time dependence of the flux at a particular frequency depends upon the frequency's position relative to spectral breaks. The flux density depends upon the time dependence of the peak flux density, peak frequency, and any spectral break between the observed frequency and the peak. The time dependence of the flux density does not change when passing through the spectrum across a stationary spectral break.

To understand the model's description of the spectral evolution, we consider the case where $\nu_a < \nu_m < \nu_c$. This is reasonable as this ordering appears to match the observed spectra (Galama *et al.*, 1998). As described in Chapter 2, at a fraction of a day the optical flux declines, so the peak ν_m is below optical frequencies. In addition, at that time the radio flux rises, so ν_m is above the radio frequencies. The frequency ν_m will not drop below ν_a (which, when measurable in the radio, is $\sim$ GHz) during the typical observable timescale of the afterglow. While ν_c may be below ν_m during the initial observations, ν_m drops more rapidly. Thus the spectral ordering for an afterglow tends toward the canonical ordering $\nu_a < \nu_m < \nu_c$.

Figure 3.3 shows model light curves at low and high frequencies. At low frequencies, below the peak, the flux density rises. For the ISM-like case, the self-absorption break is stationary, with no

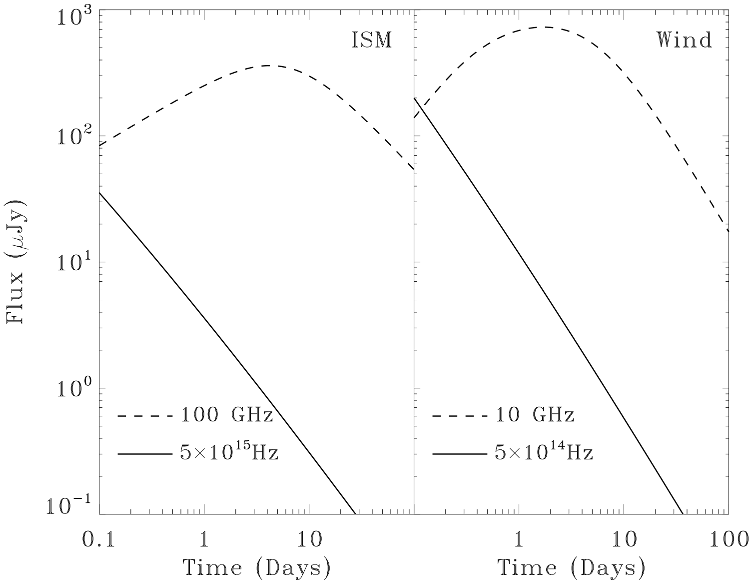

Figure 3.3: Theoretical light curves illustrating the passage of break frequencies through observed wavelength bands. The left panel shows an ISM-like case, the right, a Wind-like one. Solid lines show a high frequency (optical/UV), dashed, a low one (radio/submillimeter). In both cases, the electron energy index is $p = 2.2$; Wind-like flux evolution is steeper. In the ISM-like case, a subtle steepening occurs around Day 1 as ν_c passes below the UV. The submillimeter rises until ν_m passes below near ten days. In the Wind-like case, a subtle steepening occurs in the optical as ν_c passes above the band after a few days. The radio band is initially in the self-absorption spectral region, rising steeply until ν_a passes below the frequency at a fraction of a day. It then plateaus until the peak ν_m passes below the band after a few days. (ISM-like parameters: $E = 10^{52}\,$ergs, $n = 1\,\mathrm{cm}^{-3}$, $z = 1$, $\epsilon_B = 0.01$, $\epsilon_e = 0.25$, $p = 2.2$. Wind-like parameters: $E = 10^{52}\,$ergs, $A = 0.1\,A_*$ ($\rho = 5 \times 10^{11}\,A_*\,r^{-2}$ g cm^{-1}), $z = 1$, $\epsilon_B = 0.05$, $\epsilon_e = 0.05$, $p = 2.2$.)

difference in the rate at which the flux rises for frequencies above and below ν_a. In both cases, they rise as the peak nears, as $t^{1/2}$. For the Wind-like case, the shock encounters an increasingly rarefied circumburst medium and the self-absorption, sensitive to the average density, drops. At a relatively low frequency, such as the 10 GHz shown, the rise is initially proportional to $t^{1/2}$ in the optically thick region. The flux then plateaus once it becomes optically thin, until the peak reaches the observed frequency. The flux in a particular band need not rise to the peak levels observed at higher frequencies, since the peak drops in time in the Wind-like case.

Above the peak, the spectral slope depends upon the electron energy index p. Thus, the flux density declines at a p-dependent rate. The temporal index for frequencies just above the peak is $-0.75(p-1)$ in the ISM-like case and $-0.75(p-1/3)$ in the Wind-like one. These are ~ -1 for $p \approx 2-2.5$. In the ISM-like case, a frequency will initially be $\nu_m < \nu < \nu_c$. ν_c sweeps down past the frequency and the decline steepens by 1/4 in the temporal index for $\nu > \nu_c$. In the Wind-like case, ν_c is sweeping upward, but the decline is steeper for $\nu < \nu_c$. For $\nu > \nu_c$ the temporal index is $-0.75(p - 2/3)$. For the Wind-like case, initially the frequency is at $\nu > \nu_c$. After ν_c passes, in the region $\nu_m < \nu < \nu_c$, the decline is steeper (again by 1/4). The only observational difference in the two density profiles' cooling break passages is that in the ISM-like case it would be first seen at high frequencies and then lower ones would steepen. The Wind-like case would have the steepening begin at lower frequencies passing out to higher ones.

With a smooth spectrum, the passage of a cooling break is subtle, as evident from Figure 3.3. A greater degree of change will be seen in the light curves if there is a "jet break", which occurs when collimation of the ejecta becomes evident. To a good approximation, the ejecta's outward motion stalls as it expands in its rest-frame. Rhoads (1997) finds the bulk Lorentz factor of the shock drops exponentially with shock radius as it expands, thus the shock will not expand outward significantly without reaching a non-relativistic phase. Returning to Equation 3.2, this implies that the Lorentz factor $\gamma \propto t^{-1/2}$. By similar calculations as before, this gives

$$F_{\nu,max} \propto t^{-1}, \quad \nu_a \propto t^{-0.2}, \quad \nu_m \propto t^{-2}, \quad \nu_c \propto t^0 \, . \tag{3.3}$$

These results do not depend upon the density profile assumed. The density will be unchanged during this evolution since the shock radius r is essentially unchanged. As a result, in either case the following spectral behaviour holds for the canonical break frequency ordering. For frequencies below the peak, the flux plateaus for self-absorbed frequencies. As the shock expands sideways, the average density drops, as does the self-absorption frequency. Then as a frequency enters the optically thin regime, its flux begins to decline as $t^{-1/3}$. Above the peak, as ν_c is stalled, the behaviour does not depend upon the observational frequency's relation to the cooling break. All frequencies above the peak will have their flux decline as t^{-p}. That is, a temporal index ~ -2. The change in temporal index is far more significant than a cooling break passage; generally the index steepens, decreasing in value by about one. At low frequencies, the flux will go from rising to either a decline or a plateau followed by a decline in the ISM-like case. In the Wind-like case, the flux will go from rising to a plateau in the optically thick region, and a plateau to a decline in the optically thin region below the peak.

3.3 No Data Left Behind: Comprehensive Broadband Fits

Our model provides the full flux densities of the fireball's forward shock at each frequency and time. We fit it to all data from radio to X-ray frequencies. This ensures that the maximum amount of information from the data is used to provide model constraints and that the result is consistent in all frequency regimes. The flux model is developed from fundamental physical parameters of the event. This permits self-consistent corrections to be applied to the synchrotron flux model, such as radiative losses tied to the energy available in the electrons.

This comprehensive method, when applicable, is superior to simpler, more limited implementations of the fireball model. The simplest use of the fireball model is an "α,β" analysis in terms of the expected $F_\nu \propto \nu^\alpha t^\beta$, as presented by Sari, Piran & Narayan (1998) for the isotropic evolution, or with the addition of a jet break (Sari, Piran & Halpern, 1999). The parameters α and β are *asymptotic* behaviour limits. If far enough from any transition (a jet break or the passage of a spectral break), each behavioural regime in the model has a functional dependence of one index upon the other. That is, $\alpha = f_i(\beta)$, as both α and β are various functions of the electron index p. The index i indicates both a particular spectral region relative to the breaks and a particular dynamic regime, depending upon the form of circumburst density distribution and the presence of a jet edge. This form of analysis is often appropriate for a data set which does not have sufficient spectral and temporal baselines to constrain a broadband fit (such as by Halpern *et al.* 1999 , Jaunsen *et al.* 2001, and Vrba *et al.* 2000 for GRB980519, and by Price *et al.* 2002, 2002b for GRB010921), allowing some constraints on the parameters to be developed (e.g., t_{jet}, p, presence of host extinction) even when there is no way to produce a single set of fireball parameters for a "best fit model". The dependences between α and β produce "closure relations" to satisfy for each spectral regime ($\alpha - f_i(\beta) = 0$). The indices α and β show which closure relations are compatible with the data. When only one circumburst density distribution's relations can be satisfied, as for GRB011121 (Price *et al.*, 2002b), this indicates the form of the circumburst density distribution. However, the best constraints on α and β are in the optical, and extinction (either uncertainty in Galactic de-reddening or in the amount of host extinction) will significantly impact the spectral index α, making even these determinations uncertain.

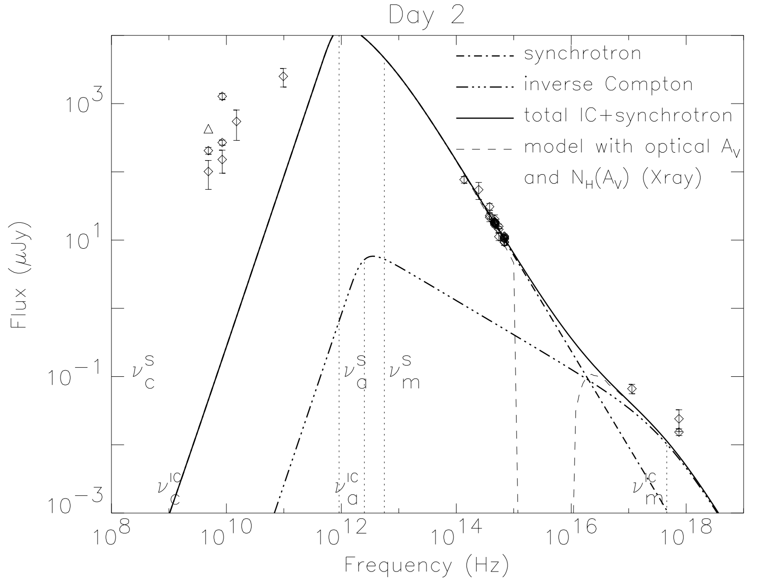

Figure 3.4: GRB 000926 spectrum relative to a high-density model, demonstrating the need for broadband modelling. Data is taken from one to three days post-burst, scaled forwards and backwards in time as calculated using the high-density model (overplotted). The relative deviations are those of the observed data from the model at the time of observation. The data, corrected for host extinction, are shown by diamonds, with $1\,\sigma$ errors. Data that are not $2\,\sigma$ detections are shown as $2\,\sigma$ upper limits (triangles). The solid line is the best-fit model assuming a density $n = 4 \times 10^4 \mathrm{cm}^{-3}$ and a collimation $\theta = 25°$, without host extinction, and the dashed line shows the model with the extinction. The high density is taken from the modelling of Piro *et al.* (2001), which only used optical and X-ray light curves from this event. They invoked a moderately collimated fireball and this dense medium to provide a rapid non-relativistic transition. The radio data reveals that this interpretation does not match the event, as the best broadband model with the collimation and density fixed at their values severely underestimates the radio data. The self-absorption frequency is a decade too high to match the observations, predicting an 8 GHz radio flux of $\sim 0.2\ \mu$Jy, whereas the flux measurement is near 200 μJy. The fit is from a preliminary method where host components had to be subtracted from the data and the evolution was assumed to be fully adiabatic, with no energy corrections applied. The locations of the synchrotron spectral breaks ν_a^s, ν_m^s and ν_c^s (for self-absorption, minimum injected electron energy, and cooling) are indicated, as well as the corresponding breaks for the IC spectrum. The IC spectral break labels are placed below the synchrotron labels. Each break frequency is noted by a dotted line that is only plotted to the height of its spectral component (synchrotron or IC). The synchrotron cooling break ν_c^s is at the edge of the plot, with its label visible above the spectrum.

Given sufficient spectral coverage over a limited time, a "snapshot spectrum" (the broadband spectrum interpolated to one point in time) can be developed. With coverage from X-ray to GHz radio, the peak and break frequencies of the broadband spectrum can generally be fit (e.g., GRB970508 and GRB971214, Wijers & Galama, 1999). Coverage will inevitably be spotty since there are no instruments available to cover all wavelengths. The coverage is limited to some radio wavelengths, the optical-NIR bands and perhaps an X-ray band, as described in Chapter 2. With large gaps in the observed spectrum, break frequency fitting requires some assumptions about the spectral shape. The spectral shape is assumed to match the synchrotron properties, rather than being fit in order to test the theory. This method may ignore the possibility of spectral properties being masked by effects along the line of sight, such as extincted optical light, or variability in the radio light from scintillation, as explained in further sections. Moreover, as the observables are the spectral breaks and not the underlying parameters, this method suffers from uncertainty in its inversion to physical parameters. Sari & Esin (2001) show that a snapshot spectrum can be solved in the basic fireball model with two separate parameter solutions: with the cooling dominated by either the synchrotron emission or the Compton scatters of these photons off the electron distribution. These solutions evolve differently in time and can be distinguished only by observations at other times.

Providing the data to constrain all the spectral breaks at one time is a difficult observational task. A better method is to fit to the light curves by evolving the model flux. A time is selected at which to fit the break frequencies, and the model flux at other times is derived from the synchrotron spectral shape and expected break frequency evolution. The breaks can then be inverted to give the underlying parameters under the assumptions of the fireball model (e.g., GRB000301C, Berger *et al.*, 2000). This method does suffer from some uncertainty. Since the fit is not on parameters such as the electron energy fraction ϵ_e, consistent radiative energy corrections cannot be calculated and are not included. Moreover, the evolution used is that of the pure synchrotron flux without considering if inverse Compton (IC) scatters may significantly impact the cooling rate. Finally, the inversion to fireball parameters is uncertain, as it is effectively that of a snapshot spectrum.

We attempt to use all of the data set's $f_\nu(\nu, t)$ points. These are fit to the flux density model calculated from fundamental parameters. This method makes maximum use of a data set's power to constrain the model, fitting part of the evolving spectrum to the data available at each time. In some sense the method resembles using all of the data extrapolated to a best average spectrum. It ignores no spectral region. As shown in Figure 3.4, such an omission (of all radio information) can lead to a poorly constrained model, inconsistent with the full data set. The use of fundamental parameters as the basis of the modelled evolution allows the development of self-consistent corrections to the main synchrotron emission, as elaborated further in the next section.

3.4 Calculating the Emission: Fireball Precision and Accounting for Corrections

Having explained the model assumptions (§3.1), its basic behaviour (§3.2), and the philosophy of the fit method (§3.3), we now turn to the details such as corrections to the pure synchrotron flux and processes that alter the flux on its path from the emitter to the observer.

We employ the previously published fireball model calculations for the spectral breaks. The published equation prefactors account for the spatial distribution of relativistic electrons behind the shock and integrate the equal arrival-time surfaces over the shock. Calculations employing these prefactors give a better estimate of the spectral break values than order of magnitude prefactors for the analytic solutions for spectral breaks. (Order of magnitude equation prefactors are calculable from the method of §3.2 by retaining the equation dependences upon such constants as m_e.)

The isotropic case is taken from the relativistic near-adiabatic equations of Sari, Piran & Narayan (1998), with equation prefactors from Granot & Sari (2002) (their canonical order, Table 2) for a Wind-like circumburst medium (CBM), and from Sari, Piran & Narayan (1998); Granot, Piran & Sari (1999a,b) for an ISM-like CBM. The resulting equations are

$$\begin{array}{lcll} F_\nu^{max} & = & 1600\,(z+1)\,D_{28}^{-2}\,\epsilon_{B,-2}^{0.5}\,E_{52}\,n^{0.5} & \mu\mathrm{Jy} \\ \nu_a & = & 4.2\times10^{8}\,(z+1)^{-1}\,f_I(p)\,\bar{\epsilon}_e^{-1}\,\epsilon_{B,-2}^{0.2}\,E_{52}^{0.2}\,n^{0.6} & \mathrm{Hz} \\ \nu_m & = & 3.3\times10^{14}\,(z+1)^{0.5}\,\epsilon_{B,-2}^{0.5}\,\bar{\epsilon}_e^{2}\,E_{52}^{0.5}\,t_d^{-1.5} & \mathrm{Hz} \\ \nu_c & = & 6.3\times10^{15}\,(z+1)^{-0.5}\,\epsilon_{B,-2}^{-1.5}\,E_{52}^{-0.5}\,n^{-1}\,t_d^{-0.5} & \mathrm{Hz} \end{array} \tag{3.4}$$

for the ISM-like CBM, where $f_I(p) = (\,(p+2)(p-1)/(3p+2)\,)^{0.6}$ and $\bar{\epsilon}_e = \epsilon_e(p-2)/(p-1)$. For the Wind-like CBM:

$$\begin{array}{lcll} F_\nu^{max} & = & 7700\,(p+0.12)\,(z+1)^{1.5}\,D_{28}^{-2}\,\epsilon_{B,-2}^{0.5}\,E_{52}^{0.5}\,A_*\,t_d^{-0.5} & \mu\mathrm{Jy} \\ \nu_a & = & 3.3\times10^{9}\,(z+1)^{-0.4}\,f_W(p)\,\bar{\epsilon}_e^{-1}\,\epsilon_{B,-2}^{0.2}\,E_{52}^{-0.4}\,A_*^{1.2}\,t_d^{-0.6} & \mathrm{Hz} \\ \nu_m & = & 4.0\times10^{14}\,(p-0.69)\,(z+1)^{0.5}\,\epsilon_{B,-2}^{0.5}\,\bar{\epsilon}_e^{2}\,E_{52}^{0.5}\,t_d^{-1.5} & \mathrm{Hz} \\ \nu_c & = & 4.4\times10^{13}\,(3.45-p)e^{0.45p}\,(z+1)^{-1.5}\,\epsilon_{B,-2}^{-1.5}\,E_{52}^{0.5}\,A_*^{-2}\,t_d^{0.5} & \mathrm{Hz} \end{array} \tag{3.5}$$

where $f_W(p) = (\,(p-1)/(3p+2)\,)^{0.6}$. The units are: D_{28} = luminosity distance in 10^{28} cm, $\epsilon_{B,-2} = \epsilon_B$ in %, n = density in cm^{-3}, A_* = density scaling for the Wind-like profile so that $\rho = 5\times10^{11}\,A_*\,r^{-2}$ g cm^{-1} (r in cm; a standard reference for a mass loss of 10^{-5} M$_\odot$ yr^{-1} at a wind speed of 1000 km s^{-1}), E_{52} = isotropic-equivalent energy in units of 10^{52} ergs, and t_d = observed time post-burst in days. The electron energy partition ϵ_e is given as a fraction and z is the redshift.

We use a smooth shape for a spectrum with $f_\nu \propto \nu^{\beta_1}$ before a break ν_b and $f_\nu \propto \nu^{\beta_2}$ after ν_b. These are connected by factors of $(\nu/\nu_b)(1+(\nu/\nu_b)^{\beta_1-\beta_2})^{-1}$ for $\nu_b = \nu_m$ or ν_c, and for ν_a we use the physically motivated prescription of Granot, Piran & Sari (1999a).

The post-t_{jet} evolution with laterally expanding ejecta uses the prescription of Sari, Piran & Halpern (1999) (Eqs. 2-5, the scalings as described in §3.2), and is connected to the pre-jet behaviour without smoothing (i.e., a sharp jet break).

Using the relativistic equations for the shock energy, $E = M\gamma^2$, we calculate the time at which $\gamma = 1$ as the non-relativistic transition, t_{nr}. This would be equivalent to using the Blandford & McKee (1976) approximation for the energy, $E = M\gamma^2\beta^2$ where $\beta = v/c$, and defining the non-relativistic transition condition as $\gamma\beta = 1$. We again employ a sharp transition to the post-t_{nr}

behaviour.

This pure synchrotron spectrum is adjusted with self-consistent corrections to the cooling rate, from the parameters already enumerated. Based upon the work of Sari & Esin (2001), we calculate the effects of synchrotron photon upscatters (inverse Compton scatters, IC) off the shocked electrons. First, we consider Y, the IC to synchrotron luminosity ratio; for $Y > 1$, $Y \approx (\max[(\gamma_c/\gamma_m)^{2-p},1]\, \epsilon_e/\epsilon_B)^{1/2}$. When $Y > 1$, IC dominates the electron cooling and we adjust the cooling break ν_c by $(1+Y)^{-2} \approx Y^{-2}$. Furthermore, the Compton upscattered photons can produce a high-frequency secondary source of flux. We adopt spectral breaks for this component of $\nu_m^{IC} = 2\gamma_m^2 \nu_m^{synch}$, $\nu_c^{IC} = 2\gamma_c^2 \nu_c^{synch}$, and $\nu_a^{IC} = 2[\min(\gamma_m, \gamma_c)]^2 \nu_a^{synch}$. We employ the same spectral slopes between the breaks as for the synchrotron spectrum, which are accurate save for the slope for $\nu < \nu_a^{IC}$, where IC flux never dominates the data. As the spectral shapes are similar, we simply relate the IC peak flux to the synchrotron peak flux by the ratio expected for the total fluxes, the photon interaction probability. The probability is the total area presented by all electrons (the number of electrons times σ_T, the Thompson cross-section) divided by the shock area. The result is $n\,\sigma_T\, r/3$ for the ISM-like case.

We also treat radiative corrections self-consistently. Instantaneously, we treat the shock as adiabatic. The energy is calculated for each time from the solution of dE/E (Cohen, Piran & Sari, 1998), as explained in more detail in Appendix B. It depends upon the ratio ν_c/ν_m in slow cooling ($\nu_c > \nu_m$), where the energy loss rate decreases, as this ratio determines the fraction of electron energy that can be radiated efficiently. We use the synchrotron-only rate of change in ν_c, allowing a simple analytic solution for $E(t)$. As this is when $E(t)$ changes are becoming unimportant, the approximation has little effect. We scale the shock's energy to the value at the change from fast- to slow-cooling regimes (when $\nu_c = \nu_m$, fairly early).

Our model also accounts for extinction and interstellar scintillation (ISS), effects upon the spectrum on its way to the observer, and the host's flux. ISS in the Galaxy distorts the flux at low (radio) frequencies. We estimate its fractional flux variations as outlined by Walker (1998) for point sources, using the map of scattering strengths by Taylor & Cordes (1993), and scalings for extended sources as explained by Narayan (1992). The growing angular size reduces the scintillations; we assume initial parameters in the model to get angular size as a function of time for the ISS model. These are not iterated, but used as an additional uncertainty in the *model* flux, added in quadrature to the data's uncertainties when estimating χ^2.

For extinction, we first de-redden for Galactic effects using Schlegel, Finkbeiner & Davis (1998)'s method for estimating A_λ (the magnitudes of extinction at each wavelength) in the optical. Their dust maps provide measures of $E(B-V)$, the difference in the extinction magnitudes at blue (B band) and green (V band) wavelengths. Schlegel, Finkbeiner & Davis (1998) provide Galactic conversions from this to A_λ. The conversion factors vary from a few at visual wavelengths, to small fractions in the infrared where extinction is minimal. As most GRBs with good followup are at high Galactic latitudes, the resulting terms are small.

We use known local extinction curves redshifted to the host rest-frame to fit for host contributions, as the extinction curves in high-redshift galaxies are unknown. The model allows for three options: the Large Magellanic Cloud (LMC), Small Magellanic Cloud's Bar (SMC) and the Milky Way (MW) extinction laws, as presented by the data in Weingartner & Draine (2001). For computational simplicity, we fit the Weingartner & Draine (2001) data for each to a six-parameter general formulation of extinction laws from the rest-frame optical to the UV. We use the formulation of Reichart (2001), connecting the extinction parameterizations of Fitzpatrick & Massa (1988); Cardelli, Clayton & Mathis (1989). In general we use the LMC law, but in one case (see the discussion of the GRB 980329 fits) we used the SMC law due to evidence that the host's extinction law is steep.

We do not subtract host fluxes as the resulting decay slope is sensitive to small differences in the subtracted host value. Instead we add host fluxes to the model in the fit. In the optical and near-IR, when there is evidence for a host component, we fit a value for the particular band(s) involved. As submillimeter hosts have been detected in other bursts (Hanlon *et al.*, 2000; Berger, Kulkarni & Frail, 2001; Berger *et al.*, 2001b; Frail *et al.*, 2002; Berger *et al.*, 2003), we allowed for this possibility (scaled to 350 GHz as ν^3), but none was required for the four events under consideration and this component was not included in the best fits. Finally, we see in two data sets evidence for underlying flux in the radio. 980703 has sufficient data that a spectral index, -0.32 (Berger, Kulkarni & Frail, 2001), was determined and we fit the radio host flux scaled to 1.43 GHz (the observed frequency where it is brightest). For 980329 we use a canonical spectral index of $\nu^{-0.8}$, again scaled to 1.43 GHz.

Two other groups have performed full analyses similar to ours, Chevalier & Li (Chevalier & Li, 2000; Li & Chevalier, 2001a) and Panaitescu & Kumar (Panaitescu & Kumar, 2001b,a, 2002). There are some differences in each group's approach to the fireball model. Chevalier & Li develop an r^{-2} CBM model, including analytic solutions to the hydrodynamics, but they do a numerical solution to get the full smooth spectral shape. They assume an extra break in the electron energy distribution but do not account for energy losses, IC cooling or ISS effects.

Panaitescu & Kumar numerically solve the dynamics, while we employ the analytic solutions of the dynamics in asymptotic regimes. These asymptotic solutions are accurate except close to a dynamic transition (i.e., to the non-relativistic phase). Both methods utilize approximations to calculate the spectral shape. They numerically calculate the spectrum from the flux with equal arrival times from the shock surface. We use a simple smoothing between spectral breaks whose evolutionary equations are adjusted for arrival time effects and the emission from electrons behind the shock. They calculate IC scatters and energy losses from their modelled spectrum. In contrast, we apply IC effects based upon the ratio of IC and synchrotron luminosities, and use consistent, pre-calculated energy losses dependent upon the electron energy fraction. The theoretical calculations for IC effects and energy losses account for the synchrotron spectrum, so the end result in both cases is ultimately the same; our method, using analytic results, is computationally simpler. In addition, they use the simplest electron energy distribution when it provides a good solution but also allow for two (rather than one) indices in the injected spectrum if needed. They pre-account for host effects by subtracting fluxes and fixing extinction levels, instead of including these in the fits.

3.5 Nuts, Bolts and Program Code: Input and Implementation

The full set of model parameters includes those from the explosion, the microphysics and environment as previously discussed, and those governing line of sight modifications. The event parameters are the isotropic-equivalent kinetic energy (tied to the time when fast cooling ends in the case of energy corrections), E, and the initial half-opening angle θ of collimated ejecta. Any $\theta > 1$ is treated as purely isotropic evolution. The shock microphysics parameters are the fraction of energy imparted by the shock to the magnetic fields, ϵ_B, and to the swept-up electrons, ϵ_e, as well as the power law index of the accelerated electrons' energy distribution, p. The environment is parameterized by the CBM's density, n for the ISM-like constant profile, and A ($\rho = Ar^{-2}$) for the Wind-like r^{-2} profile. The selection of profile is by a flag that switches to the independent sets of Equations 3.4 and 3.5.

Parameters describing flux modifications along the line of sight include local extinction and host galaxy flux. Extinction may occur in the GRB environment or on its line of sight through the host galaxy. The host galaxy flux will add to the observed flux level if the event and its host are not discriminable by the observing instrument. Extinction is parameterized by the overall level, tied to the magnitudes of extinction in the V band in the host frame, as well as by the extinction law. The extinction law is flagged to one of the 3 options (LMC, SMC, MW) as described in the previous section. The extinction law, as it is set by values for the Reichart (2001) extinction parameters, could also be fixed at any user-defined value to customize the type of extinction. In practice the data are not of sufficient quality to warrant this. Host flux is dealt with differently depending upon the frequency region. Optical hosts are fitted with individual values for each wavelength band desired. Submillimeter hosts are parameterized by the flux at 350 GHz, and parameters to set the dust temperature and its turnover to a blackbody spectrum (although these are generally fixed to produce $f_\nu \propto \nu^3$). Radio hosts are parameterized by the flux at 1.43 GHz (the lowest VLA frequency) and the spectral index β, where $f_\nu \propto \nu^\beta$ has $\beta = -0.8$ as a canonical value.

The program to propagate these parameters to a flux model for comparison to the data was initially implemented in an IDL code. The program takes a grid of parameter starting points (each parameter being either fixed or allowed to fit) and performs a gradient search from each combination via the Powell algorithm (as implemented by Press *et al.*, 1988) for a multidimensional minimum search on the fit statistic function. Initially, the sole best-fit statistic considered was χ^2. The algorithm revises the directions searched in the parameter space at each step, beginning along each parameter. Its initial search step size can be set by multiplying these unit directions by the desired step. The method does not include estimates of parameter uncertainties, and responds to a non-converging gradient search by stopping after 200 iterations.

The first version did not allow host flux components (they were subtracted from the data), radiative corrections to the energy, or inverse Compton cooling corrections. We gradually tested and added these as described above. We also considered alternative best-fit statistics.

We added an extra weighting that could be applied to each point. Its purpose is generally to even out the effects of unequal sampling in different wavelength regions. As described in Chapter 2, there are numerous highly sensitive optical observatories but less sensitive or fewer instruments available for radio, submillimeter, and X-ray work. A typical good data set will have very few ($\lesssim 5$) X-ray measurements, a handful of submillimeter points, dozens of radio observations, and $\sim$100 optical points. Giving equal weight to the ensemble of optical points as to that of the X-ray allows a search of parameter space for a solution that fits all frequency regions, not sacrificing one with few data for the sake of some improvement elsewhere.

We implement ISS uncertainties in the radio by adding to the data uncertainties the expected flux variation due to ISS. These are based upon a fraction of the model flux that can be substantial at early times. With a simple χ^2 statistic, there is a bias to models that overestimate early radio data, then overlap the data points with the large applied ISS uncertainties. We avoid this bias by using $-ln(P)$ as the fit statistic to minimize, where P is the probability of all the points' deviations from the model. Assuming Gaussian-distributed uncertainties for the individual data points i gives

$$-ln(P) = 0.5 \times (\chi^2 + 2\Sigma ln(\sigma_i)) + \text{constant} .$$

For a fixed set of uncertainties σ_i this fit statistic is equivalent to minimizing χ^2. A $-ln(P)$ fit statistic rejects excessive values for model-dependent uncertainties.

For computational speed, we translated the code running individual gradient fits into a C program; the IDL code took the better part of an hour to fit a single set of initial parameters, but the C code could typically perform the fit in under ten minutes. We have now produced a Perl code to input the grid of starting points, implement a loop over the grid, and print the output to files. We employ IDL to generate light curves and spectral plots from the fluxes output by the C code. To get a clearer picture of the code's capabilities, the commented input file is placed in Appendix C.

Chapter 4

Fitting Burst Events

The goal of GRB afterglow modelling efforts is to understand the environment and physics of the events, through deriving the parameters (enumerated in Chapter 3) that fit the data. To this end, as many well-sampled bursts as possible need to be fit to understand both the global applicability of the model and the diversity in the burst population. In this chapter we present the four best events from our work. In later chapters we will deal with some of the fit difficulties that have prevented the sample from being considerably larger.

Our development of the full comprehensive afterglow model as described in Chapter 3 evolved over time. We began with the pure synchrotron spectrum. This model evolves spectral breaks, but with the breaks' initial positions set by estimated fundamental parameters. The best sampled data sets required successive additions and refinements. For instance, the work of Sari & Esin (2001) showed that Compton cooling of the synchrotron spectrum could produce significant differences in the spectral evolution, differences that could be seen in a well-sampled event.

In this chapter we will partially review the development of the model to emphasize where the data drove the inclusion of physical effects. In particular, §4.1 elaborates an early effort with the well-sampled data set of the GRB 000926 afterglow. This work demonstrated the utility of a comprehensive model with the flux determined from fundamental parameters; these fundamental parameters also determine the significance of Compton cooling and radiative losses, of importance to this data set.

Then we present fits to four well-studied GRB afterglows with the comprehensive model of

Chapter 3, where we include the physical effects demanded by the data. The set of four fits are summarized in §4.2. We detail individual events in §4.3-4.6. As the first event studied, GRB 000926, required the inclusion of additional physical effects beyond the work of §4.1, we re-analyzed its data with the full model (§4.6).

4.1 Model Development: Working from Physical Parameters Indicated an Inconsistent Adiabatic Assumption

Work in the area of GRB afterglow modelling began with simple fits to the optical power law decay (e.g., Wijers, Rees & Mészáros, 1997) and broadband snapshot spectra (e.g., Galama *et al.*, 1998). A simple fireball model producing only synchrotron emission appeared to fit the data sets. Adopting the fundamental energetic, microphysical, and environmental parameters as the fit basis appeared to be a natural, uncomplicated method to describe the data. Under these assumptions, we began to fit data sets.

The model we initially employed was simpler than the basic model of §3.4. To keep the number of parameters small, we did not include host fluxes (when obvious, we subtracted the host flux component). We included the effects of inverse Compton scatters on the cooling rate and high-frequency emission, but we considered radiative corrections to the energy to be likely too small to be of any concern over the afterglow. Thus the model was completely adiabatic. If we accurately subtracted the host flux, and if little energy is available to radiate away, ignoring these effects is of small import. We were to discover this was not the case with our first major effort, the modelling of the GRB 000926 afterglow. The following discussion, beginning with a description of the data, is largely that of Harrison *et al.* (2001).

4.1.1 000926 Data

The Interplanetary Network detected GRB 000926 (Hurley *et al.*, 2000b) to a small positional uncertainty, allowing the discovery of its optical afterglow less than a day later (Gorosabel *et al.*, 2000; Dall *et al.*, 2000). Its redshift was 2.0369 ± 0.0007 as measured by absorption features in the optical spectrum (Fynbo *et al.*, 2000; Castro *et al.*, 2000).

The data garnered for this event includes significant radio, optical/NIR, and X-ray observations. The radio and submillimeter data was presented by the Caltech GRB group, with observations at 1.43, 4.86, 8.46, and 22.5 GHz by the *VLA*, 15 GHz data from the *Ryle* telescope, and 98.5 GHz data from *OVRO*. The optical/NIR data included the bands *BVRIJHK*, with *HST* data converted to *BVRI*, ground-based *BVRI* data from the Caltech GRB group (Price *et al.*, 2001), *J* from di Paola *et al.* (2000), and *JHK*, and *K*' from Fynbo *et al.* (2001a). We converted the *K*' data to *K* using the prescription of Wainscoat & Cowie (1992). X-ray observations by *BeppoSAX* and *Chandra* were also presented by the Caltech GRB group. Those observations were separated into soft (0.2–1.5 keV) and hard (1.5–8 keV) X-ray bands, with the central frequencies and flux densities determined assuming a spectrum of photon index $\Gamma = 2$. We determined the representative observation time by the expectation time of the observational interval, weighted by t^{-2}. We show the subset of the data near ten days post-burst in a broadband spectrum in Figure 4.1, and the X-ray light curves in Figure 4.2.

The data set used is as described above, with minor adjustments. The Galactic coordinates of the burst were $(l, b) = (78.9°, 37.3°)$, calculated from the coordinates of Gorosabel *et al.* (2000) with the NED Coordinate Calculator [1]. The optical data were corrected for the small Galactic extinction at that location, $E(B-V) = 0.0235$ (Schlegel, Finkbeiner & Davis, 1998). Flattening was visible in the late-time optical data (the *HST BVRI* observations, *R* seen in Figure 4.3). We subtracted host components fit from the light curves using a generic decaying function with a constant added (Harrison *et al.*, 2001). The first 8.46 GHz data point, about one day post-burst, is far above the 8.46 GHz fluxes for the rest of the first week, as shown in Figure 4.4. The variance is far more than scintillation estimates would predict—it was a significant outlier in the modelling and was excluded from the final analysis. It is likely associated with a separate component from the reverse shock.

---

[1] http://nedwww.ipac.caltech.edu/forms/calculator.html

4.1.2 Initial 000926 Fits

The data set presented a strong feature that any model fit must meet, a significant achromatic steepening in the optical light curves around Day 2 (seen in R in Figure 4.3). This feature suggests that a collimated model with a jet break could fit the data. Our initial fits attempted to search for fits near standard parameters (e.g., isotropic-equivalent energy $\approx 10^{52}$ergs, ISM densities ≈ 1 cm^{-3} or Wind outflow scale $\mathrm{A}_* \approx 1$); as expected from the optical break, no isotropic models provided a reasonable fit. The best fits are dominated by the post-jet evolution.

As the data set is dominated by post-jet evolution, it may be possible to have good fits with both ISM-like and Wind-like density profiles. With a well-fit model spectrum at the jet break, the model will evolve post-jet identically regardless of the circumburst medium's density profile. The identical evolution results from our approximation that the shock radius is nearly constant until one reaches the non-relativistic transition at late times. Any data in the non-relativistic phase would have low signal-to-noise; that transition is not clearly observable like the jet break.

To investigate the possibility that fits using the two density profiles could be indistinguishable, once a reasonable preliminary fit was found, we calculated its spectrum at the jet break time. This spectrum could be approximately inverted to the model's fundamental parameters for both ISM and Wind density profiles. Moreover, there are two cases of cooling that can produce a spectrum, as found by Sari & Esin (2001). These are the two limits $\eta\epsilon_e/\epsilon_B \equiv f \ll 1$, and $f \gg 1$. Here η is the fraction of the electron energy that radiates away, describing whether cooling is dominant (1 if $\nu_c < \nu_m$, $(\nu_c/\nu_m)^{(2-p)/2}$ otherwise (Sari & Esin, 2001)). If $f \ll 1$ (low IC case), the IC cooling rate is unimportant compared to that of synchrotron, whereas if $f \gg 1$ (high IC case) inverse Compton cooling dominates the total emission. This will change the evolution of the cooling frequency and so the flux densities in some frequency ranges. We used the four possible inversions of the spectrum as starting points in fits, checking whether the data set could be well-modelled for each case. Table 4.1 gives the results for the best fits in all four cases.

Table 4.1: 000926 Fit parameters for low- and high-IC ISM and Wind models with 1 σ errors, no energy corrections in the model.

Parameter	high-IC ISM	low-IC ISM	high-IC Wind	low-IC Wind
χ^2 for 114 data pts [a]	124	187	167	244
$t_{\rm jet}$ (days)	1.55 ± 0.14	1.31 ± 0.13	2.53 ± 0.45	1.38 ± 0.41
$t_{\rm nonrel.}$ (days)	70 ± 4	112 ± 7	119 ± 26	308 ± 152
$E_{\rm iso}^{b}$ (10^{52} erg)	18 ± 2	8.3 ± 0.9	43 ± 7	39 ± 8
n(ISM)$/A_*$(wind) [c]	27 ± 3 cm^{-3}	1.6 ± 0.2 cm^{-3}	3.5 ± 0.4	0.26 ± 0.02
p	$2.43\pm.06$	$2.20\pm.04$	$3.08\pm.03$	$2.25\pm.03$
ϵ_e (fraction of E)	$0.30\pm.05$	$0.16\pm.02$	$0.16\pm.01$	$0.018\pm.003$
ϵ_B (fraction of E)	$0.008\pm.003$	1.0	$0.005 \pm .002$	1.0
$\theta_{jet}(rad)$	$0.137\pm.004$	$0.099\pm.003$	$0.103\pm.002$	$.047\pm.003$
host A(V)	$0.12\pm.02$	$0.20\pm.02$	$0.00\pm.01$	$0.20\pm.02$

---

[a] First 8.46 GHz data point excluded as an outlier.

[b] Isotropic equivalent blast-wave energy

[c] $\rho = A_*(5 \times 10^{11})r^{-2}$g cm^{-1}

4.1.3 Necessity of Inverse Compton Considerations for the Best Fits

From Table 4.1 it is fairly unambiguous that the best model for the data set has (IC) Compton scatters dominating the cooling, and that the ISM-like density profile gives a better fit that a Wind-like profile. The model that best fit the broadband data is shown in Figure 4.1, with its broadband spectrum on Day 10, and compared to the low-IC ISM-like fit in the X-ray light curves of Figure 4.2.

The high-IC case is preferred in the X-ray regime because the low-IC fit systematically underpredicts the measurements. Those observations alone are insufficient to determine the presence of an IC component. It is only in the broadband model's context that the synchrotron flux estimates are insufficient at the X-ray frequencies. Even the spectral index is not conclusive. A secondary IC spectral peak will harden the X-ray spectrum over some time intervals as it passes through those frequencies (if it is comparable or dominant with respect to the synchrotron flux). There is but marginal evidence for such in the data, as the observed X-ray photon index is 1.9 ± 0.2 (Harrison *et al.*, 2001), and the expected value from the synchrotron flux is $p/2 + 1$, 2.2 for the high-IC ISM fit.

It is the expected X-ray flux given the optical and radio that is difficult to model without IC cooling dominance. The low-IC case where IC cooling is negligible has difficulty producing the required spectrum with reasonable parameters (for both the ISM-like and Wind-like density profiles).

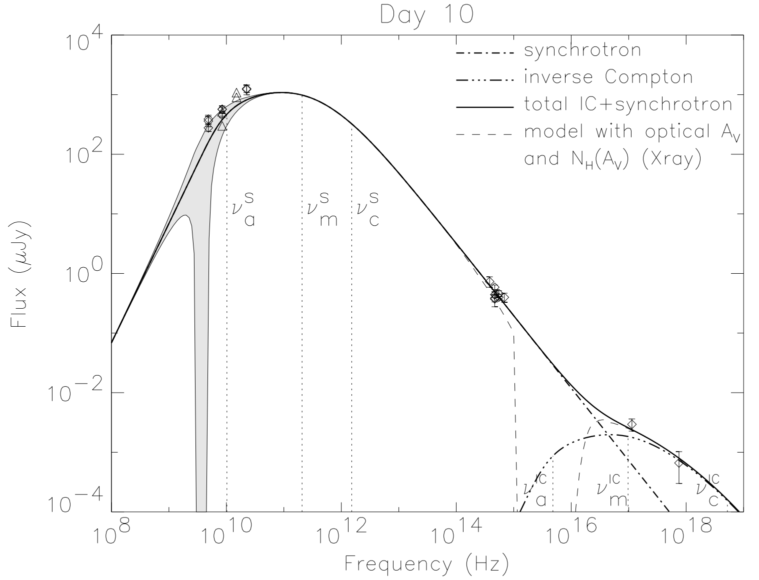

Figure 4.1: GRB 000926 broadband spectrum on Day 10 post-burst (after the jet break). Data is taken from five to fifteen days post-burst; model calculations extrapolate the points forward or backward in time. The errors represent the true relative deviation of the observed data from the model at the time of the observations. The data, corrected for host extinction, are shown by diamonds, with $1\,\sigma$ errors. Data that are not $2\,\sigma$ detections are shown as $2\,\sigma$ upper limits (triangles). The solid line is the best-fit model, without host extinction, and the dashed line shows the model with the extinction. The light grey envelope indicates the estimated model uncertainty due to interstellar scintillation, which is significant at radio frequencies. The fit is from a preliminary method where host components had to be subtracted from the data and the evolution was assumed to be fully adiabatic, with no energy corrections applied. The locations of the synchrotron spectral breaks ν_a^s, ν_m^s, and ν_c^s (for self-absorption, minimum injected electron energy, and cooling) are indicated, as well as the corresponding breaks for the IC spectrum. It is evident that the approximation made in assuming the IC spectrum has the same slope below the self-absorption break as the synchrotron spectrum is not an issue in fitting the data. The synchrotron flux dominates below ν_a^{IC}.

The low-IC case requires less energy in the electrons than the magnetic field ($\epsilon_e < \epsilon_B$). Initially the parameters were allowed to vary without limitation, but they required far more energy in the post-shock magnetic field than was available ($\epsilon_B \gg 100\%$). Even those cases were not as good as the high-IC ISM-like fit. The evolutionary difference in the cooling frequency made the synchrotron-dominant fit worse for the optical than the IC-dominant fit. With ϵ_B fixed at the physical maximum of 1.0, the fits worsened somewhat (for the ISM-like case, from χ^2 of 178 to 187 for 114 data points). In addition to the large ϵ_B, the isotropic-equivalent energy of $\approx 10^{53}$ergs in the ISM-like low-IC case is smaller than the observed gamma-ray energy release. With small expected radiative corrections (small ϵ_e), this value derived from the adiabatic model should nevertheless be nearly the initial fireball energy after the GRB phase. This would imply that more than half the initial energy was

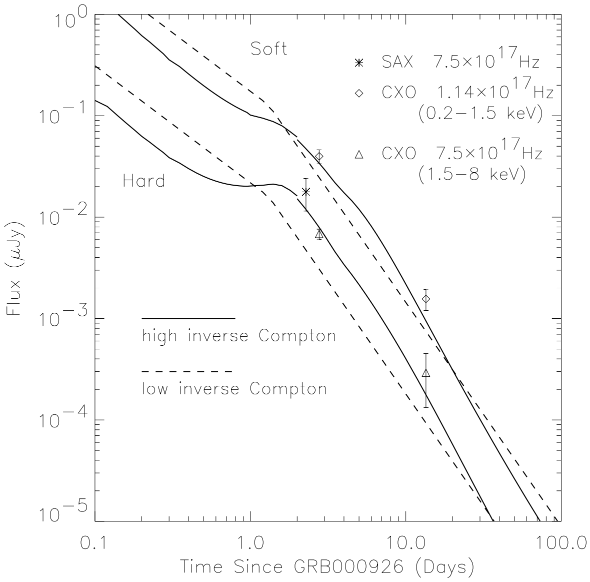

Figure 4.2: GRB 000926 X-ray afterglow lightcurve from *BeppoSAX* and *Chandra*. The *Chandra* data have been broken into two bands, hard (1.5–8 keV) and soft (0.2–1.5 keV), with center frequencies weighted by a photon index of 2. The data is corrected for absorption in our Galaxy. We show model calculations for both the best high- (*solid line*) and low-IC (*dashed line*) constant density ISM models. These fits are from a preliminary method where host components had to be subtracted from the data and the evolution was assumed to be fully adiabatic, with no energy corrections applied.

radiated as γ-rays, which is difficult to accommodate except with the most extreme assumptions in the theory (Beloborodov, 2000; Kobayashi & Sari, 2001).

The Wind-like model evolves quite differently pre-jet as the shock evolves in a significantly different density profile (see the Equations 3.4 and 3.5). The data set is dominated by the jet evolution (t_{jet} is ≈ 2 days) yet no Wind-like fit could be found as good as the best ISM-like fit. The high-IC Wind-like fit reproduced the X-ray flux reasonably well but under-predicts the 5 GHz data by a factor of 2–3. The low-IC Wind-like fit, which again required ϵ_B to be fixed at 100% as the preferred value was two orders of magnitude higher, was overall a poor fit, especially in the X-ray.

Early time optical or high-frequency radio (where scintillation is not causing large flux variations) data are particularly important in ruling out the Wind-like model assumption. Although the post-jet evolution $\gtrsim 2$ days is the same, even with observations beginning as late as 0.8 days, this data set was significantly better fit by an ISM-like density profile than a Wind-like one.

The differences in cooling rates between the synchrotron-dominated and Compton-dominated cooling routes for the shocked electrons provide significantly different model results. The observed model differences only become evident when the consistent IC corrections are taken into account by considering the fundamental physical parameters of the model.

Comptonization directly affects the rate at which ν_c evolves, dependent upon the relative amount of energy in the magnetic field and electrons (see §3.4). If the population of electrons has more energy than the magnetic fields which generate the synchrotron emission's photons ($\epsilon_e > \epsilon_B$), these synchrotron photons are quite likely to be capable of acquiring energy in an interaction with an electron via an inverse Compton upscatter. For such parameters, IC scatters dominate the cooling rate during the fast cooling stage where $\nu_c > \nu_m$, and during the slow cooling stage as long as $\epsilon_e(\nu_c/\nu_m)^{(2-p)/2} > \epsilon_B$. With the value of p near 2, for ϵ_e a factor of even a few greater than ϵ_B, IC dominance continues for a substantial period of the slow cooling phase. The excess cooling becomes required by self-consistency for a model that fits fundamental physical parameters (ϵ_e and ϵ_B) rather than observables such as break frequencies.

In order to have a significant amount of IC flux, the optical depth for IC upscatters must be substantial. The number of electrons must be sufficiently large to produce a large number of scatters that result in a large number of photons upscattered to high frequencies. This upscattered IC emission is proportional to the density, the peak fluxes for the IC and synchrotron components related by $n\,\sigma_T\,r/3$ in the ISM-like case (see §3.4). This is from the interaction probability for a photon, and does not directly depend upon ϵ_e and ϵ_B. Nevertheless, even with a somewhat low density that produces little IC flux, for $\epsilon_e > \epsilon_B$ there may still be significant IC cooling that affects the cooling frequency. The IC cooling results from a small number of scatters off the electrons. The electrons must be highly energetic, to maintain a significant ϵ_e; each scatter imparts a large energy to the photon. The upscatters produce a small number of highly energetic photons, potentially above the soft X-ray band.

The constraint that IC cooling and flux are required to properly fit this data set demonstrates the importance of self-consistent corrections to the model. Synchrotron flux alone is insufficient to properly account for the data in at least some cases. However, the mismatch between the model and data may not be evident for a model fit based upon observables (the spectral breaks) rather than the underlying parameters. A data set requiring IC would appear to be a poor fit to a model of observed spectral breaks changing as for an uncorrected synchrotron spectrum. A model drawn from fundamental parameters, with IC corrections, will only produce spectral breaks permitted by the IC-dominated or synchrotron-dominated cases. The spectral breaks' relationships include the differences in cooling rates; the two cases are distinct. With such a model a data set affected by IC will be a poor fit to the synchrotron-dominated case, yet fit the IC-dominated one.

4.1.4 Necessity of Radiative Corrections for Self-Consistency

This model also demonstrates that the non-radiative assumption may not hold. For IC cooling to dominate, the electron population's energy must dominate over the magnetic field energy, or $\epsilon_e > \epsilon_B$. The magnetic fields cannot be negligible, or insufficient synchrotron radiation would be produced in the afterglow. As a result, in at least some cases, ϵ_e will be significant (here estimated as $\epsilon_e = 0.3$). As the electron energy is also the energy available to radiate, such a large value is barely compatible with the adiabatic assumption that energy corrections are negligible.

The basic expectation of radiative corrections is that in the fast-cooling regime, where all electrons can cool and radiate significantly during the lifetime of the shock, the fractional energy losses per unit time are proportional to ϵ_e (Cohen, Piran & Sari, 1998). The result for the ISM-like case is $E(t) = E_o(t/t_o)^{-N}$, $N = (17/12)\epsilon_e$ at low ϵ_e (ISM-like case) and $N \to 9/13$ as $\epsilon_e \to 1$ (Cohen, Piran & Sari, 1998). In the slow-cooling regime, fewer electrons can significantly cool during their lifetime in the shock and the rate slows.

For $\epsilon_e = 0.3$, every energy dependence of break frequency or flux density has a corresponding time dependence of $\approx t^{-0.3}$. As an example, above both ν_m and ν_c, the energy dependence of the flux density is proportional to $E^{(p+2)/4}$. In a data set dominated by post-jet evolution, one would observe $\approx t^{-1.08p-0.16}$ rather than t^{-p}, potentially biasing the measured p by $0.08p+0.16$—with $p \approx 2$, by about $\Delta p = 0.3$.

The result that ϵ_e could be significant (partly as a result of the required IC cooling) provided an impetus to refine the model method to include energy corrections, minimizing the bias in measuring

p. The fit model culminated in the full basic model as described in Chapter 3, particularly §3.4. The set of events was fit to the full basic model (including 000926, for which this work was used as a starting point).

4.2 Full Model Fits with Self-Consistent Radiative Energy Losses

The previous section motivated the model development, including corrections required for self-consistency. The addition of inverse Compton effects (additional cooling and upscattered flux) produced significant differences in the goodness of the model's fit. Model parameters require more energy available to radiate than is consistent with adiabaticity. Here we describe fits to four events using the full model and its implementation as presented earlier in Chapter 3. As discussed in§3.5, we used $-ln(P)$ as the fit statistic, which avoids biasing with the scintillation uncertainties.

We produced reasonable fits to four of the very best broadband data sets available. (Some other data sets were also fit, with poor results; they are discussed in Chapter 6.) These four events, the afterglows of GRBs 970508, 980329, 980703 and 000926 are fairly typical of long-duration bursts. Their redshifts vary from $z = 0.835$ to (at least) 2.0369 (see the discussion concerning 980329's redshift in §4.4). Nevertheless, they do demonstrate some of the potential difficulties in interpreting afterglow observations. As will be discussed in their individual sections following, there was some anomalous brightening of the 970508 fluxes, and no redshift could be measured for the 980329 event, although some constraints were possible.

To compare the fit quality, we show here three summary Figures (4.3, 4.4, 4.5), giving the model fit in the three main frequency regimes: radio, optical, and X-ray. As the radio and optical data sets are typically multiband, these figures show the generally most data-dense wavelength bands: the 8.46 GHz band in the radio and the R filter in the optical (peaking around 4.7×10^{14} Hz). However, each has significant radio, optical, and X-ray data, with data sets totalling from 105 to 268 data points.

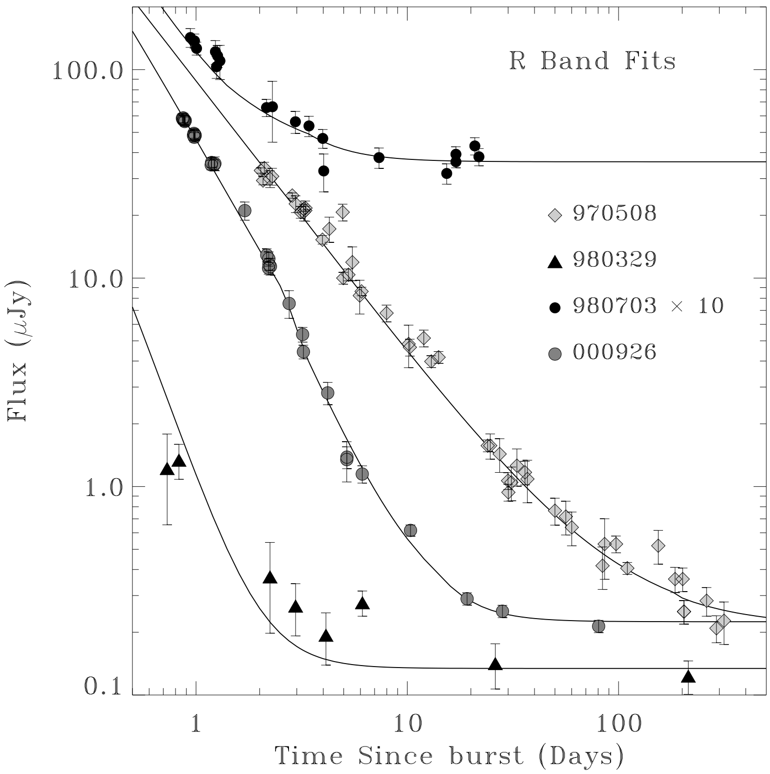

Figure 4.3: Subsets of the optical data from the best fits—the R band light curves for the four events. For data selection, see §4.3–4.6. The fits shown are to the full broadband data sets, with typically 100+ DOF, and are detailed in Table 4.2. The GRB 980329 optical data is not very constraining for the decay rate—a late optical detection (the early points were found on re-analysis) did not allow deep followup over the first week. The scatter in the GRB 970508 data cannot be explained in any simple model, but otherwise the fits are quite good.

As can be deduced from these figures, the models match the data's trends quite well, even though there may be some significant outliers (e.g., the 980329 R point at one week post-burst, and the 980703 8.46 GHz data at < three days).

The results (fit parameters) are summarized in Table 4.2. As can be seen, the χ^2 per degree of freedom (DOF) is quite large. Formally, these fits are not good. As calculated from the χ^2 test, the probability P that the model fully represents the data is 2.3×10^{-37}, 0.041, 0.102, and 0.0012, respectively for the 970508, 980329, 980703, and 000926 events. Three of these would be rejected as beyond the $2\,\sigma$ confidence level (acceptable requiring $P \geq 0.0455$), and two would be rejected even as being $3\,\sigma$ (acceptable requiring $P \geq 0.0027$) probable that the fit model does not represent the data's source distribution. These are the best results, not anomalies; it lends doubt to the hypothesis that the basic fireball model fully describes the afterglow. In further chapters the fireball model's

Table 4.2: Fit parameters of the best basic models. Statistical uncertainties are given for the primary (employed in the fit) parameters; the other columns are derived from the fitted values. The quoted uncertainties are produced via the Monte Carlo bootstrap method with 1000 trials to generate the parameter distribution. The values bracket the resulting 68.3% confidence interval.

χ^2	DOF	t_{cm}^{a}	t_{jet}	t_{NR}	E [b] t_{cm}	E 1 day	n cm^{-3}	p	ϵ_B %	ϵ_e	θ_{jet} rad	A(V) host
GRB 970508												
596	257	0.082	183	203	$3.7^{+0.1}_{-0.1}$	1.6	$0.20^{+0.01}_{-0.02}$	$2.1223^{+0.003}_{-0.0008}$	$25.0^{+0.6}_{-2}$	$0.342^{+0.008}_{-0.01}$	$0.84^{+0.03}_{-0.03}$	$0.14^{+0.02}_{-0.02}$
GRB 980329												
115	90	6.1	0.12	70	126^{+6}_{-6}	170	20^{+5}_{-5}	$2.88^{+0.1}_{-0.2}$	17^{+3}_{-3}	$0.12^{+0.02}_{-0.02}$	$0.036^{+0.002}_{-0.004}$	$1.9^{+0.2}_{-0.1}$
GRB 980703												
170	147	1.4	3.4	50	$11.8^{+0.8}_{-2}$	13	28^{+4}_{-3}	$2.54^{+0.04}_{-0.1}$	$0.18^{+0.04}_{-0.03}$	$0.27^{+0.03}_{-0.03}$	$0.234^{+0.02}_{-0.007}$	$1.15^{+0.08}_{-0.06}$
GRB 000926												
138	93	3.4	2.6	79	12^{+2}_{-2}	15	16^{+3}_{-3}	$2.79^{+0.05}_{-0.04}$	$2.2^{+0.5}_{-0.6}$	$0.15^{+0.01}_{-0.01}$	$0.162^{+0.007}_{-0.004}$	$0.022^{(<0.037)}$ [c]

---

[a] Time when fast cooling ends at $\nu_c = \nu_m$.

[b] Isotropic equivalent blast-wave energy (not corrected for collimation), at the time when $\nu_c = \nu_m$. All tabled energies are in units of 10^{52} ergs, and isotropic-equivalent.

[c] No lower constraint on this extinction value; 68.3% confidence interval is < 0.037.

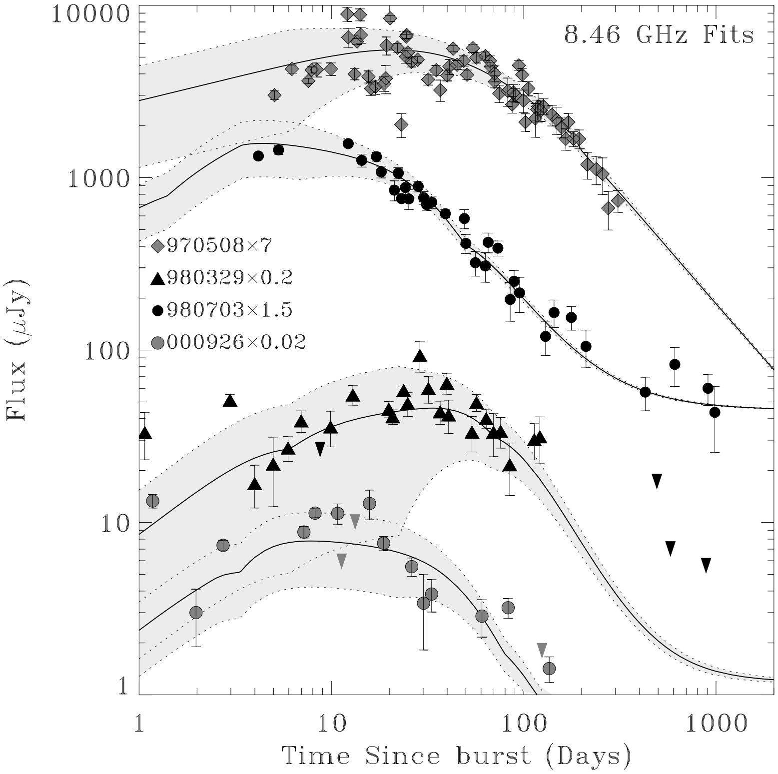

Figure 4.4: 8.46 GHz light curves of the four events, with the best fits (see Table 4.2). The light grey envelopes show the model uncertainty estimate due to interstellar scintillation. Data that is not statistically significant at the $2\,\sigma$ level are presented as $2\,\sigma$ upper limits (downward triangles). As explained in §4.4 the data for GRB 980329 prior to Day 4 was not included in the fit as it likely contains an excess contribution from the reverse shock. The first data point for 000926 is likewise excluded, as explained in §4.1.1. The 980329 radio host component improves the fit only marginally, due to a 1.43 GHz average excess, which may indicate a weak radio host flux. The fits are overall quite good, although ISS cannot fully account for the scatter in the 970508 data set (there is, moreover, inexplicable scatter at other frequencies).

uncertainty is put to the test.

We present deductions from the parameter comparisons in Chapter 5. In the following individual sections we present the details, both observational and analytic, of the events. These sections include some information not relevant to the cross-comparisons of the events (such as host fluxes). We also discuss some subtleties in the fits.

4.3 GRB 970508: The Details

GRB 970508 was detected by the *BeppoSAX GRBM* instrument and its X-ray afterglow found by the *BeppoSAX WFC* (Costa *et al.*, 1997a), allowing the discovery of its optical transient by ground-

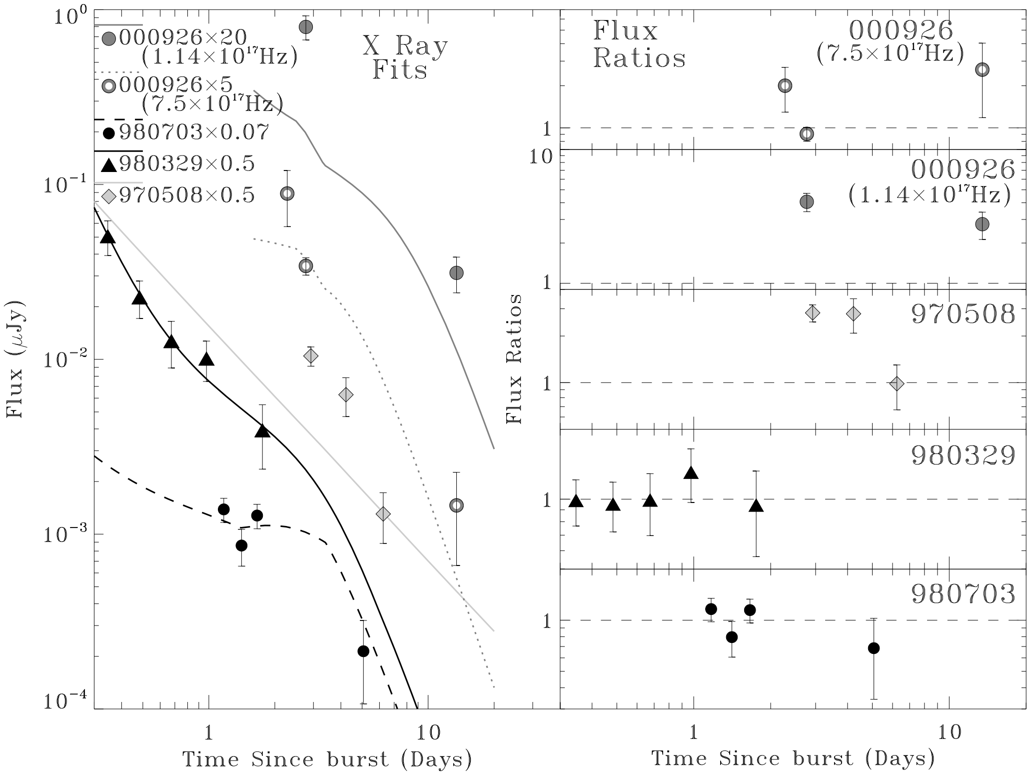

Figure 4.5: The X-ray data of the four events, with the best fits (see Table 4.2). The line style of each model is indicated above the symbol labels. The panels on the right show the ratios between the data and model, on a logarithmic scale. The GRB 000926 data is divided into a soft (solids) and a hard (open circles with dotted line) band. The broadband fit (with relative flux levels and decay rates) indicates an extra flux component in the X-ray, possibly inverse Compton upscatters, but our estimate of this component does not completely fit the data. Better sampled X-ray light curves, such as those expected from *Swift*, may clarify deficiencies in the X-ray flux model. Additionally, there is a minor IC flux component in the GRB 980329 model and IC dominates the early GRB 980703 X-ray model, providing the flat initial flux and slow decay to match the data.

based observers (Bond, 1997). This was the second afterglow discovery, and the first afterglow whose distance was determined. The initial lack of a distance measure to the first afterglow discovered (of GRB 970228) was due to a lack of prominent lines in its optical spectrum. However, (Metzger *et al.*, 1997) established the cosmological redshift of GRB 970508, z=0.835, from absorption lines in the spectrum of its optical afterglow. Djorgovski *et al.* (1999a) later determined the redshift of the 970228 event from spectral studies of its underlying host.

With a redshift demonstrating its cosmological nature, the 970508 event generated great interest, and a rich broadband afterglow data set developed from the efforts of many observers. The afterglow demonstrated a feature not describable by simple models–a sudden brightening in at least the the optical at approximately Day 1, followed by the usual power law decays at $t \geq 2$ days. Sparse X-ray coverage and scintillations at radio frequencies make it difficult to evaluate whether this behaviour was universal. Such afterglow events are unusual, as described in Chapter 2. No simple model can account for this brightening. It has been theorized to be due to a refreshing of the shock energy as slower material in the relativistic flow catches up to the decelerating forward shock (Panaitescu, Mészáros & Rees, 1998; Sari & Mészáros, 2000; Kumar & Piran, 2000). The shock may have encountered a jump in ambient density, increasing the concentration of emitters and the flux (Wang & Loeb, 2000; Dai & Lu, 2002; Nakar, Piran & Granot, 2003). There is also the possibility that the shock is a "patchy shell" where there are hot and cold spots in the shock and as the shell slows a hot spot may come into the observable area (Nakar, Piran & Granot, 2003). These models can provide a single rise that will not affect the emission substantially later. To avoid such complications we used only the data at $t \geq 2$ days, after the rise, for the modelling data set.

4.3.1 970508 at $t \geq 2$ Days: Data Set and Features

The data set includes the X-ray fluxes of Piro *et al.* (1998), converting to flux densities and frequency assuming the flux density is proportional to $\nu^{-1.1}$ over their quoted band. The optical/NIR data covers the $BVRI$ and K_s bands. The BVI data is from Sokolov *et al.* (1998) and Zharikov, Sokolov & Baryshev (1998), R is from the table of Garcia *et al.* (1998), and the K_s data is from Chary *et al.* (1998). The magnitudes are converted to flux densities with the information in Tokunaga (2000) for K_s and Bessell (1979) for $BVRI$. The Galactic coordinates of the burst are $(l, b) = (134.9°, 26.7°)$, calculated from the coordinates (Bond, 1997) with the NED Coordinate Calculator [2]. The optical data were corrected for the small Galactic extinction at that location, $E(B-V) = 0.050$ (Schlegel, Finkbeiner & Davis, 1998). For longer wavelengths there is Hanlon *et al.* (1999)'s mid-IR measurement by the Infrared Space Observatory (ISO) at 12 μm. The 86 & 232 GHz submillimeter measurements of Bremer *et al.* (1998) are used. The radio data set includes Taylor *et al.* (1997)'s 15 GHz data and Frail, Waxman & Kulkarni (2000)'s 1.43, 4.86, and 8.46 GHz measurements.

---

[2] http://nedwww.ipac.caltech.edu/forms/calculator.html

This data set shows the classic power law decays (rise and decay in the radio). It shows no sudden overall changes, and no steep declines (a steady overall decline in the optical and general rise and fall in the radio through a year post-burst); it is not expected to fit with collimated ejecta. Furthermore, the data shows two additional features.

First, there is a great deal of scatter about these general trends. There do not appear to be correlated "bumps and wiggles" in time or across wavelength bands. For example, there is a bright deviation in the R band at Day 5 (see Figure 4.3) which does not appear in other optical bands. Although their sampling is sparser, B and V data were taken near-contemporaneously with the R deviation yet do not show a similar flux increase (Figure 4.6). The X-ray data includes only three points and it is not clear if the sudden decline in the third epoch is also part of this scatter. The radio deviations may be due to interstellar scintillation, although this cannot explain the optical data's scatter. To some extent the level of variation in the radio declines with time. This decrease in variability is expected of ISS as the source size increases (see the scalings for extended sources in Narayan, 1992). If this is the source of radio flux variation, the level of ISS may be under-predicted by the model used to account for it, described in Chapter 3. Figure 4.4 shows that several points deviate significantly from the envelope describing the extra uncertainty estimate in the model due to ISS. For the broadband data, it is not clear how much variation may be due to real physical effects (such as clumpiness in the circumburst medium), and how much could be attributed to cross-calibration uncertainties (this was the first large afterglow data set, and combined optical data from a multitude of sources).

Second, there may be a decline in the peak flux level. Frail, Waxman & Kulkarni (2000) report that the peak flux declines from $\sim 650\,\mu$Jy at the high (8.46 and 15 GHz) radio frequencies to $\sim 300\,\mu$Jy at 1.43 GHz (with uncertainties $\sim 110\,\mu$Jy), and that it may have been 1620 μJy at 86 GHz from Bremer *et al.* (1998)'s data, implying $F_{\nu,max} \propto \nu_{max}^{0.4}$. Figure 4.7 shows the data for 1.43, 4.86, and 8.46 GHz. As seen from the expected behaviour of the peak flux (Equation 3.4), this would not be compatible with pre-jet expansion into an ISM-like medium. Such a "peak flux cascade" could indicate post-jet evolution ($F_{\nu}^{max} \propto \nu_{m}^{0.5}$, Equation 3.3) or a Wind-like density profile

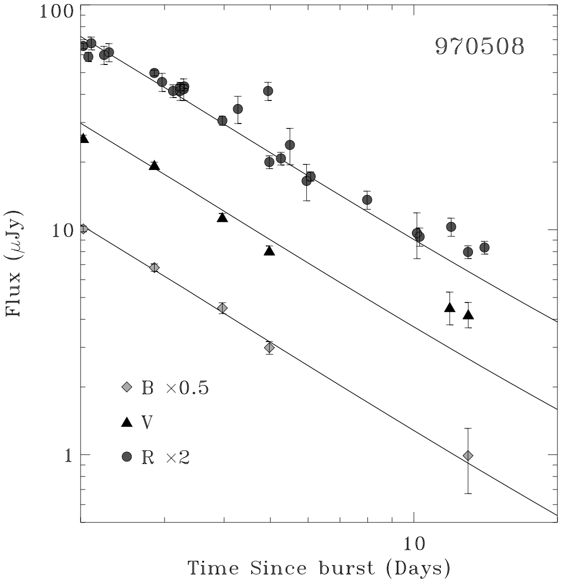

Figure 4.6: 970508 early (2–20 day) BVR light curves, plotted with the best model (Table 4.2). There is unexplained "scatter" in the data. Some deviations may be correlated across wavelength bands (see B and R at two weeks). Others are not, such as the high R flux at 5 days which is not seen in contemporaneous B and V data, and is contradicted by other near-simultaneous R observations. These may be due to errors or underestimated uncertainty in the calibration (and cross-calibration amongst observers).

($F_\nu^{max} \propto \nu_m^{1/3}$, Equation 3.5). We find the evidence for either scenario to be weak. The data at 86 GHz is of quite poor signal-to-noise, near the detection limit, and does not strongly constrain the peak level at that frequency. The lower frequencies have significant flux variations as described above; with that uncertainty, it is difficult to establish that the peak flux declines from 15 to 4.9 GHz. The peak at 1.43 GHz appears significantly lower but as this is at the lowest frequency at the latest time it may be due to a simpler cause. It may be self-absorbed, or the peak may be passing after the non-relativistic transition (at which point the peak will drop in time).

4.3.2 970508 Fits

We fit this event to the model as presented in Chapter 3. As explained there, modelled host flux components may be required depending upon the event. We found no need to include a radio host flux, nor a submillimeter host (the data is not constraining). We fit optical $BVRI$ band host components, as some flattening begins near the end of the data set ~ one year post-burst. The host is not faint, as seen from the set of optical host flux asymptotes in Figure 4.3; the optical afterglow

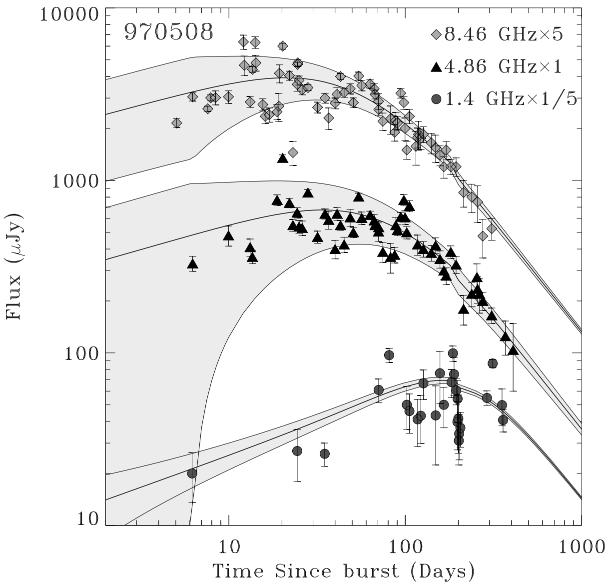

Figure 4.7: 970508 radio light curves, plotted with the best model (Table 4.2). The grey shaded regions represent the estimated flux uncertainties in the model due to interstellar scintillation. The two higher-frequency bands peak at nearly the same flux level in the model, ≈ 700 μJy, although the precise peaks in the data are difficult to determine due to the "scatter" in flux values. The 1.4 GHz data peaks at a lower flux, ≈ 400 μJy. In the model this is accounted for chiefly by the optical thickness of the spectrum near 1.4 GHz. We do not see strong evidence of a continuous cascade in peak flux values.

was quite bright and dominated the received flux for longer than is typical.

There is no strong curvature in the optical portion of the spectrum, as shown in Figure 4.8. Only a small host extinction is necessary in the fit, and the LMC extinction law suffices to describe it.

To partially accommodate the scatter seen, we added an extra 5% of the measured fluxes to the uncertainties across the board as a cross-calibration measure. This was driven by the optical, where the data set was taken from multiple observers (so instruments and calibration methods). This does not account for the amount of scatter seen, but for a reasonable level of systematic uncertainty amongst photometric systems.

With four host components, the fit has 11 parameters and 268 data points. We used various initial parameter sets for fit attempts, including some based upon the inversion of a snapshot spectrum's observables to physical parameters, taken from Wijers & Galama (1999)'s Day 12.1 spectrum. We attempted to fit models with both Wind-like and ISM-like density profiles; the ISM-like fit was slightly better. In both cases the fit statistic is $-ln(P)$ (§3.5), which avoids biasing with the scin-

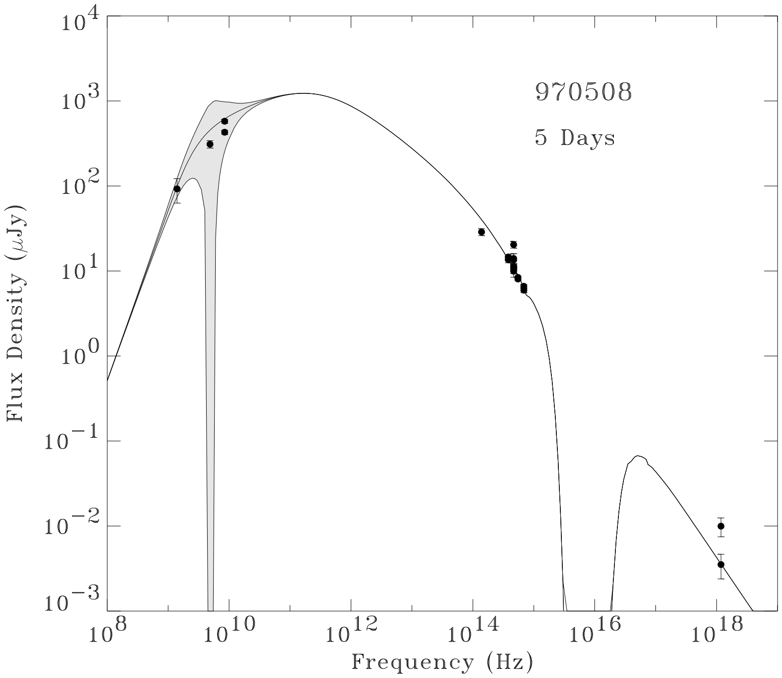

Figure 4.8: 970508 spectrum, with data from 3.75–6.25 days post-burst, scaled to five days post-burst, and plotted on the model's Day 5 spectrum. The data are de-reddened of Galactic effects. The model is the best fit, an ISM-like case presented in Table 4.2. The synchrotron spectrum has a negligible estimated inverse Compton flux component. The grey shaded region represents the estimated flux uncertainty in the model spectrum at this time, due to interstellar scintillation. Some of the data's "scatter" at optical and X-ray frequencies is visible. The average trend in the optical portion is well described by a power law; little extinction is required at the host to explain spectral curvature.

tillation envelopes. We found no results under this scheme where χ^2 is much better than the χ^2 of the fit with minimum $-ln(P)$. Given the poor χ^2/DOF (596/257 versus 661/257), we cannot reject the Wind-like fit in favour of the ISM-like case.

While there are differences by factors of up to a few between the results for the two density profiles, they do not represent two solutions from vastly different parts of parameter space. The ISM-like fit has an isotropic-equivalent energy $E_{iso} \approx 4 \times 10^{52}$ ergs, and the Wind-like fit has $E_{iso} \approx 3 \times 10^{52}$ ergs. The ISM-like fit is nearly isotropic ($\theta = 0.84$ rad), and the Wind-like fit is isotropic. The microphysical values are of the same order: $p = 2.1$, $\epsilon_e = 0.3$, and $\epsilon_B = 25\%$ for the ISM-like fit and $p = 2.4$, $\epsilon_e = 0.1$, and $\epsilon_B = 5\%$ for the Wind-like fit. Both have low extinction in the host frame (0.14 and 0.07 $A(V)$ magnitudes, respectively) and $BVRI$ host flux levels ($\approx$ 0.08, 0.2, 0.2, and 0.7 μJy respectively). The density in the ISM-like case is $0.2\,\mathrm{cm}^{-3}$ while the density scale for the Wind-like case is $0.6\,A_*$. For that scale, over a radius range of $10^{17} - -10^{18}$ cm, the density varies from 20 to 0.2 cm^{-3}. Given that the fits are not fundamentally different and neither has clearly unacceptable physical parameters, the ISM-like result is selected as the best one due to its slightly better fit. Its results are in Table 4.2, save for the host fluxes.

This was clearly not a good fit that covers all the aspects (scatter) in the data. For a small degree of scatter, an even greater cross-calibration uncertainty could be considered to bring $\chi^2 \approx$ DOF. This would enable a $\delta\chi^2$ test for the statistical uncertainties in the fit parameters. The increased uncertainties would be too extreme for this to be reasonable (for $\chi^2 = 2.5\,\mathrm{DOF}$, each uncertainty would have to be increased by a factor of about 1.6). Therefore we employed Monte Carlo bootstraps (Efron, 1982) to determine the statistical error bars.

The poor fit raises the concern that one odd deviation in the radio or optical could count as much in the fit statistic as all of the X-ray data. As described in §3.5, an extra weighting factor is permitted point by point in the fit. We employed these weights to give an equal leverage to each of three wavelength regions: the radio & submillimeter, the optical & IR, and the X-ray. At the same time, a more robust fit statistic (less dependent upon outliers, with $((\mathrm{flux} - \mathrm{fit})/\sigma)^N$ with $N < 2$) might also reduce this bias. Fits were performed to the ISM-like density profile with the wavelength-weighted χ^2 and Least Absolute Deviation ($N = 1$). The results did not substantially change the goodness of the fit (in terms of matching the data's trends). Some of the best results had nearly the same parameters as the best fit without the extra weighting. They are not considered an improvement.

We find our best fit (see Figure 4.7) does not require a "peak flux cascade", a strong decline in peak flux level as the peak passes to lower frequencies. As discussed above, this could be produced by a Wind-like density profile, or post-jet evolution. Our fit has a non-negligible ϵ_e that requires some radiative corrections to the energy, gradually decreasing the peak.

To quantify this gradual decline, we examine the radiative losses in the model. Fast cooling would have ended rapidly in the shock model we fit, at 0.08 days post-burst. We note that discussing the energy at $t <$ two days may have no physical validity; the brightening event at that time is likely to have changed the average energy in the visible shock if it is due to a refreshed shock or a patchy shell, as indicated above. If there had been no brightening event (or if the event did not change the energy in the shock), the isotropic-equivalent energy at the end of fast cooling would have been $\approx 4 \times 10^{52}$ ergs. We estimate that after the brightening, by 2.5 days post-burst, the energy was 1.3×10^{52} ergs, and by 450 days post-burst, at the end of observations, it was 0.4×10^{52} ergs. The energy would have dropped by a factor of three over the observations, and so the peak as well. In addition, a self-absorption break initially at a few GHz suppresses the flux at lower frequencies. This model matches the requirement for a lower peak flux at 1.4 GHz than at higher radio frequencies.

Finally, we compared the kinetic energy in the shock model with the energy determined from the γ-ray fluence of the prompt emission. Again, the modelled shock energy may have no relation to the shock energy during the GRB proper, but this is of some interest in comparison to the other events. The isotropic-equivalent γ-ray energy is approximately 5.5×10^{51} ergs (the k-corrected value to 20–2000 keV in the rest-frame calculated by Bloom, Frail & Sari, 2001). We extrapolate our isotropic-equivalent energy for the shock back to 100 seconds (immediately post-burst). The energy would have been 1.7×10^{53} ergs. In this model, the γ-ray production efficiency would be $\approx 3\%$.

4.4 GRB 980329: The Details

GRB 980329 was well-localized in the gamma-rays, and its position quickly refined as a result of the X-ray detection by In 't Zand *et al.* (1998). However, initial searches for an optical afterglow were unsuccessful until variable emission was identified at radio wavelengths (Taylor *et al.*, 1998). Subsequent observations of the radio position uncovered a faint optical counterpart (Djorgovski *et al.*, 1998a), as well as a relatively bright near-infrared (NIR) transient (Klose, 1998). Because of the delay in the identification of the optical afterglow, the early optical monitoring was somewhat sparse. In spite of the eventual detection of optical and NIR counterparts, no redshift has been determined, due to the faintness of the host emission and its lack of prominent emission lines. We thoroughly studied this event. The following rather detailed discussion is largely from Yost *et al.* (2002) and is divided into sections concerning the data, the best model fits, alternative models, and the fitted host.

4.4.1 980329 Data

The data set for this event includes significant radio, submillimeter, optical/NIR, and X-ray observations. The radio and submillimeter data includes observations at 1.43, 4.86, 8.46, and 90 GHz taken from the literature (Taylor *et al.*, 1998), as well as 1.43, 4.86, 8.46, 220, 350, and 650 GHz data presented by the Caltech GRB group (Yost *et al.*, 2002). The optical also includes observations garnered from the literature in the RIJ and K bands (Palazzi *et al.*, 1998; Gorosabel *et al.*, 1999; Reichart *et al.*, 1999), and $RIHK$ data presented by the Caltech GRB group (Yost *et al.*, 2002). In addition, we include all published data in the X-ray (In 't Zand *et al.*, 1998).

The Galactic coordinates of the event are $(l, b) = (178.1^\circ, 18.7^\circ)$ (equatorial coordinates from Taylor, Frail & Kulkarni, 1998, and converted by NED[3]); thus the Galactic extinction to de-redden along the line of sight is only $E(B-V) = 0.073$, 0.19 magnitudes at R band (Schlegel, Finkbeiner & Davis, 1998). The subsequent conversion to flux densities at the bands' central frequencies used the factors in Bessell (1979) for the optical and Bessell & Brett (1988) for the near-IR bands. We converted the X-ray flux measurements (in the given energy band) to flux densities at a characteristic frequency using the X-ray spectrum ($N(E) \propto E^{-\Gamma}$) and photon index $\Gamma = 2.4$ (In 't Zand *et al.*, 1998). We added 5% uncertainties in quadrature to all the measured fluxes to account for any cross-calibration uncertainty.

There are some unusual features in the data. There is an apparent submillimeter excess, very red $R-I$ afterglow colours, and an observed decline of the peak flux density F_m with time (or equivalently with decreasing frequency ν_m, since ν_m decreases with time). Smith *et al.* (1999) see evidence for a submillimeter host component in the data. Fruchter (1999) attempted to explain the very red colour as evidence that the GRB occurred at high redshift, $z \sim 5$, from the Lyα absorption by hydrogen in the intergalactic medium; Lamb, Castander & Reichart (1999) found the colour could be explained by the far-ultraviolet steepening of the extinction curve at $3 \lesssim z \lesssim 4$ or the 2175

---

[3] http://nedwww.ipac.caltech.edu/forms/calculator.html

Å dust resonance in the extinction law if $z \approx 2$.

The observed decrease in peak flux warrants further explanation, since it is an effect that can result from only a finite number of physical causes. The "peak flux cascade" can be readily seen in Figs. 4.11 and 4.12, where the peak flux density is 2.5 mJy at 350 GHz but declines to 1.5 mJy at 90 GHz and further falls to 0.35, 0.2 and <0.1 mJy at 8.46 GHz, 4.86 GHz, and 1.43 GHz, respectively. A fit to flux maxima between 4.86 GHz and 350 GHz gives a power law $F_m(\nu) \propto \nu^N$, $N = 0.59 \pm 0.07$. A similar behaviour was hinted at by the afterglow of GRB 970508 (Frail, Waxman & Kulkarni, 2000, but see the discussion in §4.3). Within the context of the standard fireball model there are three ways to produce this behaviour. First, if the flux evolution is observed after collimation of the ejecta becomes evident in the lightcurve decay (*i.e.*, post-jet), then $F_m \propto \nu_m^{1/2}$ (Sari, Piran & Halpern, 1999). For our best model, this is what produces the observed peak flux cascade. Alternatively, a Wind-like density profile $n \propto r^{-2}$ will give $F_m \propto \nu_m^{1/3}$ (Chevalier & Li, 1999). These can be deduced from the basic behaviour discussed in Chapter 3, Equations 3.3 and 3.5. Finally, radiative losses can produce a peak flux cascade. However, unless these are severe (namely, most of the shock energy in electrons), the effect is quite weak. For example, for $\epsilon_e \simeq 0.1$, $F_m \propto \nu_m^{0.08}$, while for $\epsilon_e \simeq 1$, $F_m \propto \nu_m^{0.37}$ (Cohen, Piran & Sari, 1998).

In the following section, we present a self-consistent solution derived from reasonable values for the blast-wave energy $E_{\rm iso}(t_{\nu_c=\nu_m})$, the opening angle θ_{jet}, the ambient density n and the microphysical parameters of the shock (p, ϵ_e, ϵ_B). While it is not a unique interpretation of the data, it describes all of it well without invoking a very high redshift or other additional components.

4.4.2 980329 Fits

The model which best describes this broadband data set is a collimated outflow expanding into an ISM-like medium. The best model parameters, derived from least-squares maximizing the fit probability, are given in Table 4.3 and the fits are shown in Figures 4.3, 4.4, and 4.5, summarizing all events treated in this chapter as well as in Figures 4.9–4.13 below, specific to GRB 980329. The χ^2 for the fit is 116.4 for 92 degrees of freedom. By the χ^2 test, there is a 4% probability that the

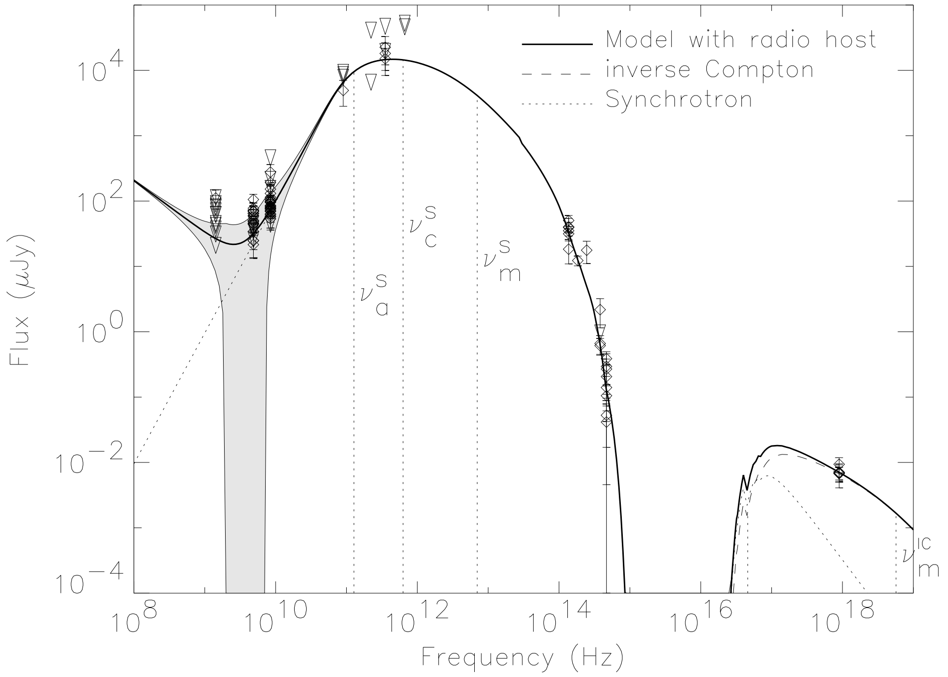

Figure 4.9: All of the 980329 data, scaled to Day 2 post-burst, and plotted on the model's Day 2 spectrum. The spectrum's inverse Compton and synchrotron flux components are decomposed from the total. The grey shaded region represents the estimated flux uncertainty in the model of the observed spectrum at this time due to interstellar scintillation. The high self-absorption frequency and predominance of the Comptonized flux at X-ray frequencies can be clearly seen.

data is fully described by the model.

Although we derived fits for three representative redshifts ($z = 1, 2, 3$), the results of which are all shown in Table 4.3, all discussion and comparisons pertain to the central, $z = 2$, solution. The choice of representative redshifts was made based upon the range of likely z for this burst. Very high redshifts ($z \gtrsim 5$) are not considered as they are not compatible with the underlying host's colours, as detailed in §4.4.3. A redshift $z < 1$ is considered implausible due to the lack of lines expected to be detected (if $z < 1$) in several spectra taken of the host. The host is visible at optical wavelengths, and thus not completely obscured, so it is quite unlikely that the prominent star-formation-related oxygen line [OII]λ3727 or the Hα line would not have been observable if the host is a faint galaxy at $z < 1$. Many of the basic conclusions do not depend on the redshift, or can be easily scaled given the information below. In §4.4.4 we discuss some of the limitations of our best fit, as well as some alternative models which also fit the data, but only with unphysical parameters.

In the best model for $z = 2$, the isotropic-equivalent fireball energy at the time when the fireball evolution becomes nearly adiabatic ($E_{\rm iso}(t_{\nu_c=\nu_m})$) is approximately 10^{54} ergs. That energy is a lower limit on the true initial energy in the blast-wave, as radiative losses will have occurred from the rise of the blast-wave to this time, 6.1 days, when fast cooling ends. For the best model, radiative losses are important, but not extreme even at early times, since the fraction of energy in radiating electrons is not dominant (ϵ_e=12%). Using our computational routines employed in the fit model, we estimate that from the time the GRB ends ($\sim$ 10–100s post-trigger), to when the blast-wave is nearly adiabatic, the energy drops by a factor of five. If the calculation begins when the first afterglow data were measured, ($t = 0.25$ d for the first data point to $t_{\nu_{\rm c}=\nu_{\rm m}}$), the energy drops by a factor of 1.6. From the time $t = t_{\nu_{\rm c}=\nu_{\rm m}}$ until late times the energy drops by only 15% .

The energy in the fireball derived from the model significantly exceeds the emitted gamma-ray energy, *i.e.,* $E_{\rm iso}(t_{\nu_c=\nu_m}) > E_{\rm iso}(\gamma)$. This is the case for the majority of GRB afterglows with energies derived from model fits (see, e.g., Panaitescu & Kumar, 2001a). For GRB 980329 the isotropic-equivalent γ-ray energy is approximately $5.1{\times}10^{53}$ ergs (the *k*-corrected value, that is, transformed to a 20–2000 keV comoving band by accounting for the GRB spectrum, as calculated by Bloom, Frail & Sari, 2001, but for this assumed redshift). The fireball energy throughout the afterglow phase is $\approx 10^{54}$ ergs (isotropic); the initial fireball energy will be even larger if radiative losses are taken into account. We extrapolate our isotropic-equivalent energy for the shock back to 100 seconds (immediately post-burst); it would have been $4.4{\times}10^{54}$ ergs. The γ-ray production efficiency would be $\approx$10%. This value is reasonable in the fireball model. It is likely that the energy remaining in the shock during the afterglow exceeds that of the prompt gamma-ray emission of the GRB event itself. This energy partition to the afterglow occurs when the radiative efficiency is less than 50% during the GRB. The radiative efficiency of internal shocks driving the prompt GRB are expected to be $\sim$ 10%, not $\gg$ 50%, leaving most of the initial shock energy in the fireball (Beloborodov, 2000; Spada, Panaitescu & Mészáros, 2000; Guetta, Spada & Waxman, 2001). Even a radiative efficiency of approximately 60% is considered "ultra-efficient" (see Kobayashi & Sari, 2001).

The large energies inferred for both the shock, $E_{\rm iso}(t_{\nu_c=\nu_m})$, and the emitted gamma-ray radiation, $E_{\rm iso}(\gamma)$, derived assuming isotropy are greatly reduced in this model by the relatively large

Table 4.3: Fit parameters for assumed $z = 1, 2, 3$

Parameter	z=1	z=2	z=3
χ^2 for 105 data pts	113.1	116.4	119.4
$t_{\rm jet}$ (days)	0.21	0.12	0.29
$t_{\rm nonrel.}$ (days)	35	70	96
$t_{\nu_c=\nu_m}$ (days)	2.4	6.1	10.0
$E_{\rm iso}(t_{\nu_c=\nu_m})(10^{52}$ ergs) [a]	15	126	107
$n(cm^{-3})$	20	20	29
p	2.55	2.88	3.06
ϵ_e (fraction of E)	0.08	0.12	0.14
ϵ_B (fraction of E)	0.27	0.17	0.08
$\theta_{jet}(rad)$	0.081	0.036	0.049
host A(V)	2.8	1.9	1.4
host R (μJy)	0.13	0.13	0.13
host I (μJy)	0.090	0.091	0.090
host H (μJy)	0.20	0.20	0.20
host K (μJy)	0.68	0.69	0.70
host 1.4 GHz (μJy)	19	25	26
$E_{\rm iso}(\gamma)$ (10^{53} ergs) [b]	1.5±0.2	5.1±0.6	9.5±1.1
$E(\gamma)$ (10^{50} ergs) [c]	5.0±0.6	3.3±0.4	11±1

---

[a] Isotropic equivalent blast-wave energy (not corrected for collimation)

[b] Isotropic-equivalent energy emitted in the gamma-rays by the GRB, if it occurred at this redshift, calculated by the method of Bloom et al. (2001)

[c] The isotropic-equivalent energies given above, corrected assuming the jet angles (without uncertainty) presented above

degree of collimation (jet half-opening angle of $\theta_{jet} \sim 2°$). A similar degree of collimation has been inferred previously in GRB afterglows: GRB 990510 has $\theta_{jet} = 3°$ (Harrison *et al.*, 1999) and GRB 000911 has $\theta_{jet} = 2°$ (Price *et al.*, 2002a). For a two-sided jet this implies a total energy in the fireball shock of $E_{iso}\Delta\Omega/4\pi = E_{iso}(1 - \cos(\theta)) = 8.3 \times 10^{50}$ ergs, similar to the energy released in supernovae. Likewise, for $z = 2$ the geometry-corrected gamma-ray energy is reduced to 3.3×10^{50} ergs, a value that is in good agreement with the mean of 5×10^{50} ergs derived from a larger sample (Frail *et al.*, 2001). We note the total energy is similar (5.0×10^{50}) for $z = 1$, and a factor of about three higher for $z = 3$.

The ratio of the energy fraction in magnetic field, ϵ_B =17%, to that in the electrons, ϵ_e=12%, determines the relative importance of inverse Compton (IC) scattering, as discussed in §3.4. In our best model for GRB 980329, this ratio is of order unity, so IC does not dominate the electron cooling, but it is a non-negligible effect. Flux from Compton scattering can in fact be seen peaking in the X-rays in the X-ray light curve plateau of Figure 4.5, indicating the dominance of IC flux evident in Figure 4.9's spectrum. This visible IC flux is largely a result of the steep electron spectral index. For an electron energy spectral index of 2, with equal energies in each logarithmic frequency interval (the infinite-energy limit), the IC luminosity would be lower than the synchrotron luminosity at all frequencies, and no IC peak would be observable in the spectrum. The index of $p = 2.9$ derived for the best model puts less energy in each successive decade above the peak frequency. With a significant circumburst electron density providing a non-negligible opacity to Compton scattering, the peak of the IC flux density, above the synchrotron peak, dominates the total flux near the X-rays.

Finally, the circumburst medium density derived from the model, $n = 20$ cm^{-3}, is comparable to those inferred from other bursts (Panaitescu & Kumar, 2001a). This relatively high density, in reference to an average galactic ISM, is expected from the measured value of the self-absorption break ν_a (Granot, Piran & Sari, 1999b), which is shown in Figure 4.9. The frequency ν_a depends upon other fundamental parameters besides the ambient density ($\nu_a \propto n^{3/5}\epsilon_e^{-1}\epsilon_B^{1/5}E^{1/5}$, Equation 3.4), and in this particular case the high ν_a results from the relatively high density, combined with a moderate electron energy fraction. Models with low circumburst densities (*i.e.*, $n \ll 10$ cm^{-3}) cannot be fit to the data by adjusting the energy and electron fraction. Highly radiative models, with large electron energy fractions, can provide reasonable fits to the data, but the densities (depending on the redshift of the fit) vary from approximately the same as to an order of magnitude greater than those for the best model (see §4.4.4).

4.4.3 980329 Host Properties Inferred from the Dataset and Fit

We infer the presence of measurable flux from the GRB host galaxy in the optical from the late-time flattening of the data set's light curves (Fig. 4.13). In Fig. 4.10, we plot the spectral energy distribution of the afterglow at 0.7 days after the burst along with the late-time measurements from the data set, assumed to be due to the host galaxy. We corrected all points for extinction in our Galaxy. Palazzi *et al.* (1998) first noted the steep spectral slope between the R and I bands seen in the early time afterglow. As mentioned above, Fruchter (1999) suggested that this "dropout" of the R band could be produced by absorption from the Lyα forest if the redshift of this burst was

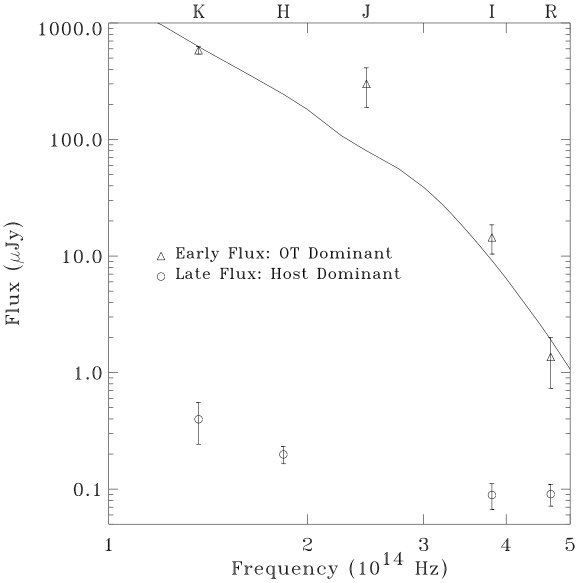

Figure 4.10: Comparison of afterglow and underlying host optical flux densities. The data are corrected for Galactic (but not host) extinction. The first available data points (open triangles) in R, I, J, and K bands (at 0.73, 0.71, 8.1, and 4.2 days post-burst, respectively) were each scaled to 0.7 days using our best afterglow model (overplotted). The afterglow (the Optical Transient, or OT) flux dominates these points and the spectral steepness from I to R is clearly seen. (Note that the J band point, extrapolated from a time when the host flux was beginning to become important, is a less reliable afterglow flux indicator.) The late time measurements (open circles) at R, I, H, and K bands are also plotted to show the host spectrum. The host spectrum does not show the steep spectral slope between the I and R bands, as expected if GRB 980329 was at $z \gtrsim 5$.

greater than five. This steep slope, however, is not reflected in the host spectrum. The afterglow at 0.7 days after the burst is significantly redder ($R-I$=2.7±0.4 magnitudes) than the host galaxy ($R-I$=0.2±0.3 magnitudes) itself (note that the quoted $R-I$ above are corrected for Galactic extinction). From the absence of a strong $R-I$ break in the host spectrum, we can rule out a redshift of $z \gtrsim 5$ for GRB 980329.

A result that emerges from the modelling is the presence of significant dust extinction in the host galaxy. Early attempts to model the optical data for this burst (Palazzi *et al.*, 1998; Lamb, Castander & Reichart, 1999) also found that the spectrum was substantially reddened by dust. Our fitted host $A_{\rm V}$ corresponds to hydrogen column density of $N_H \simeq 2 \times 10^{21}$ cm^{-2}, assuming a gas-to-dust ratio similar to that of the Milky Way (Predehl & Schmitt, 1995; Reichart, 2001). In 't Zand *et al.* (1998) used the X-ray spectrum of the afterglow to derive a column density $N_H = 1.0 \pm 0.4 \times 10^{22}$ cm^{-2}, with a 99% confidence range of 1.3×10^{21}–1.5×10^{22} cm^{-2}, after subtracting a Galactic contribution of approximately 0.8×10^{21} cm^{-2} (Dickey & Lockman, 1990). To translate this measured column into the rest-frame of the host galaxy requires multiplying by a factor $(1+z)^{8/3}$. For a redshift of 2, this exceeds the value derived from optical extinction. Such discrepancies have been noted before (Vreeswijk *et al.*, 1999; Galama & Wijers, 2001), and are taken as evidence of significant dust destruction in the circumburst medium out to a radius of order 10–20 pc (Waxman & Draine, 2000; Fruchter, Krolik & Rhoads, 2001; Reichart, 2001). In the case of GRB 980329, however, the precise redshift is not known, and the uncertainties in the dust extinction law make it difficult to claim evidence for dust destruction.

Finally, there is a suggestion of a 1.43 GHz radio host in the data, with the model requiring a flat, positive component on average (see Figure 4.11). Although the addition of this component improves the fit, the significance of a nonzero radio host parameter is only $3\,\sigma$. If real, a radio host at $\simeq 25$ μJy would be about 1/3 the host flux density found for GRB 980703 (Berger, Kulkarni & Frail, 2001). We note that the submillimeter data are in good agreement with the afterglow model (see Fig.4.12), and we do not require any host contribution in this band.

4.4.4 980329 Fit Limitations and Alternate Models

The best fit model, described in §4.4.2 is a self-consistent solution that derives reasonable parameter values. A collimated outflow expanding into a constant density medium, with high host extinction, describes *all* the data well, addressing the afterglow's puzzling features (red afterglow colour, submillimeter flux level, and peak flux decline).

The other models we derived that fit the primary characteristics of the data all required unusual physical assumptions. For example, we found a solution with extreme radiative corrections (100% of the shock energy going into electrons) that could reproduce the observed peak flux cascade. Formally, this model fits the data better than the "best model" presented in the previous section; however, it reaches the unphysical edge of parameter space, and with extreme radiative losses our energy loss corrections to the adiabatic treatment breaks down and cannot be fully trusted. The highly radiative model is isotropic, and for $z=2$, has the following parameters: $E_{\rm iso}(t_{\nu_c=\nu_m}) \simeq 2\times10^{52}$ ergs,

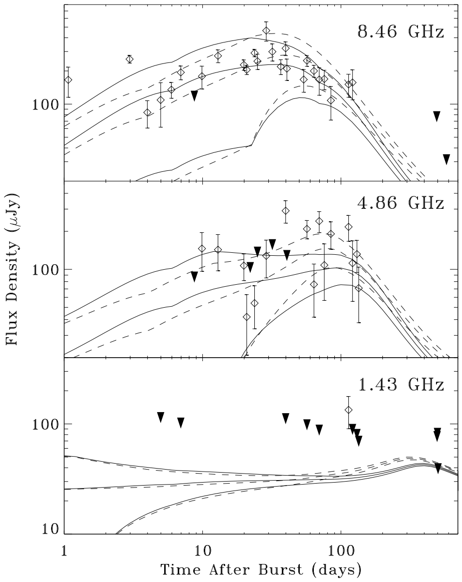

Figure 4.11: Radio light curves of the GRB 980329 afterglow. Both the best model and the extreme radiative solution, described in §4.4.4, are plotted. The light curves of the "best" model (the best physical model; see §4.4.2 and 4.4.4 for details) are solid; the radiative solution's are dashed. The model light curves are plotted with their calculated $1\,\sigma$ scintillation envelopes. Data that are not at least detected at the $2\,\sigma$ level are presented as $2\,\sigma$ upper limits (max(flux density, 0) + 2 × rms noise; black triangles). The 1.43 GHz data is only significant as a whole. Note that the 8.46 GHz data at $\leq$ three days, not included in the fits, is significantly in excess of both models.

$n \simeq 20\,\mathrm{cm}^{-3}$, $p \simeq 2.02$, $\epsilon_B \simeq 0.17$, $\epsilon_e \to 1$, A(V) $\simeq 1.1$ and a centimeter host of $\simeq 17\,\mu$Jy at 1.43 GHz. In addition to the unphysical assumption about the electron energy partition, this model also has an electron spectral index approaching two, and hence a diverging total energy. This radiative model only accounts for $\approx 1/2$ of the 350 GHz flux, suggesting an underlying submillimeter host of $\simeq 0.7$ mJy (this component improves the fit at approximately a $3\,\sigma$ level). This submillimeter host flux level is just below the sensitivity limit of current instruments and would likely not be detectable at late times, after the afterglow declines, if it indeed exists. We consider the collimated solution presented above to be the best model as it is the best fit of the models with realistic parameters. This best model reproduces the flux cascade with a relatively narrow collimation angle (early jet break). We note that the $p = 2.88$ we derive for the best $z = 2$ model is somewhat larger than found for other afterglows, which generally fall in the range $p = 2.2 - 2.4$. It is, however, physically reasonable, and we regard all the parameters associated with the best model as acceptable. The highly radiative solution is plotted along with the best model in the light curves presented of this

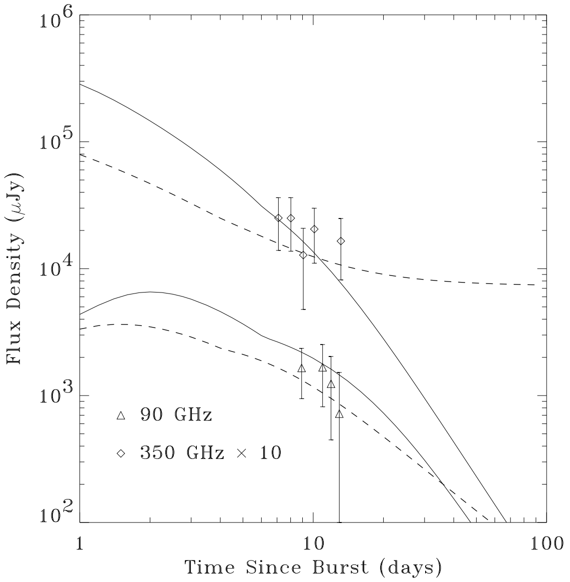

Figure 4.12: Millimeter and submillimeter light curves of the GRB 980329 afterglow; the 350 GHz data and model are multiplied by ten for clarity. The "best" model (the best physical model; see §4.4.2 and 4.4.4 for details) is shown with solid light curves; the radiative solution (§4.4.4) with dashed lines. The "best" model fits the re-analyzed data without the need to include a submillimeter host component. The radiative solution is plotted with the submillimeter host component, required to account for $\sim 1/2$ of the 350 GHz flux.

section (focusing upon 980329), Figures 4.11, 4.12, and 4.13. The fit is visibly somewhat better, but at the cost of unphysical assumptions concerning the underlying parameters of the fireball.

The most serious limitation to modelling the afterglow of GRB 980329 is the lack of a good redshift estimate. Even a fairly comprehensive data set such as this cannot constrain fundamental parameters without knowing the distance. This is because the synchrotron emission can be reproduced at different z simply by rescaling the physical parameters by appropriate powers of $(1+z)$. Only "second order" effects such as host extinction, the IC component and radiative corrections do not directly re-scale with $(1+z)$. In principle, we could include z as a free parameter in the model, and fit for the best value. In practice, however, the combination of the sparseness of the real data set, and the uncertainties in the model prevents any unique redshift determination. This is evident from Table 4.3, where we show a good fit with reasonable physical parameters for all three redshifts.

The absence of a strong break in the host galaxy spectral colours (Fig. 4.10) allowed us to place our $z \sim 5$ upper limit on the host redshift. Spectral energy distribution (SED) fittings to host colours can place stronger constraints; Castander & Lamb (1999) did so for the 970228 event. The

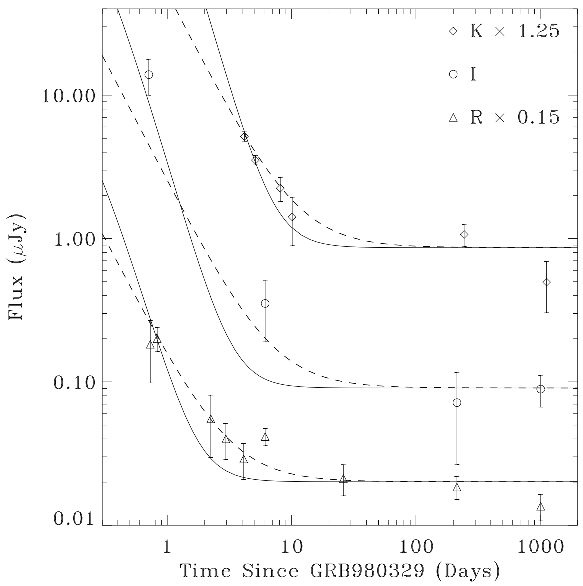

Figure 4.13: Optical light curves of the GRB 980329 afterglow at R, I, and K bands. The "best" model (the best model with physical parameters) is shown with solid light curves; the extreme radiative solution (§4.4.4) with dashed ones. The data are corrected for Galactic (but not host) extinction. The late-time host fluxes can be clearly seen.

GRB 980329 host has a promising feature in this regard, a factor of $\sim$ four decline from K-band to I-band; it may correspond to a Balmer break (caused by hydrogen opacity in the host frame). Recently, Jaunsen *et al.* (2003) performed late-time host observations and calculated a photometric redshift estimate $z \sim 3.5$ from all available optical-NIR host data, excluding $z < 1.2$ and $z > 4.2$ at the 95% confidence level.

The absence of a redshift is responsible in part for the relatively large and uncertain estimate of the electron index p in our best model. The post-jet evolution of the optical light curves is determined by p (Sari, Piran & Halpern, 1999). Unfortunately, this data is sparsely sampled at early times (Fig. 4.13), prior to when the host galaxy dominates the light. Likewise, the index p determines the shape of the synchrotron spectrum, and should therefore be derivable from the measurements. At optical wavelengths, however, there is a degeneracy between p and the dust extinction law—the latter of which can depend sensitively on z. We noted the strong curvature even in the coarse optical spectrum (see Figure 4.10) and expected a steep extinction law would be required to account for it. Lacking any knowledge about the extinction properties of dust in high redshift galaxies, we adopted the steepest locally-known law, that of the SMC bar. Neither the X-ray spectral slope, nor the X-ray to optical flux ratio, can break the p-extinction degeneracy, since the contribution from inverse Compton scattering alters the X-ray flux normalization as well as the spectrum.

Finally, we note that both our best solution and the highly radiative solution fail to predict the early radio emission at 8.46 GHz ($t < 3$ d). This level of fluctuation is too great to be accounted for by the estimated interstellar scintillation effects. Prompt, short-lived radio emission in excess of the normal afterglow component has been detected toward other GRBs (Kulkarni *et al.*, 1999b; Frail *et al.*, 2000; Harrison *et al.*, 2001). This is usually attributed to radiation from a reverse shock (Sari & Piran, 1999), and we suggest that this may explain the bright early-time radio point for GRB 980329.

4.5 GRB 980703: The Details

GRB 980703 triggered the *BATSE* detectors of the *Compton Gamma-Ray Observatory* (Kippen *et al.*, 1998), and its afterglow was detected by the *Rossi X-Ray Timing Explorer* (Levine, Morgan & Muno, 1998). Both an optical and a radio afterglow were identified (Frail *et al.*, 1998), and from host galaxy emission and absorption lines, Djorgovski *et al.* (1998b) identified its redshift as z=0.966. The following discussion outlines the data taken, and then explains the model fit results; it is largely taken from our work presented in Frail *et al.* (2003b).

The afterglow has a broadband data set including optical/NIR, radio and X-ray measurements (from the *BeppoSAX* satellite). The optical/NIR data has good frequency coverage with observations in the *BVRIJHK* bands (Bloom *et al.*, 1998; Castro-Tirado *et al.*, 1999b; Vreeswijk *et al.*, 1999; Holland *et al.*, 2001; Sokolov *et al.*, 2001). The radio data is multi-frequency with detections at 1.43, 4.86, and 8.46 GHz (Berger, Kulkarni & Frail, 2001; Frail *et al.*, 2003b) and upper limits in the high frequency radio (15 GHz), and the submillimeter (220 GHz) (Frail *et al.*, 2003b). The X-ray observations of Vreeswijk *et al.* (1999) are included, converted to flux density using their observed photon index (with the resulting factor that 1 Jy = 2.4×10^{-11} erg cm^{-2} s^{-1}).

The data has two features worthy of comment. The first is that the host is quite bright. Its optical

Table 4.4: Best models for GRB 980703. The Wind density profile case is depreciated due to extreme parameters; the ISM fit is the best model overall (see text).

Parameter	ISM	Wind
χ^2 for 162 data pts	170.4	171.4
$t_{\rm jet}$ (days)	3.43	5.11
$t_{\rm nonrel.}$ (days)	49.6	26.4
$t_{\nu_{\rm c}=\nu_{\rm m}}$ (days)	1.41	5.17
$E_{\rm iso}(t_{\nu_c=\nu_m})(10^{52}$ erg) [a]	11.8	0.66
n/A*	27.6	1.42
p	2.54	2.11
ϵ_e (fraction of E)	0.27	0.69
ϵ_B (fraction of E)	1.8×10^{-3}	2.8×10^{-2}
$\theta_{jet}(rad)$	0.234	0.310
host A(V)	1.15	1.33
host B (μJy)	2.93	2.94
host V (μJy)	3.07	3.07
host R (μJy)	3.61	3.64
host I (μJy)	4.84	4.81
host J (μJy)	8.77	8.67
host H (μJy)	9.15	9.00
host K (μJy)	10.1	10.0
host 1.4 GHz (μJy)	53	58
$E_{\rm iso}(\gamma)$ (10^{52} erg) [b]	6.01	6.01
$E(\gamma)$ (10^{50} erg)	16.5	28.9

---

[a] Isotropic equivalent blast-wave energy (not corrected for collimation).

[b] Isotropic-equivalent energy emitted in the gamma-rays taken from Bloom, Sari & Frail (2001).

flux, R ~22.6 (Djorgovski *et al.*, 1998) (or its portion underlying the optical afterglow's position) limits the optical data's utility to a few days post-burst. Figure 4.3 shows its R band lightcurve against the other three events; they have host flux components of 0.1–0.2 μJy while 980703's is $\sim 3\mu$Jy. The host flux dominates the optical flux received after just a few days rather than a week or more, preventing the data from strongly constraining the optical decay rate. It is also bright in the radio. Berger, Kulkarni & Frail (2001) showed that the radio flux includes a host component visible at late times, and determined its spectral index is -0.32.

The second is the presence of a peak flux cascade (see the discussion of §4.4.1), the flux at the peak declining steadily across the radio bands. The drop in peak flux can be seen from 1.43 to 8.46 GHz in Figures 4.14 and 4.15. This is similar to the observations of GRB 980329's afterglow. §4.4.1 discusses this observation and its potential causes (as does §4.3 for the 970508 afterglow, whose data hints at, but ultimately does not require, a peak flux cascade). A strong cascade in peak flux values may be caused by a Wind-like circumburst medium, or post-jet evolution.

4.5.1 Two Possible Fits to 980703

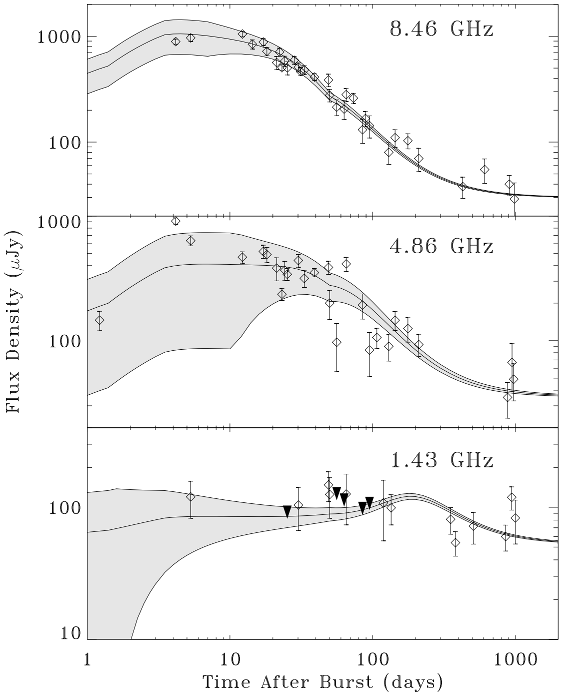

Figure 4.14: Radio light curves of the GRB 980703 afterglow. The solid line is the best-fit model, which has an ISM circumburst density profile. The model light curves are plotted with the estimated $1\,\sigma$ scintillation envelopes. Data that is not detected with $2\,\sigma$ significance is given as $2\,\sigma$ upper limits (solid triangles)

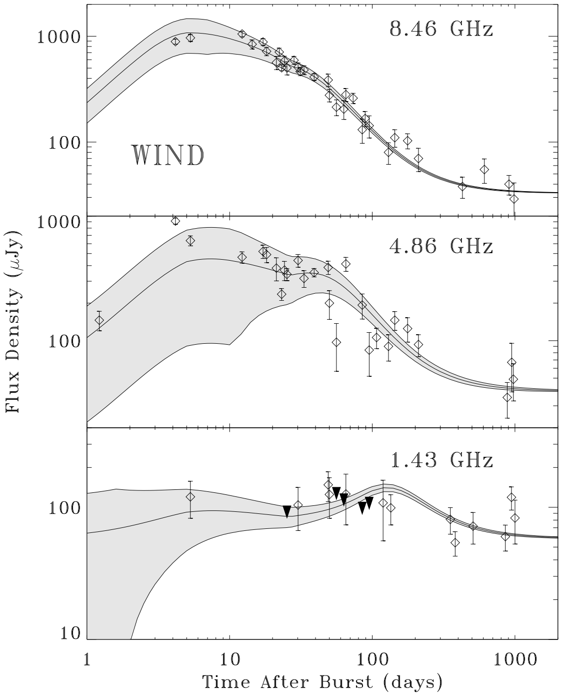

Figure 4.15: Radio light curves of the GRB 980703 afterglow. The data is identical to that in Figure 4.14. The solid line is the best model for a Wind density profile. The two fits are nearly equally good. The ISM model is strongly preferred as the Wind model has extreme parameters.

We fit the data set to the full model (as described in §3.1,3.4). It required independent optical/NIR host components in each band, and a radio host (fixing the spectral index at -0.32 as per Berger, Kulkarni & Frail (2001), with the flux scaled to 1.43 GHz). The submillimeter limits did not require a host component. We attempted fits to both types of density profile; the two resulting good fits are presented in Table 4.4.

The best model is a collimated jet into an ISM-like medium of substantial (~ 28 cm^{-3}) density, with a jet break at 3.4 days. The collimation is necessary to provide a peak flux cascade observed at radio wavelengths. We note that no break can be seen in the optical data due to the host

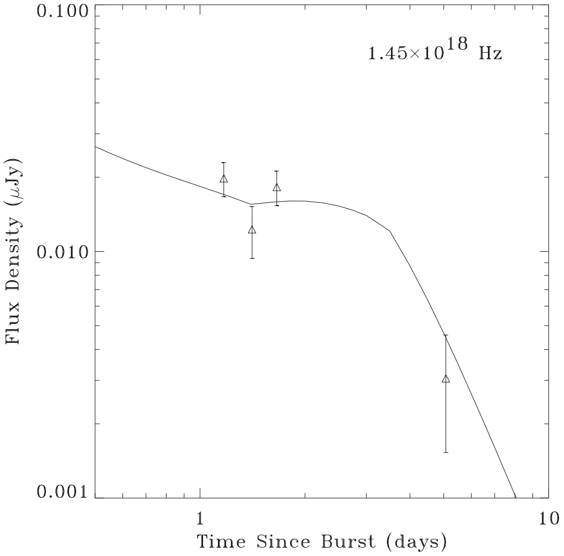

Figure 4.16: X-ray lightcurve of the GRB 980703 afterglow. The solid line is the best-fit model, which has an ISM circumburst density profile. The early flatness and curvature are signatures of a significant contribution of inverse Compton upscatters to the X-ray afterglow flux at that time. The jet break at 3.4 days can be seen.

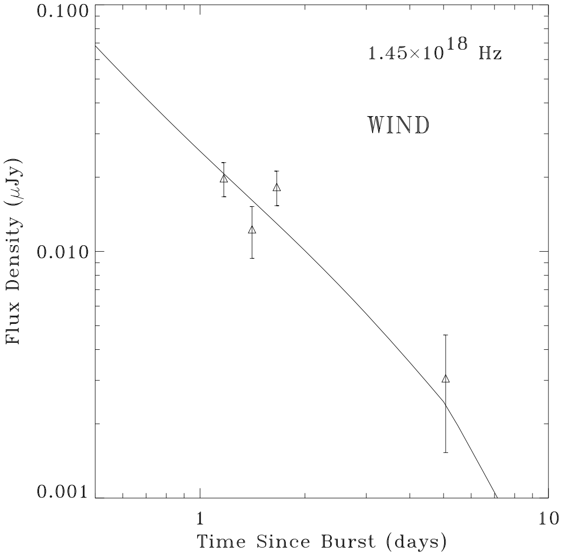

Figure 4.17: X-ray lightcurve of the GRB 980703 afterglow. The data is identical to that in Figure 4.16. The solid line is the best model for a Wind density profile, as discussed in the text. Its jet break is not until five days post-burst and is not as visible.

predominance after a few days. This hides the classic jet break signature. This is similar to the model for GRB 980329 (§4.4.2), which also fit a peak flux cascade via post-jet evolution; in that case the signature is not seen in the optical due to the late discovery of the afterglow and so sparse optical sampling. The fitted extinction at the host is substantial (A(V)∼1.2, assuming an LMC-like extinction law) as is the energy fraction in the shocked electrons ($\epsilon_e \sim$0.27).

This is not a unique solution. A Wind-like (r^{-2}) density profile could fit the data equally well (Table 4.4, the difference in χ^2 is negligible). Although an r^{-2} profile produces a peak flux cascade, it is not as strong as that from a jet break. An isotropic Wind-like fit cannot fit the data as well, only a jetted Wind-like fit can. The two jetted fits are compared in Figures 4.14 and 4.15 (8 GHz) and Figures 4.16 and 4.17 (X-ray).

However, we reject the jetted Wind-like case as the best fit on the grounds that at least one of its parameters is extreme: it requires 70% of the shock's energy to be in the electrons. It would also require the energy during the afterglow phase to be $\lesssim 1/10$ of the energy from the prompt γ-ray emission (see Table 4.4). If the shock energy were that low just after the prompt GRB emission, it would require an extremely high γ-ray conversion efficiency ~90%. (We note, though, that the extreme radiative corrections expected for $\epsilon_e = 0.69$ would decrease the energy by a factor of ~ 150 from the GRB to the afterglow phase. If the shock energy were 150 times higher just after the γ-ray phase, the efficiency would be a reasonable 5%.) Since the extremes presented by these parameters are not realistic, overall we consider the best fit to be the jetted ISM-like case. That model is presented with the best fits for all the events in Table 4.2 and Figures 4.3, 4.4 and 4.5.

4.6 GRB 000926: The Details

The discovery of this event and character of its data are presented in §4.1 and will not be repeated here. The data set comprises 114 measurements from the radio to the X-ray and there is a clear steepening in the optical bands approximately two days after the GRB event, interpreted as a jet break.

This event was used in early model fits that did not take into account radiative corrections to the shock energy. It showed that inverse Compton (IC) scatters as the dominant cooling source greatly improves the fit, and that a Wind-like density profile provides a significantly worse fit than an ISM-like one. Its best-fit parameters required a substantial electron energy fraction $\epsilon_e \approx 0.3$. The availability for radiation of a large fraction of shock energy demonstrated that the assumption of full adiabaticity was not a suitable one.

We applied the full model with radiative energy loss corrections (§3.1, 3.4) to the 000926 data set. The underlying optical host fluxes were included in the fit; a nearby galaxy "arc", within the point-spread function of the ground-based data, contaminated those observations and was removed as before (Price *et al.*, 2001). There nevertheless was underlying host flux at the $\sim 0.2\,\mu$Jy level.

The fits described above (in Table 4.1) were used as a rough guide to the range of useful starting points for the fitting parameters. The best fit to the full model is included in Table 4.2 of all the events' best fits, and is shown in Figures 4.3, 4.4, 4.5 and 4.18. As expected from the previous poor results, the Wind-like density profiles again produced substantially poorer fits than those utilizing ISM-like densities.

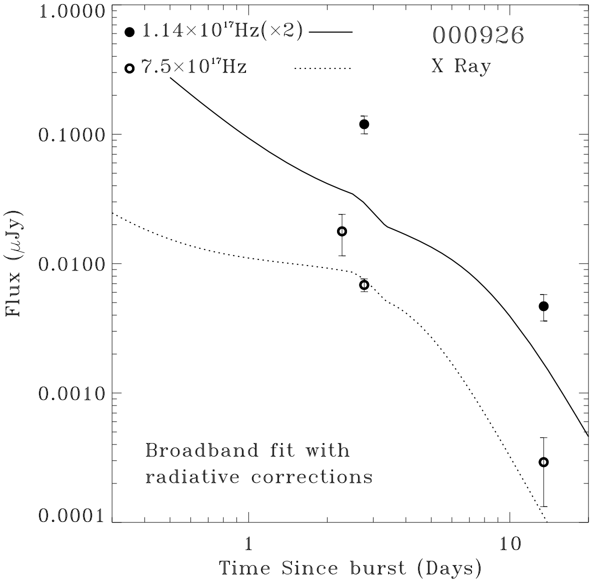

Figure 4.18: GRB 000926 X-ray afterglow lightcurve from *BeppoSAX* and *Chandra*. The *Chandra* data have been broken into two bands, hard (1.5–8 keV) and soft (0.2–1.5 keV), with center frequencies weighted by a photon index of 2. The data is corrected for absorption in our Galaxy. The model is from the broadband fit to the full data set with the full model, including radiative corrections. The best model is similar to the broadband fit which did not apply radiative corrections to the energy, but the fit with radiative losses is distinctly worse in the X-ray (compare to Figure 4.2).

The chief modelling change was the inclusion of energy corrections. This did indeed affect the model fit as the best fit without energy corrections had a non-negligible ϵ_e, from which significant energy corrections follow. As seen from the energy dependences for the spectral parameters (peak and break frequencies, Equation 3.4), the peak will drop directly with energy corrections. The injection break ν_m from the minimum electron energy (which tends to be the peak frequency) drops more slowly, and the self-absorption break drops quite slowly with energy corrections. The cooling break ν_c's decline is slowed by the energy losses. The previous good fit relied in part on the IC-dominant cooling that makes ν_c low, and no peak flux cascade is visible in the data. The self-consistent energy corrections oppose aspects of the good fit. They are minimized in the best fit to the full model.

The best fit was still a "high-IC" solution where Compton scatters dominate the cooling rate, with a substantial ISM-like density. As seen in comparing Tables 4.1 (with the solution without radiative corrections) and 4.2 (with radiative corrections), parameters have changed by factors of order unity (up to 2). In particular, ϵ_e has decreased to 0.15, minimizing the radiative corrections that were not required for a good fit in the early model. Other parameters changed by similar factors; the density n decreased from 27 to 16 cm^{-3}, and the magnetic energy fraction increased from 0.8 to 2.2 %. However, some changes were smaller, with the collimation angle increasing from 0.14 to 0.16 radians, the isotropic-equivalent energy decreasing from 1.8 to 1.2×10^{53} ergs, and the electron energy distribution index increasing from 2.43 to 2.79.

With the energy, we estimate the γ-ray production efficiency in the prompt emission (by comparison with the GRB fluence). For GRB 000926, the k-corrected value for the isotropic-equivalent γ-ray release (that is, extrapolated to the 20–2000 keV release in its host frame) is approximately 3×10^{53} ergs (Bloom, Frail & Sari, 2001). This is higher than the shock energy derived in the fit without radiative losses (1.8×10^{53} ergs), which would require a high level γ-ray production efficiency $\approx$ 60%. The expected rate of energy losses for ϵ_e in that early fit, however, would have given a factor of nine increase in energy from Day 1 (when the afterglow observations had begun) extrapolated back to 100 s (just post-burst), requiring only an efficiency of $\approx$ 15%. The required γ-ray production efficiency is higher for the fit to the full model as the radiative losses are minimized and the afterglow energy requirements are similar. We extrapolate the shock's isotropic-equivalent energy as found in the fit using the model's calculational routines and find its energy at 100 seconds would have been 5.2×10^{53} ergs. This implies an efficiency of $\approx$ 40%, somewhat higher than most estimates in the internal shock model for the prompt emission (Beloborodov, 2000; Spada, Panaitescu & Mészáros, 2000; Guetta, Spada & Waxman, 2001), but not as high as the most extreme predictions for "ultra-efficiency" (see Kobayashi & Sari, 2001).

Finally, the fit is not as good, reflecting the incompatibility found in the early result's substantial ϵ_e and the required accounting for radiative losses. In particular, while the X-ray still requires flux above the synchrotron's level, the parameter changes cause the IC flux estimate to no longer match the data as well. As a result, the χ^2/DOF (degrees of freedom) has worsened from 124/93 to 138/93. The probability by the χ^2 test that the data is fully described by the model, having a source from that distribution, has worsened from 0.017 to 0.0012.

Chapter 5

Comparisons of Best-Fit Parameters

In this chapter, we discuss the similarities and differences of the fundamental physical parameters inferred from the model fits to the four events described in Chapter 4. The discussion is largely taken from our work presented in Yost *et al.* (2003).

Table 4.2 presents the best fits using the basic assumptions described in §3.1 (also see Figure 5.1). The table includes statistical 68.3% confidence intervals for the parameters, calculated from (non-Gaussian) distribution histograms generated by 1000 or more Monte Carlo bootstraps. The results show a great deal of diversity in the values, similar to other efforts (e.g., Panaitescu & Kumar, 2001b). The fits can be seen in Figures 4.3, 4.4, and 4.5.

Neither the variation in, nor the values of the energy/geometry and environmental parameters, is surprising. Variation is seen in the energies of the prompt GRB emission (Frail *et al.*, 2001). Moreover, if GRBs are related to the deaths of massive stars (see the review by Mészáros, 2002, and references therein) then we would not expect such parameters to be identical due to variations in progenitor mass, angular momentum and environment.

The best fits for these four events have an ISM-like density profile. We note that a Wind-like profile produces reasonable fits in two cases, albeit disfavoured by comparison with the event's ISM-like fit (see §4.3.2 and §4.5.1). The densities are comparable to the Milky Way's ISM density at the low end, and to the density of diffuse clouds for the three with $n \sim 20\,\mathrm{cm}^{-3}$. This is not an extremely wide range of densities. Densities can vary from halo-like, $\ll 10^{-3}\,\mathrm{cm}^{-3}$, to those of molecular cloud

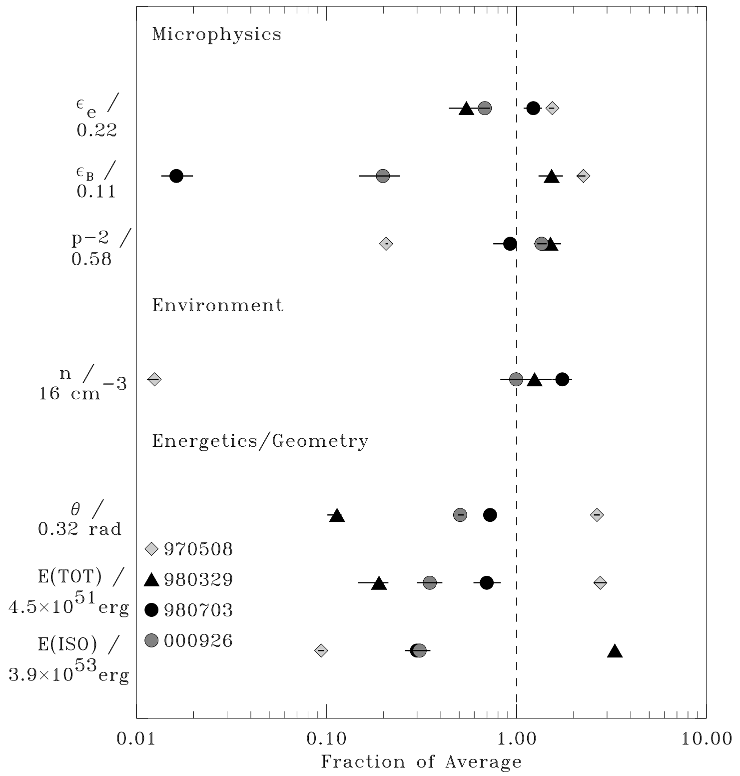

Figure 5.1: Parameters from the best fits with the simple model assumptions (see Table 4.2). They are divided into three categories: energy & geometry (kinetic energy, collimation half-opening angle θ), environment (density), and microphysics (energy partitions: ϵ_e for electrons, ϵ_B for magnetic fields, and electron energy distribution index p). See §3.1 for further details concerning the fireball model's parameters. They are presented relative to a nominal value as indicated; the error bars are the statistical 68.3% intervals calculated via Monte Carlo bootstraps. The diversity in energy, geometry, and environment is not unexpected for some variation in progenitor properties. Shock physics, however, is expected to depend only on shock strength. The variation of these parameters by orders of magnitude suggests that some effect is unaccounted for in the model.

cores, $\gg 10^4\,\mathrm{cm}^{-3}$. These densities are typical of other efforts with significant radio data, which constrains the synchrotron self-absorption (e.g., Panaitescu & Kumar, 2001a). While the core-collapse GRB progenitor hypothesis results in the death of massive short-lived stellar progenitors within a stellar birth environment, with dense molecular cloud cores, these lower densities are not inconsistent with that hypothesis. Diffuse clouds are also associated with star-forming regions, and such densities are found in the interclump medium that dominates molecular cloud volumes in the Galaxy (Chevalier, 1999, and its references). Moreover, massive stars modify their environment, making direct interactions with the dense cloud cores unlikely (Chevalier, 1999).

However, the model fits favouring ISM-like density profiles over Wind-like ones is unanticipated in light of evidence that points toward an association between GRBs and massive stars. This evidence, reviewed by Mészáros (2002), includes that the positions of GRBs within their host galaxies track star-formation regions, and that several afterglows show possible late "red bumps" that could indicate an underlying supernova, expected if the GRB were produced by the death of a massive star. More recently, Stanek *et al.* (2003) associated a supernova with the nearby bright GRB 030329 by observing the rise of the supernova spectrum in the fading afterglow.

Clearly, some GRBs are associated with the deaths of massive stars, stars that should modify their environments via wind outflows. Yet the Wind-like profile does not produce a better fit to the four afterglows considered. It is possible that only a subset of GRBs are produced by progenitors in "windy" environments. There may be more than one type of progenitor, or the outflows from massive stars that yield GRBs may produce environments no better described by an r^{-2} density profile that by a constant density. For example, if the outflows do not vary in a regular fashion the enriched environment would not have a single smooth profile. The density profile would resemble neither of the cases we considered. Another speculation is the possibility of progenitors with anisotropic wind outflows, enriching part of their environments, but leaving some large regions with near-constant densities. In subsequent chapters, we examine the level of model uncertainty from certain model assumptions. Chapter 8 studies the effects of various density profiles.

The total kinetic energies inferred in the fits (10^{51}–10^{52} ergs) are roughly comparable, though at the high end, with the range of total γ-ray energies expected from the studies by Frail *et al.* (2001). On a case-by-case basis, we check if they are reasonable by comparison with the γ-ray energies. The γ-ray energies employed are those of Bloom, Frail & Sari (2001), which are "*k*-corrected", transforming them to isotropic-equivalent values in a fixed 20–2000 keV comoving bandpass by accounting for the redshift and spectrum of the GRB event. The ratio of the isotropic-equivalent kinetic energy (at one day post-burst) and γ-ray energy (over the GRB) varies from 0.5 to 5. However, the modelled energy corrections would give fireball energies three to ten times higher at the end of the burst; the implied γ-ray efficiency would then be 3–10% in three cases, and 40% for GRB 000926. The lower efficiency values are quite compatible with theoretical expectations.

For 000926, the efficiency is near the high end of the predictions (see Beloborodov, 2000; Spada, Panaitescu & Mészáros, 2000; Guetta, Spada & Waxman, 2001; Kobayashi & Sari, 2001).

Thus the environmental and energy parameters are quite reasonable in the present framework. What is somewhat unexpected is the lack of universality in the microphysical parameters. Values of ϵ_e are fairly uniform, only varying by a factor of 2, but the values of ϵ_B vary by a factor of 100. The index p is expected to be in the range of 2.2–2.3 (Kirk *et al.*, 2000; Achterberg *et al.*, 2001) but its values span from 2.1 to 2.9. While relativistic shocks are not well-understood (neither fully modelled from first principles, nor measured in the lab), the physics occurring at a shock boundary should only be a function of the shock strength, or equivalently here for a relativistic shock, its Lorentz factor. A spread by two decades in ϵ_B would therefore be unexpected if everything is properly accounted for in the model. We would expect the microphysical parameters to be near-universal.

If the spread in the microphysical parameters does indeed exist, then highly relativistic shocks behave nonintuitively. However, the apparent spread could be due to the overall uncertainty in the model, a parameter such as the viewing angle that is not fully accounted for or nonuniqueness of the model fits. We have already noted that there are at least two nonunique fits: GRB 980329 with a highly radiative fit, and GRB 980703 with an r^{-2} density profile fit disfavoured due to extreme parameters. This leaves open the question as to whether there may be equally good fits with reasonable parameters (perhaps under other model assumptions). It is therefore important to check if the model, with the very simple assumptions we have employed, is constrained only to these fits by the data. The assumptions could be too simple, and the following chapters explore fits employing other model assumptions in order to constrain some interesting aspects of the model uncertainty.

Chapter 6

Bursts the Model Could not Fit Well

We made attempts to fit other bursts than the four presented in Chapter 4. These attempts were not very successful. The modelling difficulties generally fell into two categories: where the data was as extensively sampled as the best cases yet its behaviour presented significant difficulties in fitting to any simple model, and where fits to the model presented some difficulties and the data were not as extensive as our best cases.

It is useful to discuss these cases for several reasons. First, while we examined “good fits” in Chapter 4, even the best are formally poor fits with large χ^2. We determine that a fit is successful when it matches the trends in the data. By contrasting these with poor fits, we clarify the degree to which good fits match the data. Secondly, even cases with more than the minimal sampling to determine the existence of an afterglow may yield less extensive data sets than those events elaborated in Chapter 4. Such cases show the limitations of data set constraints upon the model when the model fails to produce an unambiguous good fit. Finally, events where the data shows features that are unaccountable by any simple model demonstrate that we do not understand the model physics (or environment) in all cases. As the basic model clearly is sufficient to describe some similarly sampled afterglows, there is some clear diversity amongst events. There may be different progenitor types, or different environments, indicated by this diversity. A study of a large sample both of the successfully modelled events and of those where the basic model fails may render clues to underlying populations.

In the following, an isolated "event" in the data not accounted for in the basic model is not sufficient to specify a bad fit. GRB 970508 showed such an event, a sudden rise at $t = 1 - 2$ days. In that case, there are reasonable hypotheses for the rise, and the trend of the data after the rise was matched by the model. Almost invariably, we determine a poor fit by the model's inability to match the general trends in the data, such a the rise or decay rates, or peak levels and times. There are a couple of cases with multiple causes: 000418 and 991216 both have model mismatches in the radio that are not as severe as other examples, and also have extreme parameters even to produce these marginal fits. Finally, there is one marginal case, 990510, where no reasonable fit was possible without refining the weights given to various parts of the data set. Even a good fit produced in that fashion is ambiguous, as a large difference results from fits that simply treat the data somewhat differently.

6.1 Data Behaviour Beyond the Basic Model

In some cases, the data definitely shows deviations not expected by any smooth, self-similar evolutionary model. The result is the expectation that in at least some cases, the fireball model is completely inadequate. We have encountered such situations in the 990123, 991216, 000301C, and 010222 events. The data may be explained by a model related to the fireball, but with changed assumptions or additions. Whether data regions require some theoretical accommodation is considered on a case by case basis. 970508 was a similar case, with an early deviation from its flux decay, but whatever occurred there was isolated to the first two days; by contrast, the data sets considered here may have odd features occurring in the middle of the afterglow, or ongoing throughout.

990123

This event was a very bright *BeppoSAX* burst, generating intense interest among GRB astronomers as the robotic telescope *ROTSE* discovered its optical emission *contemporaneously* with the GRB (Akerlof *et al.*, 1999). It was noted for its intense γ-ray fluence. At a redshift z=1.60, its isotropic-equivalent energy release in the γ-rays was over 10^{54} ergs (Briggs *et al.*, 1999; Kulkarni *et al.*, 1999a).

The data showed several interesting features. The prompt optical emission, the "optical flash", rose then decayed $\sim t^{-2}$ (Akerlof *et al.*, 1999). The optical afterglow decayed more slowly, $\sim t^{-1.1}$, but then showed a break to steeper decay (Fruchter *et al.*, 1999; Castro-Tirado *et al.*, 1999a; Kulkarni *et al.*, 1999a). This was the first strong evidence for jets in GRBs. The radio afterglow was also unusual, described as a "flare" one day post-burst, rising $\sim t^{0.8}$ and decaying $\sim t^{-1.3}$ (Kulkarni *et al.*, 1999b).

The afterglow generated great discussion. The steepening circa two days post-burst has been interpreted as a jet break (Kulkarni *et al.*, 1999a; Castro-Tirado *et al.*, 1999a), but also as a rapid transition to non-relativistic evolution in a dense ($n \sim 10^6\,\mathrm{cm}^{-3}$) medium (Dai & Lu, 1999). The optical flash has been interpreted as emission from a reverse shock plowing (for a limited time) back through the shell of ejecta (Sari & Piran, 1999), but also perhaps as emission from internal shocks in the prompt phase (Mészáros & Rees, 1999). The radio flare is expected from the reverse shock scenario; Kulkarni *et al.* (1999b) show that a two-component model (reverse shock providing the radio flare, forward shock the optical afterglow at one day) may reconcile the observations.

We assembled the broadband data set using published X-ray, optical, and radio data. We determined the flux density (and effective frequency) in the X-ray band at the beginning and end of *BeppoSAX* afterglow followup from the times, decay power law, and photon index reported by Heise *et al.* (1999), along with the initial X-ray flux as reported by Castro-Tirado *et al.* (1999a). For the optical, we assembled the multiband tables of Castro-Tirado *et al.* (1999a); Galama *et al.* (1999); Kulkarni *et al.* (1999a) and included the late-time host observations of Fruchter, Thorsett & Wijers (2000) and Bloom *et al.* (1999), using the *UBVRIHK* and *gunn-r* bands. At radio and submillimeter wavelengths, we took the data from Kulkarni *et al.* (1999b) and Galama *et al.* (1999), with data at frequencies of 1.38, 4.88, 8.46, 15, 86.5, 142.3, 212.6, 222, 228.9, 232, 353, and 666 GHz.

Taking the radio flare as emission from the reverse shock traversing the ejecta, we ignored radio data before three days post-burst, leaving us with no proper detections. This data set could not be properly fit by the model. Much of the post-break (expected to be post-jet) evolution has significant host flux contributions. Moreover, the radio data has little leverage; it may limit the afterglow brightness but does not give a measured peak flux or peak crossing time. Model fits would generally not converge; those that did both fit poorly and had extreme parameters (ϵ_e and $\epsilon_B \to 1$).

With effectively no low-frequency information, we are not able to constrain the model. The forward shock fireball model fails to describe the data (even ignoring the radio flare). They may arise from a different mechanism, from some additional component compatible with a fireball, or from a fireball with different assumptions (concerning the range or behaviour of its physical properties) than those we have considered.

991216

This bright GRB was detected by *BATSE*, and followup observations by the *RXTE* satellite detected an X-ray afterglow (Takeshima *et al.*, 1999), refining the event's known position. Uglesich *et al.* (1999) identified the fading optical afterglow; Vreeswijk *et al.* (1999a) determined its redshift, z=1.02. Frail *et al.* (2000) identified a radio afterglow and followed its evolution from ≈ 1.5 days post-burst.

From the extensive observations, we assembled a broadband data set. This included radio and submillimeter at 1.43, 4.86, 8.46, 15, 100, and 350 GHz (Frail *et al.*, 2000). We also employed optical and near-infrared *VRIJHK* data from the journals (Garnavich *et al.*, 2000; Halpern *et al.*, 2000; Sagar *et al.*, 2000) as well as the GCN Notices: Uglesich *et al.* (1999); Henden *et al.* (1999); Mattox (1999); Vreeswijk *et al.* (1999); Kassin (1999); Leibowitz *et al.* (1999); Schaefer (1999) (when no uncertainties were quoted, we adopted 0.3 magnitudes). We also included X-ray data. This consisted of the *RXTE ASM* observations reported by Corbet & Smith (1999), the *RXTE PCA* observations of Takeshima *et al.* (1999), and the *Chandra* observation (Piro *et al.*, 1999). Corbet & Smith (1999) reported 2–10 keV fluxes in mCrab; we converted them to cgs employing the W3PIMMS[1] utility (Mukai, 1993), with the reported photon index of 2.1. The spectral shape of the X-ray afterglow was consistently a power law with photon index of 2.1, which was employed in all cases to determine a flux density and

---

[1] WebPIMMS is a Web version of the PIMMS (v3.3a) tool. PIMMS was developed by Koji Mukai at the High Energy Astrophysics Science Archive Research Center (HEASARC). Effective area curves for current and future missions have been supplied by the respective projects. XTE specific subroutines have been written by Koji Mukai, with the help of Jim Lochner and Phil Blanco. The SAX specific subroutine has been written by the SAX Data Center and Lorella Angelini. Snowden R-band effective area curves for ROSAT PSPC have been created by Richard West of Leicester.

W3PIMMS is available at: http://heasarc.gsfc.nasa.gov/Tools/w3pimms.html a characteristic X-ray frequency. We determined the representative times of the observations from the reported start and stop times employing Halpern *et al.* (2000)'s fit to the X-ray decay of $t^{-1.6}$, calculating the expectation, $< t >$. The X-ray flux densities were given minimum uncertainties of 10%. This burst occurred at a fairly low Galactic latitude (l, b)=(190.4°, −16.6°) (coordinates from Uglesich *et al.*, 1999, converted via NED[2]). Its de-reddening for Galactic extinction is thus somewhat more important; we adopt $E(B-V)$=0.626 from Schlegel, Finkbeiner & Davis (1998)'s calculation of the extinction measure at the *Chandra* position (Piro *et al.*, 1999). We applied a 5% broadband uncertainty in quadrature with all reported uncertainties in an attempt to address systematic differences in flux calibration.

This event shows some difficulties in reconciling data from multiple observers with different methods. Some of the unrefereed data (from the *gunn-i* band, reported on the GCN Notices) falls beneath the multiband optical spectrum around the same time, so we ignore it. Halpern *et al.* (2000) report that their K band observation does not fit on the power law spectrum formed by their multiband (*VRIJHK*) data. It falls beneath the extrapolation of the other data, as if a spectral peak occurs there. They acknowledge that their K point is discrepant with the nearly simultaneous K observations of Garnavich *et al.* (2000), whose measurement presents no such difficulty.

Beyond such minor discrepancies, the data is acknowledged to show non-standard features, notably that the radio flux declined steadily from its discovery, peaking earlier than 1.5 days.

Frail *et al.* (2000) have summarized the data's behaviour as decaying by power laws in the radio, optical, and X-rays, but at different rates, increasing with frequency from $t^{-0.8}$ in the radio to $t^{-1.3}$ in the optical and $t^{-1.6}$ in the X-rays. They find that a single standard fireball shock passing from the radio through the optical and X-ray is discrepant with the observations; it would require a rising radio flux for at least the first few days. They suggest either a forward shock model for the optical and X-ray with a cooling reverse shock dominating the radio emission for several days, or a two-component forward shock model, in which one fireball dominates the high frequencies and a second dominates the radio, decoupling the fluxes.

---

[2] http://nedwww.ipac.caltech.edu/forms/calculator.html

Halpern *et al.* (2000) inferred a break in the optical lightcurve, from $t^{-1.2}$ to at least $t^{-1.5}$, and perhaps as steep as $t^{-2.1}$, around one to two days post-burst, but found that the X-ray lightcurve at < 1 day was already as steep as $t^{-1.6}$. They suggest a gradual jet break is occurring in the optical, and that the jet may be layered with a more-collimated higher-energy core that "breaks" earlier and dominates the high (X-ray) frequencies.

Panaitescu & Kumar (2001b) took another approach in modelling this event. They explain the observations with a single fireball, but postulate a broken power law distribution of electron energies. That is:

$$N(\gamma) \propto \gamma^{-p}, \quad (\gamma_m < \gamma < \gamma_M)$$

and

$$N(\gamma) \propto \gamma^{-q}, \quad (\gamma_M < \gamma)$$

with γ_m and γ_M calculated so that the total electron energy is a fraction of the shock energy, and γ_M (with corresponding frequency ν_M) represents a break at a constant fraction of the electrons' energy. γ_m and subsequently ν_m can be quite low, and $p < 2$ allows the shallow radio evolution while higher frequencies above ν_M behave more conventionally with $q > 2$. They find a good fit with $p \sim 1.4$ and $q \sim 2.1$, with the break allowing ~ 0.5 of the electron energy below γ_M.

Given the previous work, we expected and found difficulties in fitting the data with our broadband model. Although Frail *et al.* (2000) and Halpern *et al.* (2000)'s work did not include radiative corrections or inverse Compton upscatter effects, the data's unusual features were not related to the behaviour expected by these effects.

Our single forward-shock model cannot fit the early radio data. Its early decay is not compatible with the higher frequencies. All reasonable fits required ignoring radio data before ≈ 3.5 days post-burst. While this could be justified as a reverse shock's dominance, the steady decline (seen in Figure 6.1) shows no transition with a forward shock rising above the flux of the reverse shock. For this reason alone, we suspect that even a good fit after 3.5 days would not model the true nature of this event.

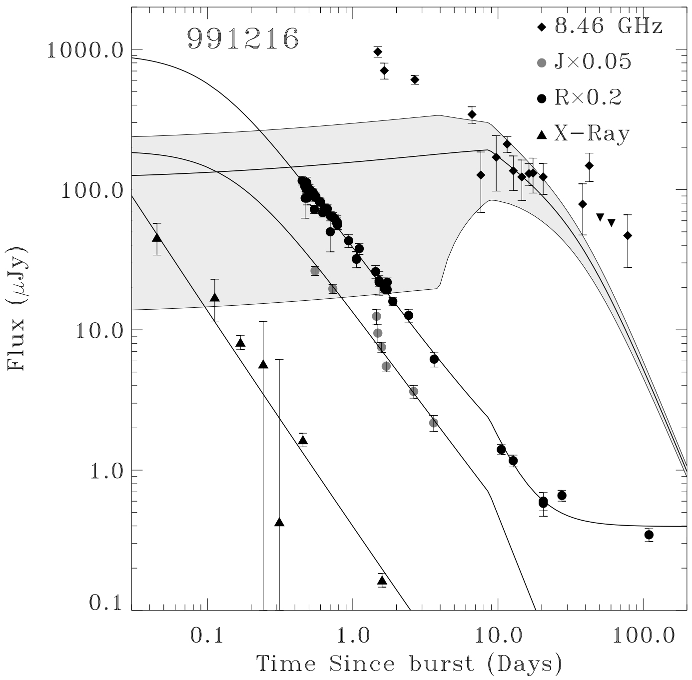

Figure 6.1: Selected radio and optical bands, as well as the X-ray observations of the 991216 afterglow. Our best-fit model is also shown; the light grey envelope shows the estimated fractional uncertainty applied to the model's flux based upon the expected degree of interstellar scintillation for an extragalactic source along that line of sight. The model has an ISM-like density profile and collimation providing a jet break at ≈ 9 days—not a satisfactory description of the event. While the X-ray and optical decays can be reasonably reconciled, the radio flux's steady decline does not fit with the time required by broadband considerations for the passage of the spectral peak. This may be the signature of the reverse shock dominating the early radio flux, yet the radio data declines much more slowly than the higher frequencies. Frail *et al.* (2000) have suggested a two-component model where a second, lower-γ fireball dominates the radio emission.

Our best results were for an ISM-like density profile, and required an extremely high ϵ_e (and so extreme radiative corrections). The model is collimated, but its jet break is later, circa Day 9, than the one to two days post-burst reported by Halpern *et al.* (2000), due to a high energy and low density. Wind-like models with and without jetted ejecta fared far more poorly. The model's parameters are: $E_{iso} \approx 8 \times 10^{54}\,\mathrm{ergs}$, $\theta \approx 0.07$ rad (so $E_{tot} \approx 2 \times 10^{52}\,\mathrm{ergs}$), $n \approx 4 \times 10^{-4}\,\mathrm{cm}^{-3}$, $A(V)$ was determined to be negligible, $p \approx 2.05$, $\epsilon_e \approx 0.7$, and $\epsilon_B \approx 0.03$. This fit is shown in Figure 6.1, where we include the early radio data for comparison.

The χ^2 is 155.1 for 108 data points, with 100 degrees of freedom, giving a probability of 0.00018 that the data is from the model distribution. The χ^2 ignores the systematic problem in fitting the early radio data. In addition, the high ϵ_e makes our approximations for the radiative corrections, and so the resulting model evolution, questionable. We do not consider our model a proper description of the data. We concur with other researchers that the basic fireball model is inadequate for this event.

000301C

This 2-second-long event was detected by the Interplanetary Network of satellites' γ-ray detectors. Jensen *et al.* (2001) describe the discovery of the GRB, its optical afterglow, and its redshift z=2.04. They determine its duration and hardness ratio, and place it at the border of the Long/Soft and Short/Hard classes of GRBs described in Chapter 1; it may belong to either class of events.

The event was well-followed at radio and optical/NIR wavelengths, but no X-ray observations were available. The optical/NIR observations included *UBVRIK* bands (Masetti *et al.*, 2000; Jensen *et al.*, 2001; Rhoads & Fruchter, 2001), and the radio/submillimeter observations included 1.43, 4.86, 8.46, 15, 22.5, 100, 250, and 350 GHz bands (Berger *et al.*, 2000). For our analysis, we have taken the broadband data set employing all these wavelength bands as compiled by Berger *et al.* (2000), including their flux conversions and de-reddening for Galactic effects.

The data demonstrated peculiar features: the optical decay steepened as seen in other cases, but to a more rapid decay than seen in other events, $\sim t^{-2.7}$ (Berger *et al.*, 2000; Sagar *et al.*, 2000; Masetti *et al.*, 2000), and a definite bump appeared from $\approx$ 3–4.3 days above the optical's broken power law evolution (e.g., Berger *et al.*, 2000; Sagar *et al.*, 2000). Masetti *et al.* (2000) reported more significant variations in the well-sampled R band, with a brightening at the start of observations, and a plateau phase around five to seven days post-burst, after the bump. Berger *et al.* (2000) gave evidence from submillimeter observations that the flux bump may be achromatic. Given the bump's rapid variability, poor sampling in a band complicates its interpretation. Rhoads & Fruchter (2001) fit an earlier break to the K' band (with data to eight days post-burst) than the break in the R band (with data past a month). Berger *et al.* (2000) find a break in the optical after seven days and demonstrate that the R data before eight days would also apparently break earlier, around the time of Rhoads & Fruchter (2001)'s K' break. Broadband modelling is clearly indicated to resolve all the data consistently.

Numerous efforts have been undertaken to provide a model for this event. These generally fall into two categories: models that explain the general trends in the data (including the steep late evolution), and models for the deviation(s) from the general trends. A few efforts attempted to address all matters simultaneously.

Garnavich, Loeb & Stanek (2000) proposed that the bump may be a gravitational microlensing event coincidentally affecting this afterglow. They model the effect of gravitational focusing of light rays by a star halfway between the observer and GRB 000301C (it would be resident in the outskirts of a galaxy near the line of sight) and find that if the emission from the afterglow source is ring-like, a lens of mass $\sim 0.5 M_\odot$ can provide a suitable magnification lightcurve for the optical bands. The microlensing event would be due to the growth of the (unresolved) disk of the expanding shock. As it passes by the lensing source its light is focused; if the edge is bright this produces a single bump. Due to time-delay effects, the emission from an afterglow is expected to be predominantly from the edge of its visible disk (see Granot, Piran & Sari, 1999a,b). Gaudi, Granot & Loeb (2001) also consider this possibility, even inverting the estimated magnifications from the data to determine what surface brightness profile would produce the light curves by being lensed.

Zhang & Mészáros (2001) have also examined the effect of energy injection from a highly magnetized millisecond pulsar on a GRB afterglow (if this were the progenitor source). They find an achromatic bump in flux level will be produced as it spins down, and the required parameters for the spin down to correspond to the 000301C afterglow's feature. Berger *et al.* (2000) did not model the bump feature, but propose that it may be due to the fireball encountering a dense cloud of material, suddenly increasing the density of radiating electrons. Dai & Lu (2002) considered a similar effect in detail, showing that a sudden jump from a low density ($n \sim 1\,\mathrm{cm}^{-3}$ or a Wind-like medium $\sim A_*$) to a high density ($\sim 10^3\,\mathrm{cm}^{-3}$), such as those in a molecular cloud, will produce a very short drop followed by a bump in the light curve, similar to that of 000301C.

The global properties of the event have also been examined under several scenarios. Berger *et al.* (2000) do a broadband model fit from observables (spectral breaks) and have described the decay steepening and late-time fast decay with a jet break at 7.3 days in an ISM-like medium, with a very steep electron energy distribution index $p = 2.70$, giving a steep post-jet evolution; they find jetted Wind-like medium models do not provide as good a fit.

Li & Chevalier (2001b) have found an isotropic Wind-like model that describes the general trends if it has a broken power law in the injected electron energies, of

$$N(\gamma) \propto \gamma^{-p} \ \ (\gamma_m < \gamma < \gamma_M) \ \ \text{and} \quad \propto \gamma^{-q} \ \ (\gamma_M < \gamma) \ .$$

The ratio γ_m/γ_M is constant in their model. They refer to observations of pulsar-wind nebulae, such as the Crab, where similar energy distributions are suggested. They find that a transition from $p = 2.2$ to $q \sim 15$ will provide the observed steepening, which will not affect the radio band as rapidly.

Dai & Lu (2001) proposed a non-relativistic model with energy injection for the optical trends. The afterglow evolves in a dense pulsar nebula and the shock becomes non-relativistic one day after the burst. A magnetized pulsar progenitor injects energy into the shock by magnetic dipole radiation (flattening the afterglow decay) and once it spins down, the decays steepens (requiring $p = 3.4$ for t^{-3}).

Panaitescu (2001) addressed both issues, fitting a numerical model of the shock evolution and emission along with gravitational microlensing effects upon the surface brightness profile produced. He finds that a jetted ISM-like model with a broken power law electron energy distribution provides a reasonable fit, but that microlensing does not describe the optical bump well. For the simplest uniform jet, his calculated surface brightness profiles are not very much like a narrow ring at optical frequencies. He does not rule out microlensing for other types of jetted ejecta. Panaitescu (2001)'s model uses the electron distribution as described for GRB 991216 (much like that of Li & Chevalier, 2001b, above). He finds a reasonable density, collimation, total electron energy fraction, and magnetic energy fraction. A transition from $p \sim 1.3$ to $q \sim 2.4$ with about 1/3 of the electron energy in the "hard" (γ^{-p}) section provides a good fit, requiring the break due to electron energy steepening to pass the optical band around the jet break. The radio, with emission from the hard part of the electron distribution, decays more slowly post-jet.

We analyzed the data set presented by Berger *et al.* (2000). In order to avoid a bias in the fit by the bump, we ignored all data from three to five days post-burst, given the claim of achromaticity. We did not consider it useful to decide upon a likely source for the flux bump and radically change or add to the model used without first determining that the model is a fairly reasonable description of the data's general trends. This leaves us with some data problems. The optical decay $\sim t^{-2.7}$ may be steeper than the radio decay; there are no X-ray observations to verify if this behaviour is universal at high frequencies. The break in the lightcurve occurs just after the bump; the bump may mask some of this evolution and ignoring it may also skew the fit.

We were unable to find a satisfactory fit to this data set. Figure 6.2 presents some of the data, with one of our fits for comparison. The model's density profile is ISM-like, and the parameters are: $E_{iso} \sim 10^{55}$ ergs, $\theta \sim 0.02$ rad, (so $E_{tot} \sim 4 \times 10^{51}$ ergs), $n \sim 2 \times 10^{-5}\,\mathrm{cm}^{-3}$, $A(V) \sim 0.07$, $p \sim 2.6$, $\epsilon_e \sim 0.03$, and $\epsilon_B \sim 0.06$. It has a jet break at 6.7 days. Even ignoring the flux bump, its χ^2 is 209 for 106 data points (99 degrees of freedom). The formal probability that the data is drawn from this model's distribution is $6.4{\times}10^{-12}$ by the χ^2 test. The high χ^2 is symptomatic of the inability of the model to fit both optical and radio data when the radio decay is significantly shallower.

There is more scatter than is reasonable about this fit, in other words more structure than a single bump. The model also has difficulty reproducing the radio peak, overestimating the pre-jet fluxes. The model's post-jet decay is clearly too steep for the radio data; early overestimation allows the model to fit the data at the midpoint of the observations. The basic fireball model is inadequate for this event. The "bump" requires at least an additional effect such as microlensing, and may indicate another model entirely is required. A successful model must produce more rapid decay at high frequencies by comparison to the radio. It is interesting that 000301C may be a Short GRB, if so the only one to date with a detected afterglow, and its afterglow does not fit the basic picture.

010222

This event was detected by the *BeppoSAX* Wide Field Cameras, and an optical counterpart was discovered $\approx$ 4 hours later by two groups, Henden (2001a,b) and McDowell *et al.* (2001). Jha *et al.*

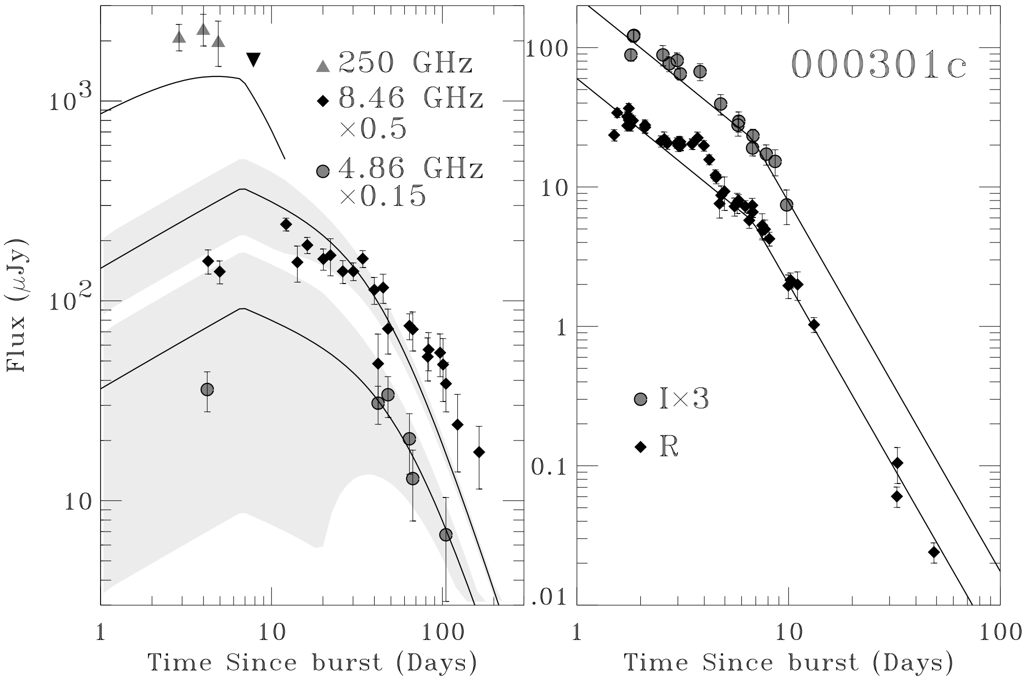

Figure 6.2: Selected radio, submillimeter, and optical bands of the 000301c afterglow; there were no X-ray observations. Our best-fit model (which does not adequately describe the data) is plotted. The grey envelopes show the estimated fractional uncertainty applied to the model's flux based upon the expected degree of interstellar scintillation for an extragalactic source along that line of sight. One submillimeter point that was not detected at the 2σ level is shown as a 2σ upper limit (downward triangle). For clarity the submillimeter model's lightcurve is truncated at twelve days, beyond which there is no data. There is a definite "flux bump" in the optical from approximately 3–5 days, seen in R and I; we ignored all data from 3–5 days in our fit. The sudden drop of the 250 GHz flux has been interpreted by Berger *et al.* (2000) as evidence that the flux bump is achromatic in the broadband. There may be other flux deviations, such as the initial R point with its low flux. While Berger *et al.* (2000) found a fairly reasonable solution by fitting for break frequencies, we are not able to find a satisfactory solution from fundamental parameters. The radio data decays less steeply than the model; the model overestimates the radio peak in order to fit more of the data.

(2001) discovered several absorption-line systems in the afterglow spectra and determined that the event occurred at redshift z=1.477. The event was followed in the radio (Berger & Frail, 2001) and X-ray by both the *BeppoSAX* Narrow Field Instruments (In't Zand *et al.*, 2001) and the *Chandra* X-ray satellite (Harrison, Yost & Kulkarni, 2001) as well. Frail *et al.* (2002)'s observations determined that the associated submillimeter emission was from the host.

The data showed one significant non-standard element, seen in Figure 6.3, a clear break to steeper decay in the optical (e.g., Stanek *et al.*, 2001; Masetti *et al.*, 2001) and X-rays (In't Zand *et al.*, 2001) whose pre- and post-break temporal indices do not fit the picture of the basic fireball model. Another issue is the extinction at the host; Jha *et al.* (2001) and Lee *et al.* (2001) claim that the

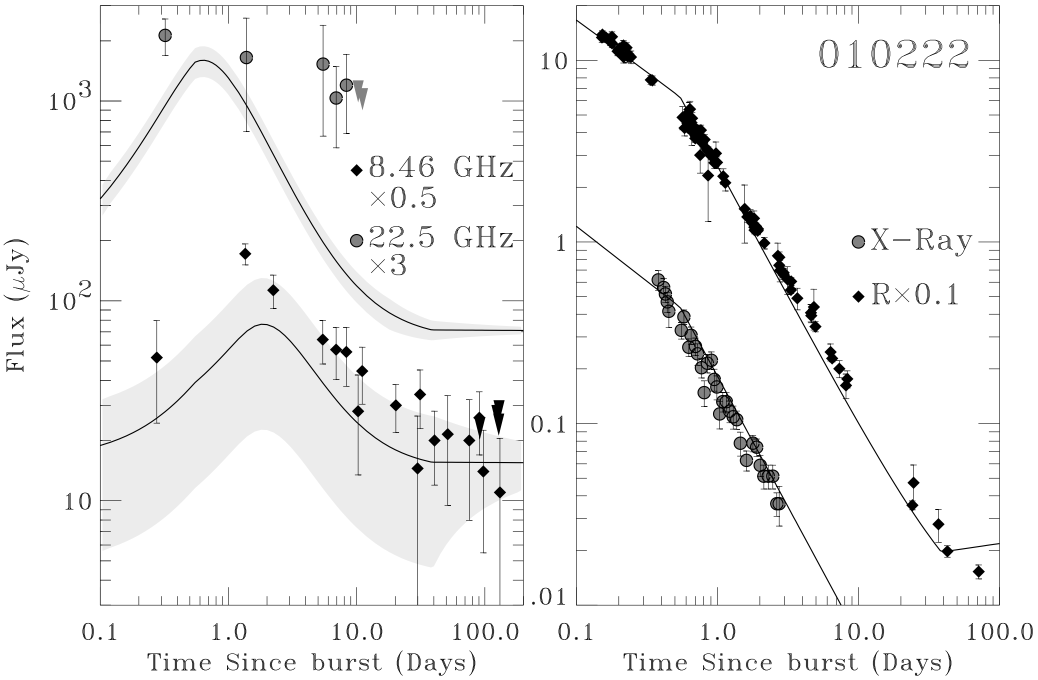

Figure 6.3: Selected radio and optical bands, and the X-ray data of the 010222 afterglow. The solid line shows one of our best (yet unsatisfactory) fits, collimated ejecta in an ISM-like density medium, with a hard ($p < 2$) electron spectrum. The grey envelopes show the estimated model flux uncertainty from interstellar scintillations. Data that are not detected at the 1σ level are shown as 1σ upper limits (downward triangles). The model does not describe the data well. The model's optical decay is too steep. Higher-frequency radio flux (22.5 GHz) does not match the peak passage expected from the 8.46 GHz lightcurve. The X-ray decay does not match the optical break. (The model parameters are: $E_{iso} \sim 3 \times 10^{53}$ ergs, $\theta \sim 0.1$ rad ($E_{tot} \sim 10^{51}$ ergs), $n \sim 20\,\mathrm{cm}^{-3}$, $A(V) \sim 0.1$ mag for an SMC-like extinction, $p \sim 1.33$, $\epsilon_e \sim 0.001$, and $\epsilon_B \sim 0.0004$. It has a jet break at 0.5 days, and a non-relativistic transition at 37 days post-burst. The radio host is assumed to have a $\nu^{-0.3}$ spectrum.)

host may not follow a "standard" extinction law seen locally.

The break at ~ 0.5 days is from $\sim t^{-0.8}$ to $\sim t^{-1.3}$ or $\sim t^{-1.5}$, too large to be due to the passage of the cooling frequency ν_c. This large a break, especially with the probable achromaticity suggested by the X-ray observations, would normally be interpreted as the jet break from seeing the edge of collimated ejecta. However, this would require a very hard electron energy spectrum $N(\gamma) \sim \gamma^{-1.5}$, as post-jet evolution is proportional to t^{-p} at high frequencies (see §3.2). With $p < 2$, there must be a high-energy cutoff to the electron energies, otherwise the total energy would be infinite. The behaviour of the maximum electron Lorentz factor γ_M will then define how much energy goes into the set of electrons. In such a model it is not clear if the spectral behaviour of the fireball emission will resemble the results for $p > 2$.

Bhattacharya (2001) addressed this issue, demonstrating that if $\gamma_M = \xi\gamma_{shock}$ (ξ a constant), this will result in a constant total energy fraction in the electrons and emission behaviour as before, since $\gamma_m \propto \gamma_{shock}$ (see Equation 20 of Bhattacharya, 2001) for $1 < p < 2$. This is not surprising as the key assumption when $p > 2$ was that $\gamma_m \propto \gamma_{shock}$, when γ_m rather than γ_M determined the electron energy.

There are alternate views of the model behaviour where $p < 2$. Bhattacharya (2001) considers a constant energy fraction injected into the electrons, and a maximum Lorentz factor γ_M proportional to a general power law of the shock Lorentz factor. For powers different than 1, the resulting break frequency evolution changes from those where $p > 2$. Dai & Cheng (2001) have considered a substantially different dependence for γ_M, setting its value by allowing the acceleration time to equal the cooling time. Thus γ_M is the cooling break's Lorentz factor, γ_c; as they allow for a constant energy injected below γ_M, the amount of energy in the *uncooled* electrons is constant. Dai & Cheng (2001) find a steep post-jet evolution above the spectral peak, $f_\nu \propto t^{-(p+6)/4}$, no flatter than $t^{-1.75}$ for $p > 1$. Bhattacharya's work (2001) differs as it can result in $\gamma_c \ll \gamma_M$.

Clearly, some physical assumptions must be adopted to analyze the fireball behaviour for $p < 2$. However, a continuing balance between the shock's acceleration and the synchrotron emission's timescales may be perhaps more difficult to maintain than a shock acceleration dependent only upon the shock's Lorentz factor. Bhattacharya's work (2001) when $\gamma_M \propto \gamma_{shock}$ permits an examination of this event using the basic fireball model, even though the data appears to require $p < 2$. If the work's assumptions are correct, the break frequencies would behave in the same fashion as the $p > 2$ case. This result justifies model efforts that simply extend $p > 2$ solutions, from "α, β" (fitted spectral and temporal slopes compared to the model relations) analyses to comprehensive broadband methods. Other solutions for spectral evolution with $p < 2$ have not generally been employed.

Galama *et al.* (2003) fit the optical/NIR data with a broken power law $t^\alpha \nu^\beta$ and fitted host components and extinction law, where α, pre- and post-break, and β are related by p. They find a jet break with $p \approx 1.6$ at time ≈ 0.9 days describes the data well. Panaitescu & Kumar (2002) fit a numerical evaluation of the fireball model to the radio, optical, and X-ray data, with an electron energy distribution allowing a break from a shallow to a steeper energy spectrum rather than a cutoff at high energy. Their best fit is to an ISM-like density with the ejecta collimated to 5° and $p = 1.35$. It is, however, not satisfactory, decaying too steeply in the X-rays with the passage of γ_M.

These are not the only proposed solutions; Masetti *et al.* (2001) found that the fitted α and β are consistent with a rapid deceleration of an isotropic shock and non-relativistic evolution past ~ 1 day, with extinction affecting the optical. More recently, Björnsson *et al.* (2002) argued that the polarization detected is not consistent with an isotropic source, and that a jet model with a normal $p \approx 2.5$, but with energy injection flattening the decay curves, accounts for the observations.

In order to investigate this further, we altered our fitting model slightly to accommodate Bhattacharya (2001)'s description of the emission from a hard electron spectrum ($p < 2$) and $\gamma_M \propto \gamma_{shock}$, with the maximum electron energy's frequency well above any data (so no extra spectral breaks were included).

The accommodation required is a minor change to the equations as expounded in §3.4 (Eqs. 3.4, 3.5). As noted, every time ϵ_e appears, it is in the form given the shorthand $\bar{\epsilon}_e = \epsilon_e(p-2)/(p-1)$; this is a direct result of integrating the electron energy distribution from γ_m to ∞, and giving this ϵ_e of the ejecta (protons') energy. As a result

$$\gamma_m = \epsilon_e \, (\frac{p-2}{p-1}) \, \frac{m_p}{m_e} \, \gamma_{shock} \ ,$$

or simply

$$\gamma_m = \bar{\epsilon}_e \, \frac{m_p}{m_e} \, \gamma_{shock} \ .$$

As for $p < 2$, $\gamma_m \propto \gamma_{shock}$ under the assumptions we adopt, we simply redefine $\bar{\epsilon}_e$. For $p < 2$ it is ***simply a constant of proportionality*** (required to be < 1), and is not related to the total electron energy ϵ_e via p in the manner $p > 2$ prescribes. The proportionality is a function of ϵ_e, p, m_p/m_e, and ξ, the proportionality between the maximum electron Lorentz factor and that of the shock. This forces a degeneracy in ϵ_e and ξ. The parameter ϵ_e only appears independently in corrections to the synchrotron spectrum: the strength of inverse Compton cooling affecting ν_c and the degree of energy corrections to $E(t)$. As the corrections should be small, they do not form a suitable independent constraint. We chose to fit $\bar{\epsilon}_e$, and fix a value for ϵ_e in the Compton and energy corrections. The fixed value can be varied for different fit runs; we select a value reasonable from other model fits, generally 0.1 or 0.3.

Using this model, we analyzed a broadband data set for this event. We took radio observations (1.43, 4.86, 8.46, 10.5, 15, and 22.5 GHz) from the Caltech GRB group (available in the VLA database described by Frail *et al.*, 2003a), and the submillimeter observations of Frail *et al.* (2002), allowing a submillimeter host component. The optical data utilized was principally the *UBVRIK* compiled by Galama *et al.* (2003); we also included the ten flux densities of Jha *et al.* (2001)'s subdivided spectrum (see their Figure 3, the frequencies range roughly from B to I). For the X-ray, we employed the *BeppoSAX* afterglow data of In't Zand *et al.* (2001) and performed our own analysis of the *Chandra* data products for this observation, fitting the counts spectrum to an absorbed power law and decomposing the energy range into a hard (characteristic frequency $\approx 1.2 \times 10^{18}$ Hz, as for the *SAX* data) and soft ($\approx 1.2 \times 10^{17}$ Hz) bands.

The data's optical/NIR and X-ray spectral and temporal power law indices are related in a manner reasonably matched by the relations for a jet break with $p \approx 1.5$. Nevertheless, we were unable to find a satisfactory model with the spectrum evolving from fundamental physical parameters. We noted a second non-standard element in the data: the low-frequency radio flux has a rapid peak passage at approximately one day post-burst (see Figure 6.3); higher frequencies remain flat (or are decaying slowly). This is difficult to accommodate, much like the early radio decay in the 991216 data set. The only reasonable fits ($\chi^2 \approx$ DOF) had a jet break at ≈ 0.4 days, and $p \approx 1.5$, but unphysically high magnetic energy fractions $\epsilon_B \approx 150$, over two orders of magnitude above the physical limit.

Restricting ϵ_B to be less than 1.0 produced very poor fits, typically with the low frequencies such as the radio becoming under-predicted, with the peak passing too early or too low. (Also, our sharp jet break did not fit the X-ray data well when $t_{jet} \approx 1$ day.) One such attempt can be seen in Figure 6.3. The model clearly does not describe the data.

We attempted to employ models with higher energy and/or density values to counteract the lower peak resulting from the lower magnetic energy fraction, but none were successful. The high frequency (above the cooling frequency) flux is expected to have a slight dependence on the magnetic energy fraction, none on the density and a strong dependence on energy; low frequency flux may have a strong dependence on all three. It is likely that increasing the energy increased the high frequency fluxes out of proportion and increasing the density produces an unacceptably high self-absorption frequency. Some of these poor models resulted in jet breaks at times much greater than one day. We also attempted similar fits while forcing the jet break to be around Day 1 (by adding a penalty to the fit statistic for a far different jet break), with no good result.

No satisfactory result with a good fit and reasonable model parameters could be found with the simple model, even stretching the model to allow $p < 2$. We concur with other researchers that the basic fireball model is inadequate to describe this event.

6.2 Cases where Data Are Insufficient

Some GRB events have little afterglow data, due to a late discovery, adverse weather, or even being overshadowed by other events whose followup is ongoing. Those with only a few points are not suited to a full broadband model fit; they will not provide sufficient constraints. There are also cases between the extremes of “a few points verifying a decaying afterglow” and densely-sampled multiband radio and optical light curves, with X-ray observations to boot. These may be suitable to constrain the full model, but any oddities in the data will be difficult to put into perspective.

Two events where data is not as fully sampled as the cases in Chapter 4 are GRB 991208 and GRB 000418. These both exhibit some scatter or deviation about a best fit with the simple model. Moreover, no X-ray data exist for either event. These are not as useful as the 970508 event, which showed scatter, as that event was densely sampled in optical and radio frequencies and had some observations in the X-ray. For these cases the highest observable frequencies cannot be checked for consistency with the lower ones. There can be no check against the estimated inverse Compton upscattered flux component (or lack thereof) required by certain parameters (high densities, and

$\epsilon_e > \epsilon_B$). This section also includes GRB 990510, whose data set contains X-ray observations. However, the data does not uniquely constrain our model. Our results depend upon the treatment of scintillation uncertainties. The modelling efforts for these events are presented below.

991208

This event was detected by the IPN and its position was disseminated approximately two days post-burst (Hurley *et al.*, 2000a). The event was followed up by radio and optical observers, yielding independent afterglow detections in the radio (Frail *et al.*, 1999) and the optical (Castro-Tirado *et al.*, 1999). Djorgovski *et al.* (1999b) determined the redshift, z=0.707.

We assembled a data set of 79 points, distributed among the optical ($BVRI$ of Castro-Tirado *et al.*, 2001), submillimeter (86.24, 100, and 250 GHz), and extensive radio (1.43, 4.86, 8.46, 15, 22.5, and 30 GHz) bands (Galama *et al.*, 2000). The optical data was de-reddened for Galactic extinction, and showed evidence of underlying host flux. There was no evidence for a submillimeter or radio host flux contribution. We applied a nominal 1% extra uncertainty to the data for flux calibration. We fit this data set by the method described in Chapter 3. We found a reasonable fit with the following parameters: $E_{iso} \approx 3 \times 10^{54}\,\mathrm{ergs}$, $\theta \approx 0.024$ rad ($E_{tot} \approx 9 \times 10^{50}\,\mathrm{ergs}$), $n \approx 0.3\,\mathrm{cm}^{-3}$, $A(V) \approx 0.3\,\mathrm{mag}$, $p \approx 2.42$, $\epsilon_e \approx 0.1$, and $\epsilon_B \approx 0.03$. The jet break is at 0.1 days. The character of this fit model is shown in Figure 6.4.

The model fit's χ^2 is 136 for 68 degrees of freedom. This includes the interstellar scintillation estimates. By the χ^2 test, the probability the data is drawn from the model's distribution is merely 2×10^{-7} (excluded at approximately the $5\,\sigma$ level). The high χ^2 is a symptom of problems with the fit elaborated below.

There is no single frequency band that causes this poor fit. In the radio, the 1.43 GHz band contributes 2.6 to the χ^2 for each data point, but the 4.86 and 8.46 GHz bands contribute only 0.3 and 1.6 per point, respectively. The optical bands contribute from 1.3 to 2.7 per point, and the submillimeter from 0.5 to 3.9 per point.

Some deviations from the fit model's trends are not systematic. There is insufficient sampling to determine whether those in the optical (such as the R points at 20–40 days post-burst in Figure

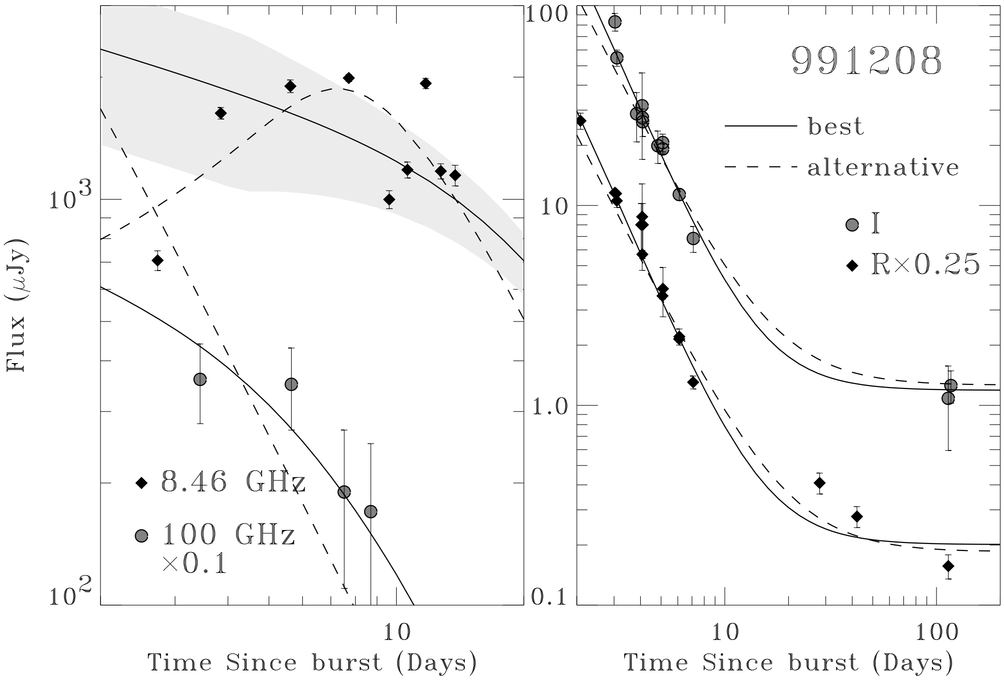

Figure 6.4: Selected radio (8.46 GHz), submillimeter (100 GHz), and optical bands of the 991208 afterglow, with our fit attempts. The solid line depicts the best broadband fit, which has a χ^2 of 136 for 68 degrees of freedom and does not properly predict the radio peak. The dashed line shows an alternative fit giving a later radio peak due to high self-absorption. The radio's estimated model uncertainty from interstellar scintillation is indicated by the shaded region surrounding the best model; it is the same fractional uncertainty in both fits. Both model fits have reasonable parameters and ISM-like density profiles. The data shows a rapid optical decline, demanding a jet break before the data; this is not compatible with a rising radio flux, unless the radio is self-absorbed and in fast-cooling (or with $\nu_a > \nu_m$). This incompatibility may indicate a deficiency in the model (or its assumptions) but the event has too little data to distinguish between modelling scenarios.

6.4) are the result of rapid fluctuations in the flux, rather than miscalibrations of the data.

The main difficulty lies in reconciling the optical and radio data sets. The optical is decaying quickly, as $\sim t^{-2}$, and this requires a collimated model. The jet break is not seen but is placed before the first observations (the observations did not begin until a few days post-GRB, after the times at which some jet breaks are observed in other afterglows). Nevertheless, the radio flux is rising, which only occurs in the basic model when the frequency is below self-absorption and the shock is in the fast cooling regime ($\nu_c < \nu_m$). The model over-predicts the radio. It is not a good fit that describes that data, despite the reasonable χ^2 per point in that frequency region.

By eliminating the scintillation efficiency component in the model uncertainties used to calculate the fit statistic, another fit model was found, with somewhat different parameters ($E_{iso} \approx 2 \times$

10^{55} ergs, $\theta \approx 0.018$ rad [$E_{tot} \approx 3 \times 10^{51}$ ergs], $n \approx 0.9\,\mathrm{cm}^{-3}$, $A(V) \approx 0.1\,\mathrm{mag}$, $p \approx 2.07$, $\epsilon_e \approx 0.03$, and $\epsilon_B \approx 0.02$, with a jet break at 0.06 days). This model produces an early rise in the radio from a much higher self-absorption; it is above the radio frequencies initially and the minimum injected electron energy break ν_m is below it, so ν_a gives the spectral peak and the radio rises until it passes. These peaks are not well-matched to the data nor is the decay at higher (submillimeter and above) frequencies. The peak may be a bit low and this initially under-predicts some of the optical data slightly.

This event contains too little data to definitively distinguish between such disparate scenarios. It is cautionary that a reasonably large data set, at least when it is not decisively well-fit, can be marginally fit by quite different spectral models.

000418

This event was detected by the Interplanetary Network (Hurley, Cline & Mazets, 2000) and subsequently followed up by radio and optical observers. Klose *et al.* (2000) detected the afterglow in the near-infrared K' band; Bloom *et al.* (2000) determined its redshift, z=1.118.

We assembled a data set of 71 points from the work of Berger *et al.* (2001a), who present optical and radio data as well as compiling optical data from the literature. The radio data includes 49 points distributed among frequencies of 1.43, 4.86, 8.46, 15, and 22.46 GHz. In the optical-NIR range, we select only the 22 points in the R and K' bands for use, ignoring other wavelengths where there is insufficient sampling (merely one point) to determine the contribution from host flux. Berger *et al.* (2001a) note than the R data show that the host is bright enough to dominate optical observations after one week; the data in bands without a host flux constraint were taken later than ten days post-burst and do not provide a reliable measure of the afterglow. We treat the K' and K bands as identical as they differ by approximately $0.2(H-K)$ magnitudes (Wainscoat & Cowie, 1992). An $H-K$ colour of more than one magnitude would be very red (the entire $R-K$ colour of the afterglow is approximately three magnitudes, and H is "next" to K); with data uncertainties of 0.2 to 0.5 magnitudes the $K'-K$ differences are treated as negligible. The data do not show any evidence of a jet break or a cascade in peak flux values (although, as the peak is only visible at 4.86

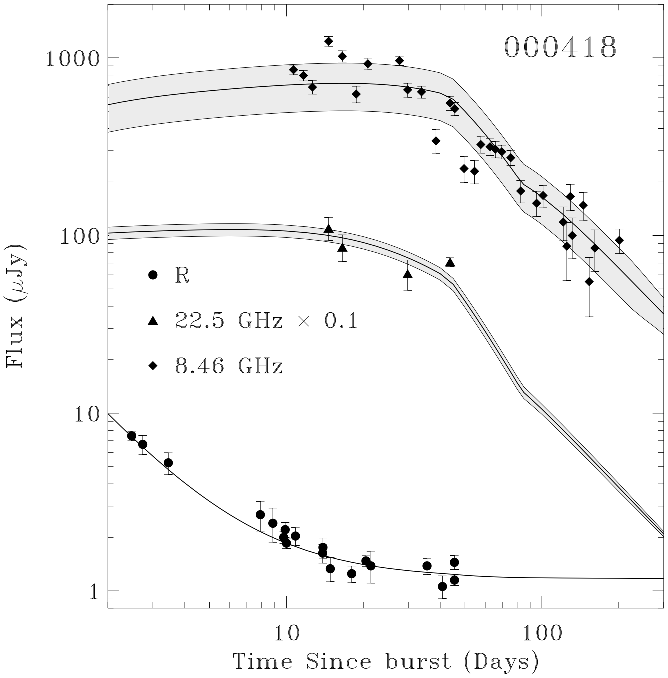

Figure 6.5: Selected radio/optical bands of the 000418 afterglow, with our best fit, a wide jet in an ISM-like density profile. It is formally a poor fit (χ^2=123 for 58 degrees of freedom), and has extreme radiative corrections (ϵ_e=0.7). There is scatter in the radio above the degree expected from interstellar scintillation estimates, and there are some issues with the data consistency in the optical (note the large scatter past two weeks). The lack of X-ray data and of radio data at less than ten days post-burst, combined with the optical data's reduced usefulness due to the bright host, causes this data set to be insufficient to completely resolve the modelling issues.

and 8.46 GHz, this is not a strong constraint).

Berger *et al.* (2001a) could not provide a good fit with an isotropic model. They produced a reasonable fit with either an ISM-like or Wind-like circumburst medium and a jet break after $\approx 2-4$ weeks, masked in the optical by the host. There is no visible cascade of peak flux values. However, when the fit matches the peak flux value during its passage through the radio, the optical flux estimates will be too high if the peak frequency and flux values are extrapolated back employing an ISM-like isotropic evolution (with no peak flux cascade).

We performed fits, finding a best result for an ISM-like density with χ^2 of 123 for 58 degrees of freedom. The character of the fit is shown in Figure 6.5. It is a somewhat poor match to the data, with a low radio peak. This is further seen in the χ^2 test: the probability the data is drawn from the model's distribution is 1×10^{-7} (excluded at approximately the $5\,\sigma$ level). The model parameters are: $E_{iso} \approx 5 \times 10^{52}\,\mathrm{ergs}$, $\theta \approx 0.64\,\mathrm{rad}$, $n \approx 5\,\mathrm{cm}^{-3}$, $A(V) \approx 0.6\,\mathrm{mag}$, $p \approx 2.13$, $\epsilon_e \approx 0.7$, and $\epsilon_B \approx 0.01$. The jet break is at 43 days post-burst. The substantial density causes a fairly rapid deceleration; the non-relativistic transition is at 84 days post-burst.

The electron energy fraction, ϵ_e, and consequently the estimated radiative corrections, are rather extreme. A poorer Wind-like model was the best fit with a smaller $\epsilon_e \approx 0.3$. (The Wind-like fits may not be as good as they take longer to reach a non-relativistic transition, and the radio decay is not extremely steep.) For this reason the fit is questionable.

The optical (R and K) provide good fits. It is the radio that has excessive deviations from the model (8.46 GHz adds on average 2.4 to the χ^2 for each point). The model is somewhat too flat around ten days post-burst. Instead of rising out of self-absorption, the flux level is seriously attenuated by the radiative losses. The peak is also too low there, as seen in Figure 6.5. We consider the fit to be poor, insufficiently constrained by a paucity of high-frequency data, with a low radio peak and an extreme ϵ_e requirement, which strains the radiative corrections model.

Without a more constraining data set it is not a simple matter to extract information from this event. We have a best fit with extreme radiative corrections, a significant ISM-like density and a substantial host extinction. Berger *et al.* (2001a) find a best fit with either (1) a Wind-like density environment produced by a small outflow, a low ϵ_e, and an extremely high ϵ_B or (2) a low ISM-like density, small ϵ_e, and small ϵ_B. Panaitescu & Kumar (2002) find a good fit in a Wind-like environment with a substantial outflow $\sim 0.7A_*$, and small ϵ_e and ϵ_B. The only commonalities are that the models are collimated, but widely, and a subtantial extinction at the host.

990510: A Marginal Case

This event was detected by the *BeppoSAX* Wide Field Cameras, permitting optical searches for the counterpart. Vreeswijk *et al.* (1999b) discovered the optical afterglow in the B and R bands by comparison to archival images. The fading X-ray afterglow was also identified (Piro, 1999). Vreeswijk *et al.* (1999c) identified the redshift as z=1.619 based upon its absorption-line spectrum. The afterglow was followed in the optical, X-ray, and radio.

This event was the first where a strong break to faster decay was observed and interpreted as evidence for collimated ejecta. Both Stanek *et al.* (1999) and Holland *et al.* (2000) reported a

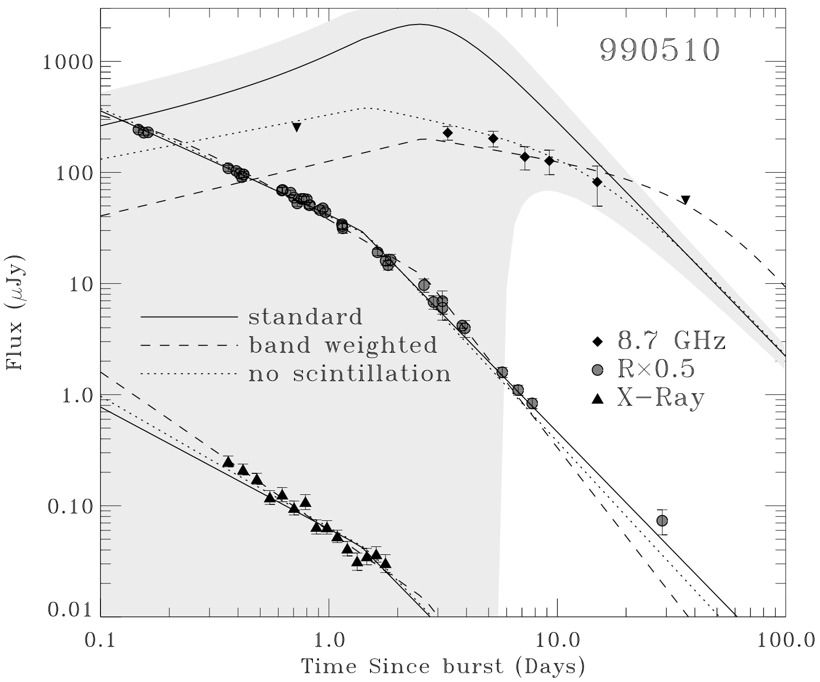

Figure 6.6: Selected radio and optical bands, and the X-ray data of the 990510 afterglow. Three models, the best fits under slightly different fit statistics, are shown. The solid line gives the best fit under the standard method from Chapter 3, where interstellar scintillation is accounted for by applying extra uncertainty (grey envelope) based upon estimated scintillation efficiencies. The fit statistic ($-ln$(Probability), §3.5) disfavours excessive model radio flux to get higher model uncertainties; the fit nevertheless strongly overestimates the radio data. The dashed line shows the fit where each *wavelength region* (radio, optical, and X-ray) is weighted equally in a pseudo-χ^2 fit statistic (the same fractional scintillations were applied in this case, but are less important in the fit). The dotted line shows a fit as in the standard case, but where interstellar scintillation was not accounted for in any way. The latter two models provide far better fits in the radio, but are too steep for the late-time optical data. None of the fits is completely adequate, and the three different results with slight changes to the fit process show how "fragile" a fit model can be when it does not clearly fit all the data.

steepening from $\sim t^{-1}$ to $\sim t^{-2}$, achromatic in the optical bands, and too large a change to be the passage of the cooling break; this was interpreted as evidence for a jet break (see Figure 6.6).

Harrison *et al.* (1999) performed a broadband radio and optical analysis. They reported an optical decay steepening from $t^{-0.82}$ to $t^{-2.18}$ near Day 1, deriving from the spectral and temporal power laws (an α, β analysis) that this was consistent with a jet break if $\nu_m < \nu$(optical)$< \nu_c$ and $p \approx 2.1$. They further calculated the position and height of the spectral peak from simultaneous optical and radio observations (assuming for the spectral shape that the radio emission was in the optically thin regime, proportional to $\nu^{1/3}$). This determined that the radio behaviour after the optical break is compatible with the expected post-jet gradual decay before the peak passes the wavelength band, and not with the expected continued growth in an isotropic model.

Covino *et al.* (1999) and Wijers *et al.* (1999) detected polarization in the optical afterglow, at a level $\sim 2\%$. Each demonstrates that it is not due to polarization from Galactic dust, by comparison with the polarizations of field stars. It is unlikely to be due to dust in the host environment, as this would be expected to occur from light scatters that would appear later as a dust "echo". This is further evidence for collimation, since the polarization of light from an unresolved isotropic shock would average out. Observing a collimated jet slightly off-center permits a non-zero average polarization (see Sari, 1999; Ghisellini & Lazzati, 1999).

Kuulkers *et al.* (2000) demonstrated that the *SAX* afterglow observations, taken over a shorter time domain than the optical data, are consistent with either a single power law decay or a gradual steepening mirroring the optical break. Pian *et al.* (2001) strengthened the X-ray case for collimation, showing that the extrapolation of the X-ray afterglow as a single decay is too steep to be compatible with observations at the end of the prompt emission. The X-ray afterglow likely steepened from an initially slower decay.

Panaitescu & Kumar (2001b) find a reasonable fit from fundamental parameters to radio, optical and X-ray data with jet model in an ISM-like medium (they infer that the optical slope is not consistent with a Wind-like medium's $t^{\alpha(p)}\nu^{\beta(p)}$ requirements). Their result has a small density $n \approx 0.14\,\mathrm{cm}^{-3}$, substantial collimation $\theta \approx 3^\circ$ and $p = 2.01$.

Based upon others' success, we undertook a full broadband analysis of the data set with our model. We took the X-ray data of Kuulkers *et al.* (2000), the optical ($UBVRI$ bands) data of Stanek *et al.* (1999) as well as that presented and compiled by Harrison *et al.* (1999). The radio data (4.8 and 8.6 GHz) were taken from Harrison *et al.* (1999). For Galactic de-reddening, we adopt $E(B-V)$=0.20 from the Schlegel, Finkbeiner & Davis (1998) dust maps, as in Harrison *et al.* (1999). We allowed a cross-calibration uncertainty of 5%, and did not fit any host components as there is no evidence for late-time flattening out to a month post-burst, when the R flux $\approx 0.1\ \mu$Jy.

Using our standard method described in Chapter 3, we were not able to find a satisfactory model. The fit statistic, $-ln(P)$ (P the fit probability), aims to avoid situations where the radio flux is consistently overestimated in the model, with the uncertainty introduced by scintillation (as a fraction of the model flux) becoming large to accommodate the data (§3.5). In this case, the model is not well-fit and the best fits do indeed over-predict the radio. The best fit by our standard method has a χ^2 of 236 for 158 degrees of freedom; by the χ^2 test, the probability that the data is taken from this model's distribution is 2.5×10^{-5} (excluded at approximately $4\,\sigma$). The character of this fit, which is fairly reasonable at frequencies above the radio, is shown in Figure 6.6. Its parameters are: $E_{iso} \sim 10^{55}\,$ergs, $\theta \sim 0.04$ rad (so $E_{tot} \sim 7 \times 10^{51}\,$ergs), $n \sim 0.02\,\mathrm{cm}^{-3}$, with no required host extinction, $p \sim 2.007$, $\epsilon_e \sim 0.07$, and $\epsilon_B \sim 0.07$. It has a jet break at 1.4 days.

This result is due to a poor overall fit; the fit becomes sensitive to changes such as scintillation efficiencies when there is no good description of the overall trends in the data, under the constraints of the model. In addition, the low value of p approaches the infinite-energy limit.

We performed fits that eliminate the scintillation efficiencies, finding a far better fit to the trends in the data, as shown in Figure 6.6. The fit parameters differ somewhat (but are broadly similar in the sense of high energy, low density and moderate electron and magnetic energy fractions): $E_{iso} \sim 6 \times 10^{53}\,$ergs, $\theta \sim 0.05$ rad (so $E_{tot} \sim 8 \times 10^{50}\,$ergs), $n \sim 0.01\,\mathrm{cm}^{-3}$, with no required host extinction, $p \sim 2.13$, $\epsilon_e \sim 0.1$, and $\epsilon_B \sim 0.07$. The fit has a jet break at 1.5 days. The χ^2 is 329 for 158 degrees of freedom. The high χ^2 is expected as there are factors in the data (flux scintillations) that are not accounted for.

We also performed fits with the estimated scintillation efficiencies, but to a weighted "pseudo-χ^2", where each wavelength region: the radio-submillimeter, the optical-NIR, and the X-ray, are given equal weight. (E.g., if there were one X-ray measurement and ten radio points, $\Delta\chi^2 = 1$ from the X-ray point would change the fit statistic as much as $\Delta\chi^2 = 10$ from a point in the radio data set.) This provides a third fit, which is also a fairly reasonable description of the data, albeit the late-time decay is somewhat too steep for the optical. (This fit is also shown in Figure 6.6.) The fit parameters are: $E_{iso} \sim 6 \times 10^{54}\,$ergs, $\theta \sim 0.03$ rad (so $E_{tot} \sim 10^{51}\,$ergs), $n \sim 2 \times 10^{-4}\,\mathrm{cm}^{-3}$, with no required host extinction, $p \sim 2.65$, $\epsilon_e \sim 0.08$, and $\epsilon_B \sim 0.04$. The model has a jet break at 2.6 days, and a χ^2 is 309 for 158 degrees of freedom (excluded at $\approx 7.5\sigma$). The χ^2 test is *not* appropriate for the pseudo-χ^2 statistic, but it is 173.3 and there is $\approx 20\%$ probability that data drawn from a distribution would give a χ^2 of 173.3 for 158 degrees of freedom. Therefore the fit adjusts reasonably well, given the extra weights.

The relatively large χ^2 under the various weighting schemes is merely a symptom of the model fit difficulties for each case. The 990510 fit is not robust—changes to the band weighting or assumed scintillation efficiencies significantly change the character of the fit. The peak height or the parameters change greatly. A reasonable fit requires refinements of the weights given to data points. This ambiguity in the fit contrasts with the case of GRB 970508, in which we considered alternate weights, but they did not change the character of the fit (see §4.3.2). With this ambiguity, the event is a marginal fit that we do not consider with those of Chapter 4. The ambiguous fit demonstrates that there are definite uncertainties in the fitting process, and it is not robust even in cases where the data appears to be fairly good, with radio, optical and X-ray observations, and no obvious data events not covered by the basic model, such as bumps or "$p < 2$" decays.

6.3 Fit Robustness—A Serious Consideration

From these events we infer that the fireball model may be insufficient, or at least not robust, in many events. This is especially seen in 990510 and 010222; the data appears to be sufficient to provide model constraints and its behaviour appears to match model expectations. Yet good fits were not possible.

Even in cases where the model does fit well, we now note the need for caution in adopting a model. If the basic fireball model is inadequate in a fair number of cases, there is the question of whether the basic model is the proper, full description of the underlying process even when it fits the data well. There are several extensions to the basic model that have been proposed to improve (or allow) fits: a break in the electron energy distribution function and energy injection are just two of the examples above.

The four good cases from Chapter 4 could fit the basic fireball model well by mere chance, if there is a large degree of allowable model assumptions that do not greatly affect the fit between model and data. The good fits are not evidence that the basic model has the correct assumptions for those events without quantifying the uncertainty inherent in the model itself.

Even if changes to a model assumption could greatly affect the evolution of the modelled fireball emission, this does not indicate that the basic assumptions are well-constrained in the cases with good fits. Data is sampled only over limited time and frequency ranges. Observed frequencies are typically clustered in three areas (radio, optical, and X-ray), separated by many decades in frequency. Thus only a small part of the broadband spectrum is recorded. Significant changes to the emission are possible when they are not strongly evident over the observed regions. There may be a great deal of degeneracy in the model assumptions that fit the limited data we observe.

We now devote efforts to understanding this uncertainty in the model (given available data). We focus on two areas, the magnetic energy, which is poorly understood from first principles, and the density profile, expected to be more complicated than the simple ISM-like profile, or Wind-like profile in star-forming regions (which are a reasonable progenitor environment).

Chapter 7

Magnetic Energy Fraction as $f(\gamma_{shock})$

In previous chapters we presented good fits to well-sampled afterglow events employing the simple assumptions of the basic model of Chapter 3 (§3.1). We also presented several events where the basic model appears insufficient to account for the data. The basic model assumptions may be incorrect in at least some cases. Without quantifying the uncertainty in model assumptions, it is not clear if the existence of good fits says anything about the simplicity of the underlying physical processes or the environment in those cases. This and the following chapter investigate the range of allowed modifications to a limited set of fireball model assumptions, and whether modified assumptions substantially change the parameters that produce good fits. Here we examine the effects of changing the behaviour of the magnetic energy fraction ϵ_B. The following discussion is taken largely from our work presented in Yost *et al.* (2003).

The behaviour of the magnetic fields is clearly one of the important questions surrounding the microphysics of relativistic shocks. The strength of the magnetic fields implied in the fireball model are far stronger than the levels expected from the strength of the Galactic fields. The relativistic shock would have to amplify the nearby fields (e.g., Medvedev & Loeb, 1999). This would be a nonlinear process acting on small instabilities; the resulting fields would depend on the amplification mechanism and not on the initial values. The large spread in the fitted magnetic energy fraction values ϵ_B (by a factor of more than 100) would then imply highly diverse microphysics amongst relativistic shocks.

This aspect of relativistic shock physics is not fully understood—it is not known from first principles whether the fields pile up, decay away or reach a steady state (see the review by Kirk & Duffy, 1999, and references therein). GRB afterglow emission can be used to investigate this process; Rossi & Rees (2003) show that spectra will differ if the magnetic field is confined to a small length behind the shock. The importance of magnetic fields in GRBs is further demonstrated by Coburn & Boggs (2003)'s recent detection of linear polarization at the theoretical maximum in the prompt emission of GRB 021206. This would require a uniform magnetic field across the γ-ray emission region beamed to the observer, potentially implying that magnetic fields dominate the dynamics (Lyutikov, Pariev & Blandford, 2003).

The assumption that the magnetic energy fraction ϵ_B imparted by the shock amplification is constant is the simplest assumption. Shock physics could depend on the Mach number, or equivalently the Lorentz factor if the shock is relativistic. We therefore want to learn whether the assumption of constant magnetic energy fraction is required, or whether it is possible for the field strength to evolve with the strength of the shock in the afterglow phase. Whether the data truly constrain the interesting diversity seen in the best fit constant values of ϵ_B is also a valuable clue to relativistic shock physics.

With an evolving ϵ_B, the shock would have efficiency varying with time, and the fitted ϵ_B would be simply some weighted average over time. The weighting would depend upon where ϵ_B has the strongest effect upon observable data. It would be possible to effectively get an increase or decrease in ϵ_B if the pileup of magnetic fields behind the shock, in the place where the electrons are accelerated and radiate, does not reach a steady state. If the fields remain and grow it would increase, and if they diffuse away faster than they are replenished it would decrease. It is also possible that the pileup could be position-dependent, even if there is a universal behaviour for a collimated flow, and some of the interesting diversity in the fitted values of ϵ_B could be due to the unaccounted-for differences in viewing angle. To get some constraint on whether these possibilities are allowed by the data, we explore whether an evolving ϵ_B can still produce good fits.

It is important to constrain whether the data *allows* a variable ϵ_B to see if such explanations are

Table 7.1: Spectral parameters' dependences with $\epsilon_B \propto \gamma^x$

	Energy	density	ϵ_e	ϵ_B	t, $t < t_{jet}$	t, $t > t_{jet}$
F_{max}	E	$n^{0.5}$	ϵ_e^0	$\epsilon_B^{0.5}$	$t^0\ t^{-0.19x}$	$t^{-1}\ t^{-0.25x}$
${\nu_a}^a$	$E^{0.2}$	$n^{0.6}$	ϵ_e^{-1}	$\epsilon_B^{0.2}$	$t^0\ t^{-0.08x}$	$t^{-0.2}\ t^{-0.1x}$
ν_m	$E^{0.5}$	n^0	ϵ_e^2	$\epsilon_B^{0.5}$	$t^{-1.5}\ t^{-0.19x}$	$t^{-2}\ t^{-0.25x}$
ν_c	$E^{-0.5}$	n^{-1}	ϵ_e^0	$\epsilon_B^{-1.5}$	$t^{-0.5}\ t^{0.56x}$	$t^0\ t^{0.75x}$

[a] For the order $\nu_a < \nu_m < \nu_c$. When $\nu_c < \nu_m$, multiply by $(\nu_m/\nu_c)^{1/2}$

viable, and its spread in fitted values could be due to model uncertainty. If the ϵ_B disparities could be resolved with a universal varying ϵ_B behaviour that would be of significant interest. Moreover, if ϵ_B's behaviour is not constant, the values fitted with the simple constant assumption could be different from the real magnetic fraction, and the level of this effect should be checked. If only a growing ϵ_B (pileup of field energy as the shock strength drops) or a falling ϵ_B (drop in the field energy as the shock strength drops) are allowed by the data, this would be a clue to the unknown details of relativistic shock's field amplification. To see what the data permit, we studied a simple parameterization of ϵ_B with the shock's γ.

We took the equations for the model as presented in §3.1 and allowed the fixed magnetic energy fraction to vary smoothly. A value for the parameter is calculated at each time and inserted into the equations governing the spectrum at that time. Under assumptions where ϵ_B grows we do not permit it to get infinitely large, capping it at 100%. Any change in the magnetic energy fraction is expected to come from the evolution of the shock, and thus the simplest physically motivated form is to tie it to the shock strength, as expressed by its Lorentz factor γ. For simplicity, we considered $\epsilon_B \propto \gamma^x$, where the basic model (§3.1) has $x = 0$.

This affects the results in two ways, directly and indirectly. There is an explicit dependence upon ϵ_B in the spectral breaks (Sari, Piran & Narayan, 1998) whose evolution changes (Table 7.1). Indirectly, as the cooling frequency affects the energy losses as described in §3.4, we also recalculate $E(t)$, which affects the dynamics.[1]

---

[1] Note that for $x < -4/3$, synchrotron-only theory used for E(t) predicts a decreasing ratio ν_c/ν_m requiring us to change the function $E(t)$. This would indicate a transition to fast cooling ($\nu_c < \nu_m$ and maximal radiative losses) rather than a transition to slow cooling ($\nu_c > \nu_m$ and energy losses subside). Only after the non-relativistic transition, with constant ϵ_B, would the ratio decrease, resulting in an eventual transition to slow cooling.

In practice this is not the case in models of interest with ϵ_B rising over the data range (so $\epsilon_B < 1$); ϵ_e is found in practice to be large enough that $\epsilon_e > \epsilon_B$ (over at least most of the data range). IC cooling dominates so ν_c is multiplied

Table 7.2: Model flux dependences with $\epsilon_B \sim \gamma^x$

Spectral Region	Parameters	t, $t < t_{jet}$ [a]	t, $t > t_{jet}$ [a]
For $\nu_a < \nu_m < \nu_c$			
$\nu < \nu_a$	$E^{0.5} n^{-0.5} \epsilon_e \epsilon_B^0$	$t^{0.5}\ t^{0x}$	$t^0\ t^{0x}$
$\nu_a < \nu < \nu_m$	$E^{0.83} n^{0.5} \epsilon_e^{-0.67} \epsilon_B^{0.33}$	$t^{0.5}\ t^{-0.13x}$	$t^{-0.33}\ t^{-0.17x}$
$\nu_m < \nu < \nu_c$	$E^{1.35} n^{0.5} \epsilon_e^{1.4} \epsilon_B^{0.85}$	$t^{-1.05}\ t^{-0.32x}$	$t^{-2.4}\ t^{-0.43x}$
$\nu_c < \nu$ [b]	$E^{1.1} n^0 \epsilon_e^{1.4} \epsilon_B^{0.1}$	$t^{-1.3}\ t^{-0.04x}$	$t^{-2.4}\ t^{-0.05x}$
For $\nu_a < \nu_c < \nu_m$			
$\nu < \nu_a$ [b]	$E^0 n^{-1} \epsilon_e^0 \epsilon_B^{-1}$	$t^1\ t^{0.38x}$	$t^1\ t^{0.5x}$
$\nu_a < \nu < \nu_c$ [b]	$E^{1.17} n^{0.83} \epsilon_e^0 \epsilon_B$	$t^{0.17}\ t^{-0.38x}$	$t^{-1}\ t^{-0.5x}$
$\nu_c < \nu < \nu_m$ [b]	$E^{0.75} n^0 \epsilon_e^0 \epsilon_B^{-0.25}$	$t^{-0.25}\ t^{0.09x}$	$t^{-1}\ t^{0.13x}$
$\nu_m < \nu$ [b]	$E^{1.1} n^0 \epsilon_e^{1.4} \epsilon_B^{0.1}$	$t^{-1.3}\ t^{-0.04x}$	$t^{-2.4}\ t^{-0.05x}$

[a] p=2.4 is assumed where necessary

[b] for synchrotron cooling dominating; ν_c behaviour changes for IC-dominant cooling, see §3.4 for details

We examined model assumptions of several indices x, $x = 2$, 1, 0, -1, -2, and -3. We did not allow the index to vary, but instead fixed it at integer values. Changes in the model's behaviour (i.e. rates of change in the output light curves or spectral break frequencies) are not highly sensitive to the index. For a typical time span of a factor of 100, γ changes by $\approx$1/6–1/10, and the change in ϵ_B for $x = 1$ alters the magnetic field by only a factor $\approx$2.4. Table 7.2 gives the expected behaviour of the synchrotron flux for $x \neq 0$; these changes are not large for $\delta x \ll 1$.

We thoroughly searched for the best fit models at the values of x considered. Our methods included stepping x in very small steps (between 0.05 and 0.2, depending upon the ease with which the fitting would adjust for a data set), allowing small, smooth changes. We tried larger steps δx ($\sim$ 0.1 where 0.05 would work smoothly, and $\sim$ 0.25 or 1 where 0.2 would work for small steps), forcing the gradient search algorithm to look farther afield for a good fit. We also fit from grids of selected parameter starting points at a particular (integer) x. These grids included values comparable to those at the best fit for the x next-nearest to 0, the basic model's values and typically went up &

---

by a factor $(1+Y)^{-2} \approx Y^{-2}$ (Y, the ratio of IC and synchrotron luminosities, $\approx (\max[(\gamma_c/\gamma_m)^{2-p}, 1]\epsilon_e/\epsilon_B)^{1/2}$) (Sari & Esin, 2001). The effect is $\approx \nu_c^{synch} \times \epsilon_B/\epsilon_e$.

The result is then that $\nu_c/\nu_m \propto E^{-1-x/8} t^{1+3x/8}$ for $t < t_{jet}$. For $E \propto t^{-S}$, $S < 9/13$ (Cohen, Piran & Sari, 1998), this is $t^{(1+S)+x(3/8+S/8)}$. For even a moderate energy loss slope $S = 0.2$, the ratio is increasing for x as small as -3. For the maximal $S = 9/13$, the ratio increases almost to $x = -4$. Such results hold similarly for $t > t_{jet}$, so there will be a fast- to slow-cooling transition even for quite low values of x. The ratio rises at a low rate, so the rate of decrease in radiative corrections falls between none and the rate of $x = 0$. These are not very different; typically the energy difference between these out to $\sim$ 200 days is $\sim 2\times$, a small effect on the final data with low S/N (see Figure7.1, with data not detected at $3\,\sigma$ significance). We use the synchrotron ν_c/ν_m ratio to calculate the reduction in energy losses during slow cooling for $x > -4/3$. We check two cases for $x < -4/3$: no reduction in $E(t)$ losses and the lessening of energy losses at the rate for $x = 0$. These give substantively the same results, as shown below.

Table 7.3: Fit parameters for the best models with $\epsilon_B = K\gamma^x$

x	χ^2	DOF	t_{cm} [a]	t_{jet}	t_{NR}	E [b] t_{cm}	E 1 day	n cm^{-3}	p	$\epsilon_{B,\%}$ 1 day	K=$\epsilon_{B,\%}/\gamma^x$	ϵ_e	θ [c]
GRB 970508													
+2	945	257	1.7	223	223	1.6	1.8	0.87	2.23	100	2.2	0.19	ISO
+1	695	257	0.57	322	322	1.8	1.5	0.21	2.20	80	8.2	0.24	ISO
0	596	257	0.082	183	203	3.7	1.6	0.20	2.12	25	25	0.34	0.84
−1	600	257	0.028	246	246	7.1	1.6	0.15	2.09	22	220	0.45	ISO
−2 [d]	569	257	0.0015	289	289	27	1.5	0.10	2.07	21	2400	0.59	ISO
−2 [e,f]	703	257	0.0011	498	498	13	2.0	0.032	2.14	100	5.9e4	0.24	ISO
GRB 980329													
+4	112	90	6.5	76	76	2.9	4.7	220	2.31	21	0.021	0.23	ISO
+1	117	90	0.30	1.1	151	4100	3900	150	2.0007	64	4.7	0.027	0.075
0	115	90	6.1	0.12	70	130	170	20	2.88	17	17	0.12	0.036
−1	107	90	0.66	0.16	79	174	170	15	2.56	3.0	29	0.061	0.040
−4 [d,f]	114	90	9e-18	0.38	73	50	27	6.4	2.35	100	2.7e13	0.090	0.064
−4 [e,f]	124	90	1e-18	0.45	83	2000	35	6.9	2.43	100	1.2e13	0.074	0.066
GRB 980703													
+3	230	147	3.4	121	121	0.74	1.2	2.1	2.13	100	1.3	0.39	ISO
+1	194	147	1.3	75	85	1.4	1.6	1.2	2.05	100	13	0.68	0.83
0	170	147	1.4	3.4	50	12	13	28	2.54	0.18	0.18	0.27	0.23
−1	165	147	1.2	3.5	52	14	16	22	2.21	0.083	0.62	0.51	0.23
−3 [d]	180	147	0.026	1.7	76	120	12	2.3	2.06	0.42	370	1	0.13
−3 [e]	174	147	0.044	1.9	76	170	20	3.8	2.06	0.16	140	1	0.14
$-(4^+)$ [f]	180	147	0.36	73	93	3.8	1.9	0.51	2.03	100	1.5e6	0.92	0.78
GRB 000926													
+1	209	93	6.0	8.2	80	3.8	5.3	14	2.88	20	2.5	0.15	0.28
0	138	93	3.4	2.6	79	12	15	16	2.79	2.2	2.2	0.15	0.16
−1	127	93	3.4	1.7	80	23	32	23	2.61	0.26	2.5	0.23	0.13
−3 [d]	198	93	0.043	0.79	100	28	15	2.4	2.18	11	1.5e4	0.20	0.079
−3 [e]	217	93	0.25	0.25	111	85	66	2.7	2.21	6.6	1.0e4	0.15	0.042

---

[a] Time when fast cooling ends at $\nu_c = \nu_m$

[b] Isotropic equivalent blast-wave energy (not corrected for collimation), at the time when $\nu_c = \nu_m$. All tabled energies in units of 10^{52} ergs, and isotropic-equivalent

[c] Jet half-opening angle, in radians; > 1 radian treated as isotropic (ISO)

[d] $x = 0$ rate lessening energy losses in slow cooling

[e] No lessening of E(t) losses, as described at the start of Chapter 7

[f] ϵ_B pinned at 100% throughout the entire data range

Table 7.4: Best fits assuming $\epsilon_B \propto \gamma^{-1}$. The uncertainties are statistical only, without regard to systematic uncertainties in the model assumptions. They are given for the primary parameters (employed in the fit); the other columns are derived from the fitted values. The quoted uncertainties are produced via the Monte Carlo bootstrap method with 1000 trials to generate the parameter distribution. The values bracket the resulting 68.3% confidence interval.

χ^2	DOF	t_{cm} [a] (d)	t_{jet} (d)	t_{NR} (d)	E_{52} [b] t_{cm}	E_{52} 1 d	θ_{jet} rad	n cm^{-3}	A(V) host	p	ϵ_e	$\epsilon_{B,\%}$ t_{cm}	$\epsilon_{B,\%}$ 1 d	$\epsilon_{B,\%}$ t_{NR}
GRB 970508														
600	257	0.028	246	246	$7.1^{+1.2}_{-0.3}$	1.6	ISO [c]	$0.146^{+0.004}_{-0.04}$	$0.09^{+0.03}_{-0.04}$	$2.088^{+0.006}_{-0.002}$	$0.45^{+0.02}_{-0.03}$	$4.8^{+0.4}_{-1.1}$	22	100
GRB 980329														
107	90	0.66	0.16	79	174^{+6}_{-11}	170	$0.040^{+0.004}_{-0.002}$	15^{+4}_{-2}	$1.46^{+0.09}_{-0.08}$	$2.56^{+0.05}_{-0.08}$	$0.061^{+0.008}_{-0.01}$	$2.4^{+0.5}_{-1.1}$	3.0	29
GRB 980703														
165	147	1.2	3.5	52	14^{+2}_{-1}	16	$0.23^{+0.02}_{-0.01}$	22^{+4}_{-3}	$1.25^{+0.05}_{-0.05}$	$2.21^{+0.04}_{-0.03}$	$0.51^{+0.04}_{-0.06}$	$0.091^{+0.010}_{-0.018}$	0.083	0.62
GRB 000926														
127	93	3.4	1.7	80	23^{+2}_{-3}	32	$0.131^{+0.004}_{-0.005}$	23^{+4}_{-5}	$0.036^{(<0.063)}$ [d]	$2.61^{+0.08}_{-0.2}$	$0.23^{+0.05}_{-0.03}$	$0.47^{+0.14}_{-0.15}$	0.26	2.5

---

[a] Time when fast cooling ends at $\nu_c = \nu_m$

[b] Isotropic equivalent blast-wave energy (not corrected for collimation), at the time when $\nu_c = \nu_m$. All tabled energies are in units of 10^{52} ergs, and isotropic-equivalent.

[c] No results with jet half-opening angles < 1 radian; all treated as isotropic (ISO).

[d] No lower constraint on this extinction value; 68.3% confidence interval is < 0.063.

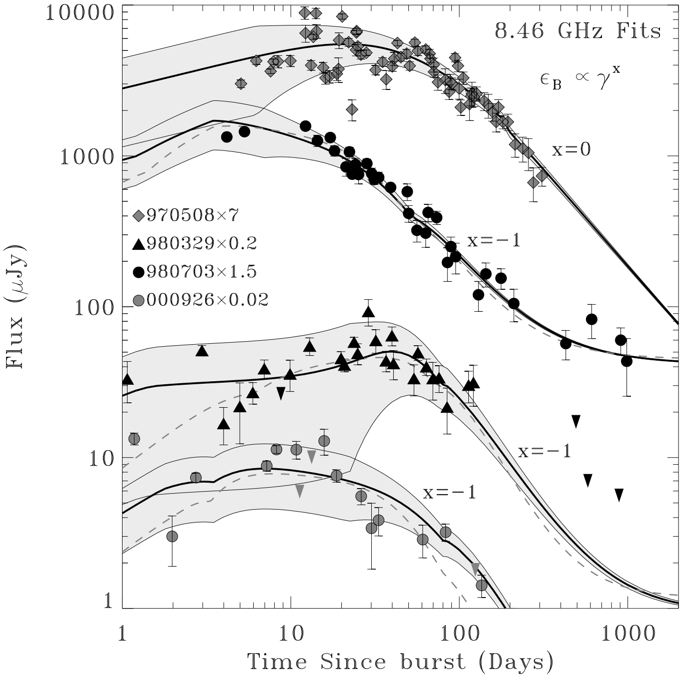

Figure 7.1: 8.46 GHz light curves of the four events presented in Chapter 4, with the best fits (solid lines) for an assumed magnetic energy relation $\epsilon_B \propto \gamma^x$ (§7.3). The light grey envelopes are the estimated scintillation uncertainties (the 970508 scatter is not fully accounted for, but it has scatter excess at all frequencies); data that isn't 2σ significant is shown as 2σ upper limits (downward triangles). 980329 has a radio host component which marginally improves the fit due to a 1.43 GHz average flux excess. In one case (970508) a constant ϵ_B produces the best fit (but only by 1% in the total broadband χ^2); in the others $\epsilon_B \propto \gamma^{-1}$ gives the best fit. For these three, the best constant-ϵ_B fit is shown as a grey dashed line for comparison. The model decay for constant-ϵ_B is generally slightly steeper than the data in the late radio; this is especially obvious in the last few points of the 000926 lightcurve. A magnetic energy increase at late times flattens this decay, improving the fit.

down by a factor ~ 10.

Best fits for various x are in Table 7.3. We find that $x < 0$ fits as well or better than the basic model out to at least $x = -1$ (see Figure 7.1); the best $\epsilon_B \propto \gamma^{-1}$ fits including uncertainties are shown in Table 7.4 and Figure 7.2. The improvement is seen in three of the four cases, while the fit with the $x = -1$ model assumption to 970508 is only 1% worse in the total broadband χ^2 than the basic, constant-ϵ_B fit. The effect of the $x = -1$ assumption on the fit to optical and X-ray data is minor. It takes a long temporal baseline, as in the radio, to see the spectral evolution differences; moreover the optical and X-ray are above the cooling frequency and thus have a lesser flux dependence upon ϵ_B (Table 7.2). Assuming $\epsilon_B \propto \gamma^{-1}$ improves the radio fits—the magnetic energy grows as the shock slows, which allows the peak to rise, flattening the late time decay (see

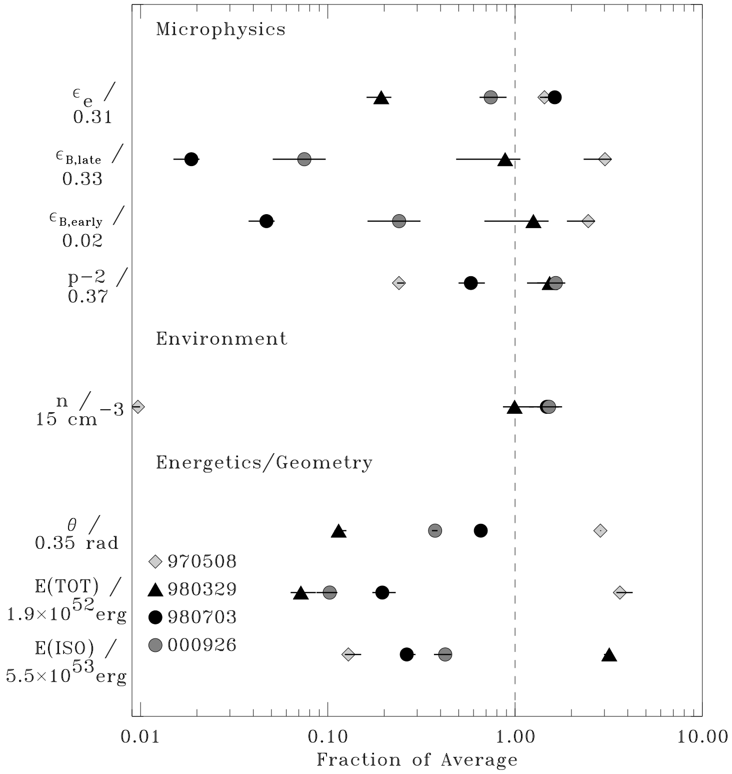

Figure 7.2: Parameters from the best fits assuming $\epsilon_B \propto \gamma^{-1}$ (see Table 7.4). They are divided into three categories: energy & geometry (kinetic energy, collimation half-opening angle θ), environment (density), and microphysics (energy partitions: ϵ_e for electrons, ϵ_B for magnetic fields, and electron energy distribution index p). As it varies, ϵ_B is presented both with its early (at fast- to slow-cooling transition) and final values. See §3.1 for further details concerning the fireball model's parameters, and Figure 5.1 to compare these parameters with those from the fits with constant ϵ_B. The parameters are presented relative to a nominal value as indicated; the error bars are the statistical 68.3% intervals calculated via Monte Carlo bootstraps. This model assumption produces fits as good as (970508) or better than (980329, 980703, 000926) those assuming ϵ_B is constant. However, it does not fit with a universality in the microphysics. There is clearly great flexibility in the model assumptions allowed by the data, and considerable *model* uncertainty in the derived parameters.

Figure 7.1). We note there appears to be a general trend that the radio decays are a bit shallower than the optical / X-ray, so an increasing magnetic energy improves the fit. There are other possible causes since any effect that increases the peak flux, such as an increasing energy or density, will flatten the radio decay.

We find that $x > 0$ worsens the fit. We quit finding a good fit around $x = +2$ or $+3$, depending upon the sensitivity of the data set. For $x < 0$, we either find no good fit, or reject on physical grounds the parameters of good fits around $x = -3$ or $x = -4$. At that point the changes that improve the fit around $x = -1$ become too radical. More details are in the sections below.

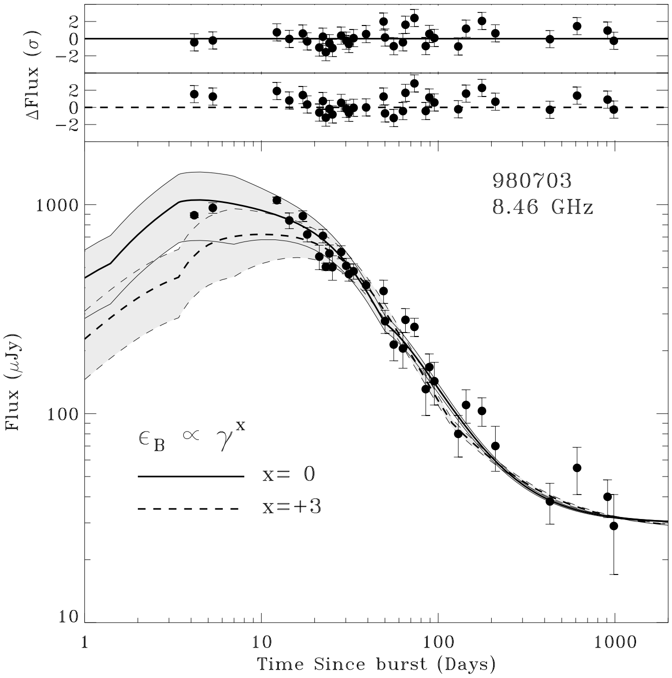

Figure 7.3: GRB 980703 at 8.46 GHz with the constant-ϵ_B and $\epsilon_B \propto \gamma^{+3}$ fits, showing where the assumption about the magnetic energy can no longer fit the data (see Figure 7.1). With the spectral peak $\propto \epsilon_B^{1/2}$, the model radio flux peaks too low and declines too steeply, as seen in the excess of positive residuals (which include the scintillation indicated by the shaded envelopes and 5% broadband cross-calibration model uncertainties) at < 10 and ~ 100 days. The effect is exacerbated by a more rapid decline in the peak frequency; the effect is stronger post-jet. The other data sets have similar difficulties fitting for $x > 0$. The fit to 970508's data places the model above the early radio in order to match part of the decline. The 980329 fit matches the peak to the radio level and is then too steep to match the declining radio data. The 000926 data is not well fit even assuming $\epsilon_B \propto \gamma^{+1}$; the more rapid post-jet decline will not fit the radio for a jet break early enough to match the optical data.

7.1 Magnetic Energy in Decline: Limits for $x > 0$

For a sufficiently steep $\epsilon_B \propto \gamma^x$ and $x > 0$, the resulting model behaviour can no longer fit the data sets despite any compensating changes in other parameters. The peak flux is proportional to $\epsilon_B^{1/2}$, so that one of the chief spectral behaviour changes is that the peak flux drops, producing steeper decays (see Tables 7.1 and 7.2). This leads to a poor radio fit by $x \approx +3$, often with the radio peak flux too low in order to give an appropriate earlier peak flux relative to the optical data. There can also be some fit difficulties at higher frequencies. The poor fit there may be due to a drop in IC flux components for higher early ϵ_B, or a change in the spectral slope from its link to the decay rates.

Figures 7.3 and 7.4 show these effects for the 980703 afterglow assuming $\epsilon_B \propto \gamma^{+3}$. Clearly the model is lower than the X-ray data. The fit barely matches the X-ray flux level, passing below two of the four points by approximately $2.5\,\sigma$. The radio flux is systematically too low at early times, peaking below the data at $\lesssim 15$ days. The model reproduces the start of the decline, but declines too steeply out to the non-relativistic transition.

Some of this poor radio fit results directly from a high value of x. The value of ϵ_B is very small at late times by comparison to the early ϵ_B; the early ϵ_B is quite large. Around Day 1, $\epsilon_B = 100\%$ and around Day 40 post-burst, when the radio data is peaking, $\epsilon_B \simeq 1\%$ in the model. The peak flux is proportional to $\epsilon_B^{1/2}$. For the appropriate synchrotron peak to model the optical flux at Day 1, the peak flux at 40 days will be 1/10 that value. The fit without an ϵ_B decline is relatively good, but the radio peak is too low (Figure 7.3). The radio decline post-peak ($\nu_m < \nu < \nu_c$, Table 7.2) has a time dependence of $t^{-1.05-0.32x}$ pre-jet and $t^{-2.4-0.43x}$ post-jet (for $p = 2.4$). The value $x = +3$ steepens the radio decline, so that the disappearance of the jet break is necessary in order to avoid making the situation worse.

Some indirect results partially compensate. The lower density gives a larger early radio flux (for $\nu < \nu_a$, Table 7.2). However, the lower density drops the IC flux that dominated the X-ray in the simple model's fit (see Figure 7.4). A smaller value of p will help to fix the optical−to−X-ray ratio and give a greater synchrotron flux at the X-ray frequencies to compensate. The overall flux level also increases to raise the X-ray model, and some of the optical flux is suppressed with extra host extinction. The spectral index is a poor match to the optical data (the early model is below the R and above the K data, with the host components altering to compensate). This still does not suffice; the fit doesn't match the X-ray data.

Fits to the other data sets are not good at $x = +3$ either. We find that without a strong jet break, model assumptions of $x = +1$ or $+2$ produce acceptable fits. With a strong jet break, we find no acceptable fit to the 000926 event with $x \geq +1$.

The GRB 980329 fits show a very similar account to 980703's. The parameter changes are almost all in the same direction as those in 980703, and assuming $x = +3$, the model no longer fits. The jet break also drops to avoid the steep post-jet decays accompanied by $x > 0$. The 980329 optical

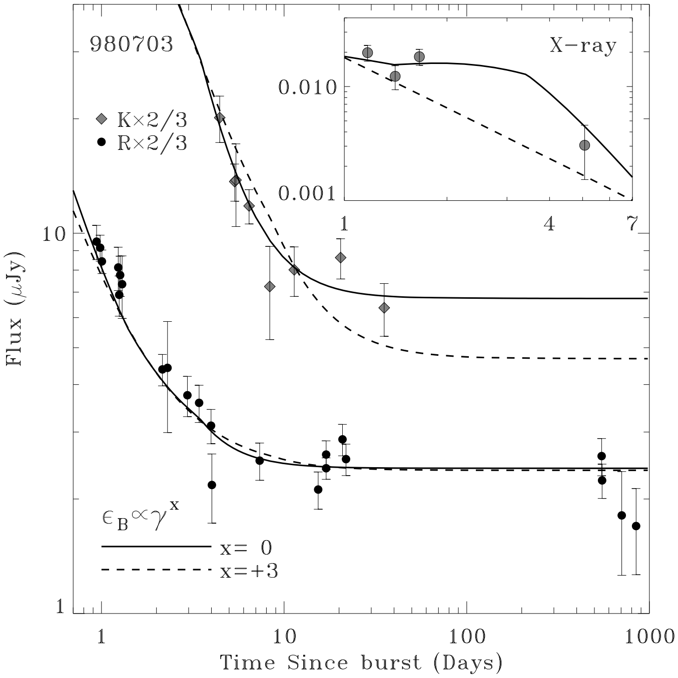

Figure 7.4: X-ray and selected optical data for GRB 980703, with the best constant-ϵ_B and $\epsilon_B \propto \gamma^{+3}$ fits. With $x = 3$, $\epsilon_B \propto \gamma^{x>0}$ no longer fits the data (see §7.1). The effects are more dramatic at lower frequencies (Figure 7.3) but even the high frequency fits can become marginal. The poor fit is due to accomodations for the faster decays and lower radio peaks resulting from the spectral peak's dependence as $\epsilon_B^{1/2}$. For this burst, by $x = 3$, the X-ray flux is underestimated and the spectral index is a poor match to the optical data (early, it is below the R and above the K data, with the host components altering to compensate). That fit uses a lower circumburst density than the constant-ϵ_B one (Table 7.3) in order to produce a larger early radio flux. This reduces the IC flux contribution in the X-ray, compensated by increasing the overall flux level and suppressing some of it at the optical with extra host extinction, making the optical–NIR spectral index not optimal. Moreover, the optical−to−X-ray spectral index flattens and yet the fit doesn't match the X-ray data.

data is not very constraining, so the model can scale the radio flux level to almost match the radio peak, but this then makes the rise and fall of the peak too steep to accomodate the radio data.

The model assumptions break down for the 970508 data at $x = +2$ because $x > 0$ causes a steep decay in the radio. The 970508 fit places the early radio too high, in order to reproduce the decay. The high peak requires a larger p to connect the optical level to the peak, and this steeper p makes the optical−to−X-ray connection too steep, placing the model too low at high frequencies.

Finally, the 000926 data cannot accomodate much in the way of $x > 0$, in contrast to the other data sets. This is due to its visible jet break. A model with $x = +1$ and a jet break earlier than Day 3 had the model flux far too low in the radio. The peak flux is dropping even pre-jet, and ν_m drops more quickly (see Table 7.1), so the peak is closer to the radio at the jet break and passes earlier.

The decay is too early. A better fit pushes the jet break out later, despite the fact that this does not match the optical data well. There is no suitable fit with $x = +1$ assumed.

7.2 Magnetic Energy Growing Like a Weed: Limits for $x < 0$

While the $x = -1$ assumption produced improved fits, a negative enough x can no longer match the data, a point reached for $x \approx -3$. There are two subtleties involved in the fits for such small x.

First, for $x \ll 0$, ϵ_B will become unphysically high (capped physically at 100%), even if the value is reasonable at early times. For small enough x, ϵ_B will reach this limit over all or nearly all of the time range over which data is recorded. If a good fit is possible with $\epsilon_B = 100\%$, then a more negative x may find a good model fit. This would be unacceptable because the data could only be described with unphysical parameters, formally with all the energy in the magnetic field, leaving none for the shock or electrons. Therefore the question becomes whether a good fit is possible for a certain $x < 0$ which also has reasonable parameter values over (at least the great majority of) the data's time range.

Secondly, there is the rate at which energy losses decrease for $x < -4/3$, as explained earlier in the chapter. The approximation we use, that the rate at which ν_c/ν_m increases is given by the synchrotron-only rates at which the break frequencies change, would not give the right behaviour. Without accounting for inverse Compton cooling, the ratio would decrease. With inverse Compton cooling dominating as ϵ_B grows (see §3.4), the ratio increases slowly; energy losses slow less quickly than the rate in the basic model, where ϵ_B is constant. For $x < -4/3$ we fit the two slightly different model assumptions that bracket the expected result: no decrease of energy losses at all, and a diminishment at the basic model rate. In both Table 7.3 and the figures we include fits for both assumptions when the model assumes an index $x < -4/3$. These Figures and Table show that there are only small differences in the results at a particular x, using the two bracketing fit assumptions.

By $x = -3$, the model can no longer fit the 980703 data. The basic trends cannot all be reproduced and the electron energy fraction is forced to its unphysical limit of 100%. There were fits that did not have $\epsilon_e = 100\%$, although they were not as good, and moreover they did not eliminate

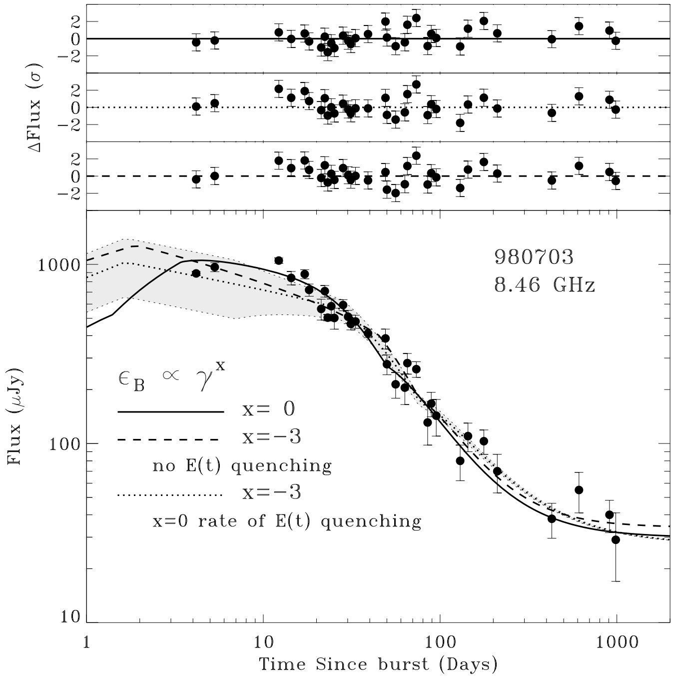

Figure 7.5: 980703's 8.46 GHz data, with the best constant-ϵ_B and $\epsilon_B \propto \gamma^{-3}$ fits, showing where this assumption about the magnetic energy can no longer fit the data. $x = -3$ is shown with two rates at which energy losses slow; they give the same result. An envelope shows the estimated model uncertainties from scintillation (ISS) for one case; the same fractional uncertainty was used for all. The peak is too early, as seen in the residuals from 10–20 days (these include ISS and a 5% broadband cross-calibration uncertainty). This is because $\nu_m \propto \epsilon_B^{1/2}$ is slowed by the increasing ϵ_B and cannot pass the radio early enough; the peak is at the jet break and only because $\epsilon_e \to 1$ for extremely fast radiative energy loss. The jet break must remain early due to shallow decays from an increasing spectral peak proportional to $\epsilon_B^{1/2}$, as shown in Figure 7.6.

the problem of unphysical parameters; ϵ_B was 100% over nearly the entire data set, reaching the maximum only a few days post-burst.

The break frequency behaviour is strongly affected for $x = -3$ and 980703's radio peak cannot be matched (Figure 7.5). The breaks ν_c and ν_m drop quite slowly (Table 7.1); the peak frequency does not pass until much later than the peak at ~ 10 days. The radio peak is modelled in this case by the jet break. With large energy corrections (forcing $\epsilon_e \to 1$), above ν_a there is a shallow post-jet decline (Table 7.2). The X-ray data requires a jet break considerably earlier than 10 days so the radio decline begins well before the peak in the data and the model does not fit the radio peak.

The unphysical ϵ_e in the fit to 980703 for $x = -3$ is also required to counter the shallow decay at optical and X-ray frequencies (Figure 7.6). Since ϵ_B starts smaller than ϵ_e, IC cooling will dominate

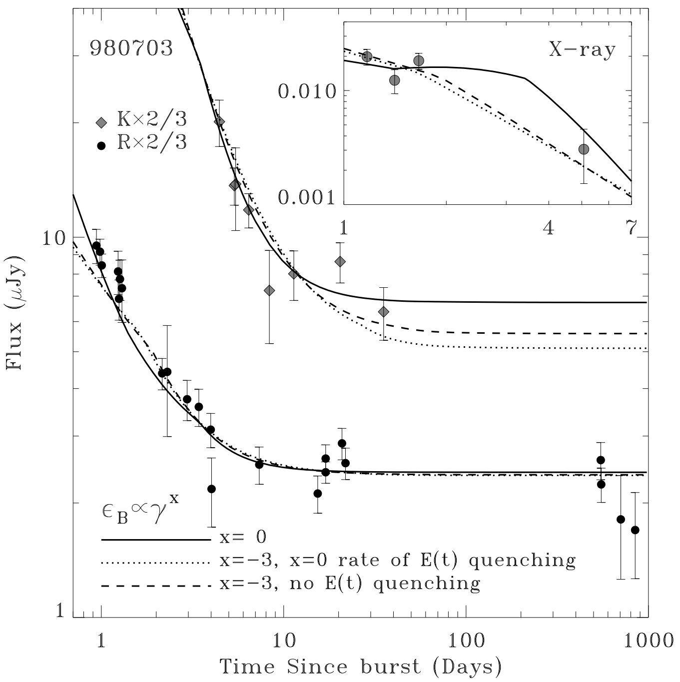

Figure 7.6: 980703's X-ray and selected optical bands' data, with the best constant-ϵ_B and $\epsilon_B \propto \gamma^{-3}$ fits, demonstrating where this assumption about the magnetic energy can no longer fit the data. Two rates at which the energy losses subside for $x = -3$ are shown; they give the same result. For $x = -3$ the spectral peak rises, the peak frequency drops slowly, and the decays are shallow. An early jet break is required to steepen the decay (which sets the radio peak too early, seen in Figure 7.5). The IC flux component, dominating the constant-ϵ_B X-ray model, makes the $x = -3$ decay too shallow, and thus is suppressed. For the synchrotron flux level to match the X-ray's requires a combination of a shallower spectrum from the optical to the X-ray and increased flux in the optical (suppressed by extra host extinction). This change makes the optical fit marginal.

the behaviour of ν_c. While for pure synchrotron flux the behaviour of the flux density above all the spectral breaks (generally corresponding to the optical and X-ray regimes) is only very slightly dependent upon ϵ_B, it is not the case here. The effect is approximately $\nu_c = \nu_c^{synch} \times \epsilon_B/\epsilon_e$ (Sari & Esin, 2001), so that roughly $F_\nu \propto \epsilon_B^{0.6}$. Thus with ϵ_B rapidly increasing, the decay becomes considerably shallower. The maximal ϵ_e increases the decay rate due to energy losses. The jet break t_{jet} is low in the model fit, as the decay steepens post-jet. This effect is clearly seen in the X-ray (Figure 7.6), where IC flux is not needed as the synchrotron flux is quite shallow enough to accomodate the data. The IC flux would decay even more shallowly, due to the dependence of γ_c on ϵ_B. Consequently, the fitted density value drops to decrease the IC flux peak, and the value of the index p drops to increase the X-ray flux relative to the optical flux level.

As expected, beyond this, not even a marginal fit can be found without $\epsilon_B = 100\%$ for the entire data set. A fairly reasonable fit, but with this unphysical parameter limit, is presented in Table 7.3 as the best solution for "$x = -4^{+}$". This fit requires extreme parameters. Both energy partitions, ϵ_e and ϵ_B, are 100%.

This occurs at $x = -4$ for 980329. There are reasonable fits to that event with assumptions through $x = -3$ but beyond that index for the magnetic energy fraction no good fit can be found with $\epsilon_B < 100\%$ in the data's time range. By that point, the model's early radio flux would decline rather than rise, in contradiction to the data. This is seen for $\nu < \nu_a < \nu_c$, $t < t_{jet}$ in Table 7.2 when $x < -2$. IC-dominant cooling changes the time dependence of ν_c and the radio flux rises out to about $x = -4$. There is also a general trend as in the 980703 case for a lower spectral index p, again pushing ϵ_e to 100%. The only good 980329 fit with the assumption $\epsilon_B \propto \gamma^{-4}$ pins the magnetic energy fraction at 100%, circumventing these problems.

970508 fits poorly in a similar manner to 980703, but the fit breaks down more quickly with x, at $x = -2$. As shown in Table 7.3, its parameter changes are similar to those for 980703 as it reaches assumptions where it can no longer be fit.

000926 fits poorly when its definite optical break is no longer well-modelled. With IC cooling dominant, the pre-jet flux is too shallow and the jet break is pushed back earlier than the data. The fit tries to accomodate the data's break with the steepening associated with the change in cooling dominance from IC to synchrotron. That break does not match the data well. It also requires ϵ_B to become larger than ϵ_e around the optical break, placing the time at which ϵ_B reaches the unphysical limit fairly early, $\approx$ 10 days post-purst.

7.3 Magnetic Energy Fraction Evolutionary Constraints

In summary, the data do not constrain the fireball model to have a constant magnetic energy fraction ϵ_B. Good fits are possible with both increasing and decreasing ϵ_B, generally as strongly as $\epsilon_B \propto \gamma^{+1}$ through γ^{-2}. With γ changing by a factor $\sim$ 10 over the data range, this allows an extra change in magnetic field strength by a factor of $\sim$3–10. Moreover, the increasing magnetic energy with $\epsilon_B \propto \gamma^{-1}$ tends to improve the model fit to the radio data. As $\boldsymbol{B} \propto \gamma\,\epsilon_B^{1/2}$, a more constant level

$\boldsymbol{B} \propto \gamma^{1/2}$ fits slightly better than the basic model.

The allowable changes to the model significantly alter the fit parameters. We examine the differences between the fitted parameters to the basic model ($x = 0$) and equally good fits where the magnetic energy fraction grows ($x = -1$) in Table 7.3. Parameters change by small fractions in some cases, but up to factors of ≈ 2 (for some of the energy E and electron energy fraction ϵ_e values). Taking the comparisons further to the marginal fits ($x = +1$, -2 or -3), we find again some of the changes are by small fractions, but changes by factors of 2 are more common, and some (such as certain events' densities n) change by factors up to ≈ 5. It is clear that the uncertainty from model assumptions is greater than the apparent uncertainties in the fit parameters once different assumptions concerning the evolution of the magnetic energy fraction are adopted.

Chapter 8

Investigation of Density Profiles $n \propto r^S$

The circumburst medium (CBM) density profile, generally approximated as a power law $n \propto r^S$, is an important clue to the nature of the progenitor. In this chapter, we investigate the range of power law indices S tolerable by the events presented in Chapter 4. These fit to the basic model with $S = 0$ (and in one case as well with $S = -2$). The following discussion is largely taken from our work presented in Yost *et al.* (2003).

The ISM-like case is the simplest density model. A low ISM-like density would be expected for progenitors in galactic haloes, such as most types of merging compact binaries. Giant stars are known to produce winds. A wind in a steady state of constant mass-loss produces an r^{-2} profile, the expected Wind-like signature of a massive star employed by, e.g., Dai & Lu (1998); Chevalier & Li (2000). A number of profiles have been considered by GRB theorists. This includes "naked GRBs", where a constant density drops to zero after a certain radius (Kumar & Panaitescu, 2000). Ramirez-Ruiz *et al.* (2001) discuss the evolution of the afterglow through the ejecta left by a Wolf-Rayet star, showing that r^{-2} is a very crude approximation to the environment about a massive star. Nevertheless, despite evidence for massive stellar progenitors from other sources (see Mészáros (2002)'s review of positions within the host, supernova [SN] associations, and Stanek *et al.* (2003) for the spectroscopic discovery of a SN associated with GRB 030329), most model fits do as well or better with the ISM-like approximation to the density profile than the Wind-like one (e.g., Panaitescu & Kumar, 2002), although there is one case where a Wind-like CBM fits and an ISM-like cannot (Price *et al.*, 2002b).

We investigate a wide range of density profiles, parametrized as $n \propto r^S$. We recalculated the equations for the model presented in §3.1 allowing a general power law density profile index S. This includes changes to the radiative loss estimates, as presented in Cohen, Piran & Sari (1998). There are no general calculated adjustments in the equation normalizations accounting for the post-shock electron distribution with a generic density profile, so we used the order of magnitude estimates (including for γ, which gives t_{jet}), and the estimate that from the jet expansion, $t_{NR}/t_{jet} \approx \theta^2$.

We expect cases of $S < 0$ to help constrain how sensitive the model is to the details of a mass-loss wind from the supposed progenitor star. Cases of $S < -2$ become so rarified as to approach the CBM form of an evacuated cavity, where the afterglow shock accumulates (almost) no matter. The Blandford & McKee (1976) solution's equations for the fireball energy break down at $S = -4$ (but see Best & Sari, 2000, for $S < -4$).

Conversely, $S > 0$ models a fireball plowing into a medium that gradually increases in density. This could mimic a denser region surrounding the burst (though not a sharply bounded overdensity). For $S \gg 1$, such models offer insight into the behaviour when hitting the edge of a very dense, but not sharp, shell surrounding the burst. The use of such a rapidly increasing density profile is illustrative, but not perfectly realistic. The density increase must continue over the region from which the afterglow is emitted, yet must eventually have some outer boundary. The calculated fireball evolution does not directly model the extinction column from the material, so the density increase would have to cut off before the material ahead would absorb all the light emitted from the shock.

Table 8.1 details the expected behaviour of the spectral breaks with general S. An increasing density ($S > 0$) does not change the behaviour as greatly as a rarefaction ($S < 0$). As a result, rapid changes are expected for decreasing $S < 0$, not increasing $S > 0$. The reasons are illustrated by the range in densities probed and that the rate at which the shock γ slows depend upon a density profile.

Taking the observer time t affected by relativistic beaming, and the relativistic energy, $E = M\gamma^2$

Table 8.1: Spectral parameters' dependences with $n = n_i(r/r_i)^S$

	Energy	density [a]	ϵ_e	ϵ_B	$t,\ t < t_{jet}$	$t,\ t > t_{NR}$ [b]
F_{max}	$E^{(8+3s)/(8+2s)}$	$n_i^{2/(4+s)}$	ϵ_e^0	$\epsilon_B^{0.5}$	$t^{s/(8+2s)}$	$t^{(2s+3)/(s+5)}$
ν_a [c]	$E^{0.8(s+1)/(s+4)}$	$n_i^{2.4/(s+4)}$	ϵ_e^{-1}	$\epsilon_B^{0.2}$	$t^{0.6s/(s+4)}$	$t^{(16s+30)/(5s+25)}$
ν_m	$E^{0.5}$	n_i^0	ϵ_e^2	$\epsilon_B^{0.5}$	$t^{-1.5}$	$t^{-(4s+15)/(s+5)}$
ν_c	$E^{-(3s+4)/(8+2s)}$	$n_i^{-4/(s+4)}$	ϵ_e^0	$\epsilon_B^{-1.5}$	$t^{-(3s+4)/(8+2s)}$	$t^{-(2s+1)/(s+5)}$

---

[a] the density at a reference radius r_i

[b] to the model approximation, r is constant during the jet spreading phase, and so the behaviour at $t_{jet} < t < t_{NR}$ is the same for any density profile (see Table 7.1, for $x = 0$)

[c] For the order $\nu_a < \nu_m < \nu_c$. When $\nu_a < \nu_c < \nu_m$, multiply by $(\nu_m/\nu_c)^{1/2}$; other orderings have other factors.

(c=1), with M from the density profile $n \propto r^S$, we find

$$E \propto r^{S+3}\gamma^2, \quad and \quad t \propto r\gamma^{-2}\,.$$

Solving for r gives

$$n \propto r^S \propto (Et)^{S/(S+4)}\,.$$

As evident from the above equation, for S greater than a few, the rate at which density n increases with *observer time* is weakly dependent upon S, despite its strong dependence on radius. Moreover, in the adiabatic approximation, with E constant,

$$\gamma \propto t^{-(S+3)/(2S+8)}\,.$$

For $S \geq 0$, the rate of slowing only varies from $\gamma \propto t^{-3/8}$ to $\gamma \propto t^{-1/2}$; it depends quite weakly on the density profile for S larger than a few.

By way of contrast, as discussed in the previous chapter, the rapidity of the change in model behaviour is symmetrical for $x < 0$ and $x > 0$ when $\epsilon_B \propto \gamma^x$. The shock γ will drop from typically more than ten in the early afterglow observations to $\gamma = 1$ at the non-relativistic transition, regardless of the behaviour of ϵ_B. Both for $x > 0$ and $x < 0$, changes of $\delta x \sim 1$ were significant. In this case, the behaviour of the model should change rapidly for decreasing $S < 0$, but not for increasing $S > 0$.

Moreover, in our model, the post-jet shock evolution is not sensitive to density (since it is stopped

Table 8.2: Model flux dependences with $n = n_i(r/r_i)^S$

Spectral Region	Parameters	$t,\ t < t_{jet}$ [a]	$t,\ t > t_{NR}$ [a]
For $\nu_a \ < \ \nu_m \ < \ \nu_c$			
$\nu < \nu_a$	$E^{\frac{2}{4+s}} n_i^{\frac{-2}{4+s}} \epsilon_e \epsilon_B^0$	$t^{\frac{2}{4+s}}$	$t^{\frac{-2(s+1)}{s+5}}$
$\nu_a < \nu < \nu_m$	$E^{\frac{10+4s}{12+3s}} n_i^{\frac{2}{4+s}} \epsilon_e^{\frac{-2}{3}} \epsilon_B^{\frac{1}{3}}$	$t^{\frac{s+2}{s+4}}$	$t^{\frac{10s+24}{3s+15}}$
$\nu_m < \nu < \nu_c$	$E^{\frac{p}{4}+\frac{12+5s}{16+4s}} n_i^{\frac{2}{s+4}} \epsilon_e^{p-1} \epsilon_B^{\frac{p+1}{4}}$	$t^{\frac{-3p}{4}+\frac{12+5s}{16+4s}}$	$t^{\frac{8s+21-(4s+15)p}{2(s+5)}}$
$\nu_c < \nu$ [b]	$E^{\frac{p+2}{4}} n_i^0 \epsilon_e^{p-1} \epsilon_B^{\frac{p-2}{4}}$	$t^{\frac{-3p+2}{4}}$	$t^{\frac{6s+20-(4s+15)p}{2(s+5)}}$
For $\nu_a \ < \ \nu_c \ < \ \nu_m$			
$\nu < \nu_a$ [b]	$E^{\frac{-s}{4+s}} n_i^{\frac{-12}{12+3s}} \epsilon_e^0 \epsilon_B^{-1}$	$t^{\frac{4}{4+s}}$	$t^{\frac{8s+10}{3s+15}}$
$\nu_a < \nu < \nu_c$ [b]	$E^{\frac{14+6s}{12+3s}} n_i^{\frac{10}{12+3s}} \epsilon_e^0 \epsilon_B$	$t^{\frac{2+3s}{12+3s}}$	$t^{\frac{2s+5}{2s+10}}$
$\nu_c < \nu < \nu_m$ [b]	$E^{\frac{3}{4}} n_i^0 \epsilon_e^0 \epsilon_B^{\frac{-1}{4}}$	$t^{\frac{1}{4}}$	$t^{\frac{-s+5}{s+5}}$
$\nu_m < \nu$ [b]	$E^{\frac{p+2}{4}} n_i^0 \epsilon_e^{p-1} \epsilon_B^{\frac{p-2}{4}}$	$t^{\frac{-3p+2}{4}}$	$t^{\frac{6s+20-(4s+15)p}{2(s+5)}}$

---

[a] To the model approximation, r is constant during the jet spreading phase, and so the behaviour at $t_{jet} < t < t_{NR}$ is the same for any density profile (see Table 7.2, for $x = 0$).

[b] For synchrotron cooling dominating. The frequency ν_c's behaviour changes for IC-dominant cooling; see §3.4 for details.

and expands laterally) until the non-relativistic transition. Changing the parameters to maintain the same jet break for different S may make the non-relativistic transition come at a somewhat different time, but the effect is not dramatic. The question becomes whether the model with a given S can reproduce the behaviour pre-jet. To examine this, we choose the two data sets with sufficient data for well constrained jet break times. GRB 970508, which was well fit with near-isotropy, and GRB 000926, with a sharp jet break seen in the optical, are most useful to constrain possible model fits for various S. The others had more limited optical data, where jet breaks are generally the most obvious, as it was either sparsely sampled or partly masked by a bright host. (In §4.5, we note that the GRB 980703 data set could be fit equally well by ISM-like and Wind-like density profiles; clearly at least some very good data sets do not constrain $n(r)$.)

The results of these fits are in Table 8.3 below. We examine the cases $S < 0$ and $S > 0$ in the following sections.

Table 8.3: Fit parameters for the best models with $n = n_i(r/r_i)^S$

S	χ^2	DOF	t_{cm} [a]	t_{jet}	t_{NR}	E_{cm} [b]	E 1 d	n_{18} [c]	n [d] 1 d	R_{18} [e] 1 d	n [d] 100 d	R_{18} [e] 100 d	p	ϵ_B (%)	ϵ_e	θ [f]
GRB 970508																
12.5	617	257	0.0044	52	52	8.3	0.75	0.087	0.14	1.0	1.9	1.3	2.08	3.2	0.56	1 [g]
0	596	257	0.082	183	203	3.7	1.6	0.20	0.20	0.57	0.20	1.4	2.12	25	0.34	0.84
-2.5	832	257	4.5	1.3×10^5	1.3×10^5	0.44	0.50	0.021	3.3	0.13	0.0023	2.4	2.32	100	0.052	1 [g]
-2.5	1012	257	3.8	6.2×10^3	6.2×10^3	1.8	2.6	0.25	170	0.0074	0.30	0.93	2.28	0.095	0.20	1 [g]
GRB 000926																
12	160	93	1.8	1.6	23	4.3	5.4	9.4×10^7	70	0.31	320	0.35	2.14	0.34	0.35	0.27
12	141	93	2.2	2.2	26	7.5	9.7	1.9×10^7	73	0.35	530	0.42	2.64	0.026	0.31	0.29
10	135	93	2.1	1.9	26	6.7	8.2	1.6×10^7	92	0.30	560	0.36	2.45	0.046	0.26	0.27
0	138	93	3.4	2.6	79	12	15	16	16	0.29	16	0.37	2.79	2.2	0.15	0.16
-2.5	196	93	0.35	4.7×10^7	4.7×10^7	48	47	0.17	1.2	0.46	0.00056	9.9	2.88	0.046	0.033	1 [g]

---

[a] Time when fast cooling ends at $\nu_c = \nu_m$

[b] Isotropic equivalent blast-wave energy (not corrected for collimation), at the time when $\nu_c = \nu_m$. All tabled energies are in units of 10^{52} ergs, and isotropic-equivalent.

[c] Density at $R = 10^{18}$cm, in units of cm^{-3}. This is what the fit scales to, while the following columns give the density calculated post-fit for 1 and 100 days, which give an idea of the range of density probed in the model. The fit uses the scalings based upon the density power law and does not calculate the density at each time.

[d] in units of cm^{-3}

[e] Radius in units of 10^{18} cm, as calculated, not a fit parameter

[f] Jet half-opening angle, in radians

[g] Jet angles ≥ 1 radian are treated as isotropic

8.1 Accelerating into a Blown-out Region: $n \propto r^{S<0}$

We have seen cases where $n \propto r^{-2}$ densities can fit the data, but it is difficult to even marginally fit models with as steep a gradient as $r^{-2.5}$ (see the best fits in Table 8.3). For 000926, for example, we could not find a satisfactory fit with $r^{-2.5}$ (see Figure 8.1). GRB 970508 is also not well fit by $n \propto r^{-2.5}$. Its $r^{-2.5}$ model with the best χ^2 in Table 8.3 has an unphysical $\epsilon_B = 100\%$, and the model under-predicts the X-ray flux (see Figure 8.2). Figure 8.2 shows the best 970508 model for $r^{-2.5}$ with the constraint that $\epsilon_B < 100\%$, which does not fit the radio data.

The essential question for this model assumption in relation to the GRB 000926 data set is whether its spectral behaviour can satisfactorily match the strong achromatic temporal break in the optical (initially discussed in §4.1.2, shown for the B and R bands in Figure 8.1). Matching this behaviour with a jet break encounters a difficulty in decelerating the shock quickly in a rapidly declining density gradient, to produce the jet break at early times. Moreover, the model declines more steeply for $\nu_m < \nu < \nu_c$ than the steepest decay of the isotropic ISM model (Table 8.2), and ν_c rises, guaranteeing this decay at late times. It thus becomes possible to reproduce a steep decay (as in the post-jet case) without a jet break in the model. The favoured $r^{-2.5}$ model is isotropic.

Despite its steepness, the 000926 $r^{-2.5}$ model is not a good fit in the optical, as is seen in Figure 8.1. The rollover in the spectrum does not match the jet break time, nor its sharpness, so the early R data is under-predicted by the model. The effect is best-seen in densely sampled light curves; the B band is a closer fit to the $r^{-2.5}$ model.

In addition, the radio peak in this model is systematically early, also shown in Figure 8.1. The impact of this on the χ^2 is small, since there is uncertainty in the radio model due to interstellar scintillation. However, ISS fluctuations should produce random deviations from the true flux and not observations consistently below it for the first week. For the ISM-like model, the peak occurs when ν_m crosses the radio in the isotropic case, or above ν_a post-jet (the best model has the radio come out of self-absorption post-jet, around a month post-burst). The early radio peak is a direct consequence of the steeply declining density for $n \propto r^{-2.5}$. The the flux density declines above ν_a for the isotropic $n \propto r^{-2.5}$ case (see Table 8.2, and 7.2 for the post-jet evolution at all density profiles).

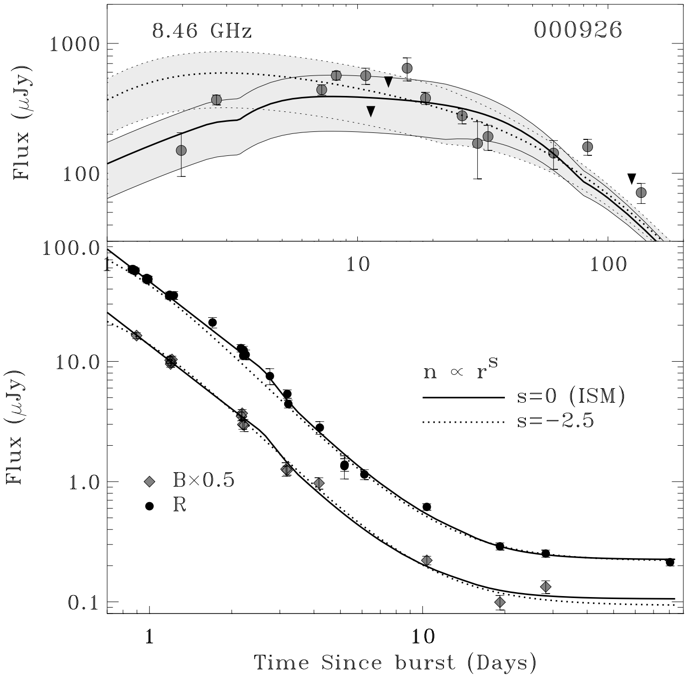

Figure 8.1: GRB 000926, selected optical and radio bands comparing the best fit to ISM and $n \propto r^{-2.5}$ profiles. The radio model envelopes show the assumed scintillation (ISS) uncertainties. When assuming $n \propto r^{-2.5}$, no good fit was possible with a jet break. The peak flux declines rapidly pre-jet (Table 8.1); if the peak scales to fit the early optical, it is low by the jet break time, and too low in the radio. The radio model will also decay too early due to ν_a's rapid decline as the shock moves into less dense material. For this profile, the isotropic case declines more steeply than for an ISM-like density. It is possible to get steep decay without a jet break as in the best fit, seen here. It cannot reproduce the strong break in R, although the fit to the less-densely sampled B data is good. Furthermore, its radio peak is too early. The flux density declines above self-absorption for $n \propto r^{<-2}$(Table 8.2); the peak is due to the (early) passage of ν_a. This does not affect the overall χ^2 much due to the model's ISS uncertainty, but ISS fluctuations in the data should be random, not systematically below the model. There is no satisfactory 000926 model for such a steep density profile.

The peak occurs as ν_a passes below the radio frequencies, which is early since ν_a drops relatively quickly as the shock moves into less dense material (see Table 8.1). The 000926 data is not well fit by this model.

To determine why that poor isotropic fit would nevertheless be preferred over a jet, we investigated jetted $n \propto r^{-2.5}$ models, finding a model that fit (although more poorly) with $t_{jet} \approx 2.7$ days. Unlike the model discussed above, the optical fit was quite reasonable, although the slight increase in t_{jet} caused a slight increase in p to steepen the post-jet decay. The resulting steeper spectral index gives a model that overestimates the near-IR K band data. However, the main problem with the model was a systematically low radio peak. This results from the declining pre-jet F_{max} and ν_a

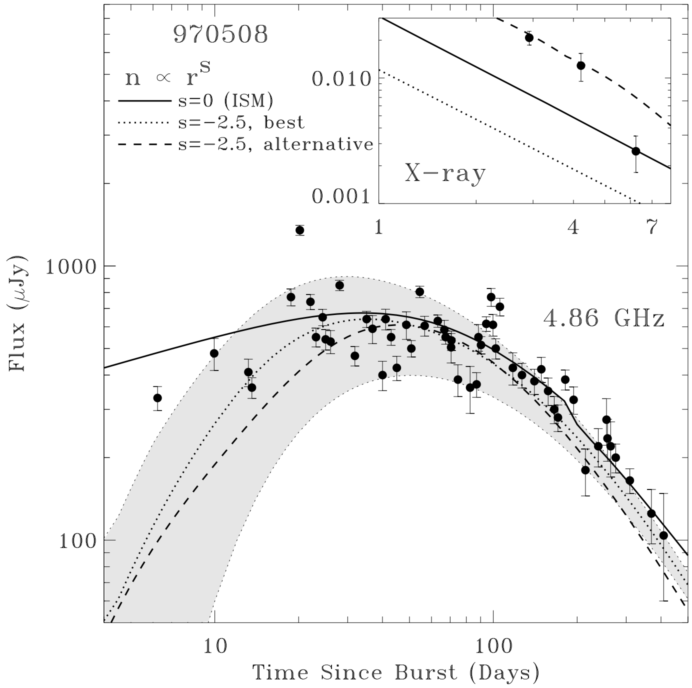

Figure 8.2: GRB 970508, 4.86 GHz and X-ray data with the best fits to ISM and $n \propto r^{-2.5}$ profiles (data selection explained in §4.3). The radio envelope shows the estimated model uncertainties from scintillation (ISS) for one case; the same fractional uncertainty was used for all. Two models are presented for $r^{-2.5}$: "best" had the best χ^2 but an unphysically high ϵ_B of 100%; the "alternative" is the best with reasonable parameters (Table 8.3). Neither fits the data. The best fit pushes ϵ_B unphysically high to put these breaks initially higher. In addition, the peak flux drops in time, so the fit puts it high early on and the peak-optical spectrum must then be steeper than in the ISM case, causing a steeper optical−to−X-ray spectrum; the best fit model is lower than the X-ray data. The $r^{-2.5}$ alternative fit has a higher density and makes up the difference in the X-ray with an IC flux component. Nevertheless, the alternative fit rises and falls too sharply, as ν_a and ν_m fall rapidly, giving a steep decay; it under-predicts the data past 100 days. The ISM fit reasonably describes the data's trends even though the scatter in the data produces an unreasonably improbably χ^2, but no $r^{-2.5}$ density profile fit is a good match to the data.

in the $n \propto r^{-2.5}$ model (Table 8.1). A peak scaled to fit the early optical data will be lower at the jet break, and so lower when it passes the radio later, than in the ISM case. A lower ν_a gives an earlier passage post-jet and so an earlier start to the post-jet decay.

There are also two $r^{-2.5}$ fits to the GRB 970508 data in Table 8.3. The best model in terms of the goodness of the fit has an unphysically high $\epsilon_B = 100\%$, which would indicate that all the shock energy was in the magnetic field, despite the need for shock kinetic energy and shocked electrons. This best-fit model can be seen in Figure 8.2, where it is constrasted with the alternative model, the best-fit with reasonable parameters. The alternative is systematically below the late radio data and is a marginal fit. In the alternative model, ν_a and ν_m pass the radio too quickly and the model's decay above these frequencies is too steep. The unphysically high ϵ_B comes from the need to make ν_a and ν_m initially high (see Table 8.1). They then pass through the radio later in the best fit.

However, the best-fit model is not a good descriptor of the X-ray flux level, so neither $r^{-2.5}$ model is a good fit across the entire GRB 970508 broadband data set. Figure 8.2 also compares the fits in the X-ray, where the best model is clearly below the X-ray flux. This is because the synchrotron flux is low at high frequencies for $r^{-2.5}$; the alternative model has a higher density and makes up the difference with IC flux. The synchrotron flux is low because the peak flux drops in time for models where the shock hits a progressively more rarified medium. To match the peak level at later times, the model peak is high early on and requires a steeper spectral index to connect the peak to the optical (see Table 8.3 values of p), which continues through the X-ray. The difference in spectral index between the optical and the X-ray makes the flux lower in this model by a factor of about two.

The data for well-sampled broadband cases does not accomodate very rarified, blown-out circumburst media with a steep density gradient. Even $r^{-2.5}$ can only produce marginal fits. The model's flexibility can be constrained to exclude such extremely steep density gradients.

8.2 Plowing into a Dense Medium: $n \propto r^S$; $S \gg 1$

As mentioned above, for an increasing density gradient the shock slows rapidly compared to the constant density case, and the resulting changes in n seen by the shock are gradual. As a result, 970508 and 000926 can both be fit with $S \approx 10$ (Table 8.3).

The primary change in the fits to GRB 000926 is a more rapid non-relativistic transition. The fits are even slightly *better* than the ISM $S = 0$ case through $S = 10$ (good fits shown to GRB 000926 in Figure 8.3 and to GRB 970508 in Figure 8.5). As long as the data up to times $t \approx t_{jet}$ can be modelled, the behaviour post-jet will be quite like the ISM case until the non-relativistic transition, where the decay shallows. This shallower decay is the key to the improved fit. It occurs at late times when the afterglow can only be observed in the radio. We note that typically the radio decay is a bit shallower than the optical decay so the earlier transition fits a bit better. This is not a big constraint on the density scaling; our treatment of the NR transition (a sharp break, at an estimated point) is approximate, so we expect some uncertainty in the calculation for t_{NR}. In addition, there are other possible causes for the shallow radio flux, as any effect that increases the peak flux, such as an increasing energy or density, will flatten the radio decay.

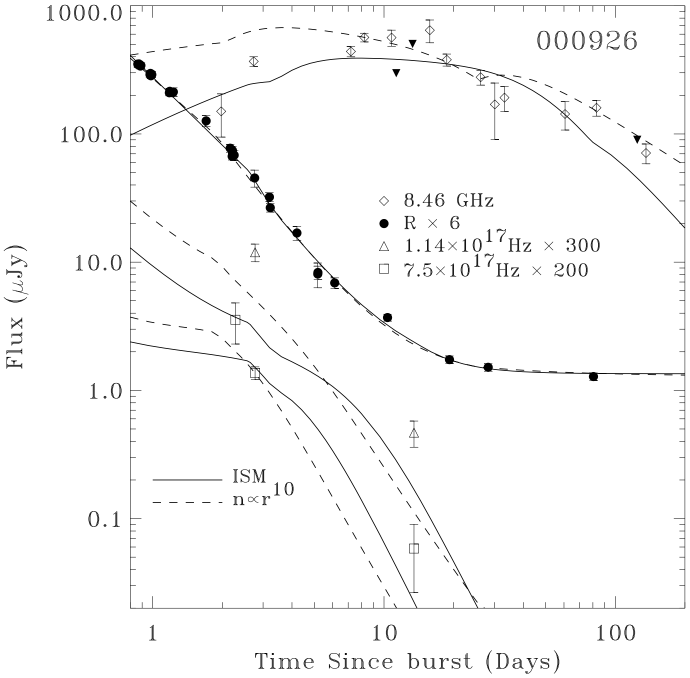

Figure 8.3: GRB 000926, comparison of the best fit to ISM and $n \propto r^{10}$ profiles, with X-ray and representative radio and optical data (see Table 8.3). Data that aren't $2\,\sigma$ significant are given as $2\,\sigma$ upper limits (filled triangles). Both fits are reasonable as a general description of the X-ray flux, although the X-ray region's spectral slope is not well reproduced. The jet break has dropped from 2.6 to 1.9 days in the $n \propto r^{10}$ fit. The fits, however, are nearly identical in the optical (at early times it is above the cooling frequency ν_c and thus insensitive to density changes, and the post-jet behaviour until the non-relativistic transition does not depend on the density gradient). The $n \propto r^{10}$ fit has an earlier estimated non-relativistic transition, at 26 days instead of 79. That decay is shallower than the post-jet rate. Typically the radio decay is a bit shallower than the optical decay so the earlier transition fits a bit better. The early radio rise is a bit above the data. The fit is insensitive to this; the model's estimated uncertainty due to interstellar scintillation at 8.46 GHz is 46% initially (subsiding around twenty days).

At $S = 12$, we begin to see some worsening of the fit to GRB 000926. It is not as evident in the χ^2 in Table 8.3 as in Figure 8.4, which shows that the early radio flux is systematically overestimated in the model. This does not affect the χ^2 greatly due to the incorporation of ISS into the model's uncertainty (see §3 for details). The model is considered uncertain in the early radio due to the possibility the observations may be affected by scintillation. However, the expected result is to see fluctuations around the model, not values consistently below it.

The $S = 12$ fit with the best fit statistic (see Table 8.3) consistently overestimates the early radio flux, as shown in Figure 8.4. The fit places ν_a just below the high radio (8.46 GHz) at t_{jet}. The peak is then at t_{jet}; the flux density above ν_a declines post-jet for both fast and slow cooling. As t_{jet} is set in the optical, this is too early for the radio peak and the model flux at (and before) the peak is set too high in order for the post-jet decline to hit the data after its actual peak somewhat later.

A higher ν_a ought to counteract this problem, but it is not without trouble of its own. The other $S = 12$ model presented, the "alternative" one (with $\chi^2 = 160$ in Table 8.3), presents the best case found with a higher ν_a, about as high around two days as the ISM case. The flux density below ν_a during the early fast cooling is proportional to $t^{4/(4+s)}$ ($= t^1$ for the ISM case), but only $t^{0.25}$ for $S = 12$. This slower rise would again place the model a bit high over the first few radio data points. The model adjusts by pushing t_{jet} a bit lower, to 1.6 days instead of 2.2 or 2.5. This is enough to produce a fit that is not optimal in the optical, as seen in Figure 8.4, where the longer post-jet decay of this model is being compensated by a shallower p.

The fit for GRB 000926 at $S = 12$ is becoming marginal. Due to the slow changes in the model with increasing S, the breakdown of the fit is gradual. It is difficult ot determine a precise point at which the model no longer describes the data. However, the data can accomodate a very steep density gradient, at least $S > 10$.

We find for GRB 970508 that good fits are possible for $S > 10$. Figure 8.5 demonstrates a reasonable fit at $S = 12.5$. The data without a jet break are not as sensitive to a steepening density field. Thus we decided that pushing to some extreme value of S (near 100, or 1000) to discover whether the model would "break down" and be unable to fit the data was of limited value. A *very* steep gradient can be accomodated, and we examine the model as $S \to \infty$.

First, we consider what will occur to modelled jet breaks such as that seen in GRB 000926. The denser the medium, the quicker the transition t_{NR}. We find (see Table 8.3) that as S increases, even for the same t_{jet}, t_{NR} decreases. The jet opening angle θ increases. This is because the amount of

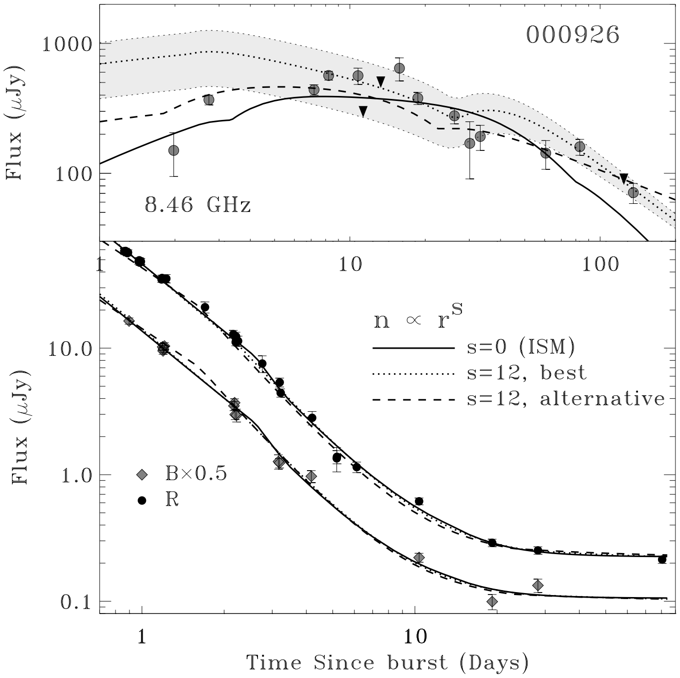

Figure 8.4: GRB 000926, 8.46 GHz, B, and R bands comparing the best fits to ISM-like and $n \propto r^{12}$ profiles. Two models are presented for r^{12}: "best" is the model in Table 8.3 with $\chi^2 = 141$, with a later jet break than the "alternative" fit with $\chi^2 = 160$. The radio envelope shows the estimated model uncertainties from scintillation (ISS) for one case; the same fractional uncertainty was used for all, and data that is not $2\,\sigma$ significant is presented as $2\,\sigma$ upper limits (triangles). The best r^{12} fit is systematically above the early radio data (uncertainty due to ISS reduces the impact on χ^2, but ISS would not produce a systematic deviation); it places the self-absorption frequency ν_a just in/below the radio at t_{jet} and the decay begins post-jet above ν_a. The optical requires the early t_{jet}, which sets the time of the radio peak; the flux is above the early radio to match the radio during its decline. We searched for another fit with higher ν_a; the best is the alternative $S = 12$ fit. It is a better radio fit, but worse in the optical. With this assumption, the model rises slowly and goes above the earliest radio points in order to match the peak. This places t_{jet} a bit lower, giving a fit with a shallower post-jet decay that is not optimal for the optical. All the 000926 fits become marginal assuming an S of about 12; it is of little value to pin a specific assumed S where the model fully breaks down.

matter swept up in the density gradient is reflected in the dependence of t_{jet} on S.

The equation for t_{jet} has

$$t_{jet} \propto (1+z)\,(E_i/n_i)^{1/(3+s)}\,\theta^{(8+2s)/(3+s)}\,(17+4s)^{1/(3+s)}\,(4+s)^{-1}\,.$$

For $S \gg 1$, the density at the reference radius and the energy no longer affect the result, nor does the factor of $(17+4s)$. The limit is $t_{jet} \propto \theta^2 s^{-1}$. Eventually, for a particular required t_{jet}, θ_{jet} will become large and nearly isotropic. Then the non-relativistic transition t_{NR} will follow so quickly that its shallowing would be seen right after t_{jet}, which does not occur in the optical data. We estimate that to keep $t_{NR} >$ one week for a t_{jet} of two days requires for GRB 000926 $S \lesssim 100$.

Eventually, the required θ_{jet} for a particular t_{jet} becomes isotropic and only the non-relativistic transition occurs. We estimate this would occur at $S \approx 600$ for GRB 000926. Beyond this point, the non-relativistic transition occurs earlier and earlier and one should consider a non-relativistic model. This clearly does not correspond to the data.

We consider a similar effect in isotropic models for GRB 970508. The equation for t_{jet} then corresponds, with $\theta = 1$, to the non-relativistic transition. The inevitable decrease with S leads to a decrease in t_{NR}. To keep $t_{NR} > 10$ days, and so keep the modelled transition from being apparent in the optical decay where none is seen in the data, requires an estimated $S \lesssim 70$.

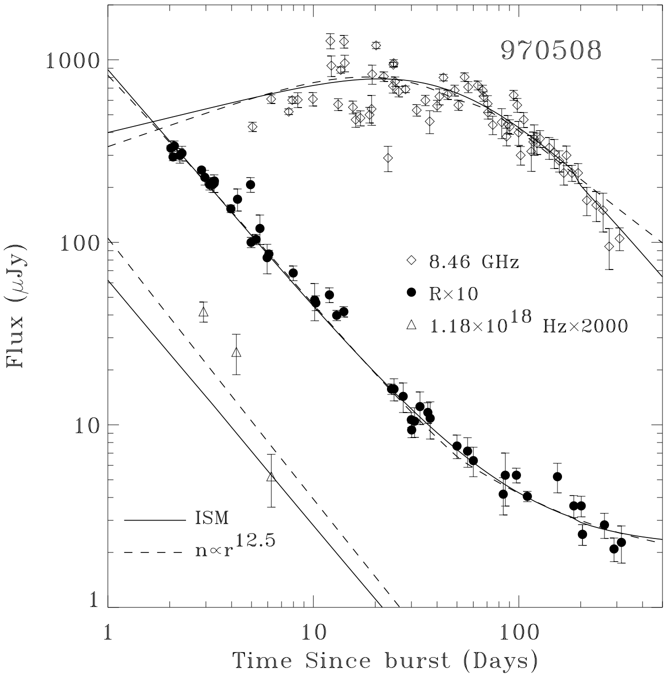

Figure 8.5: GRB 970508, comparison of the best fits to ISM and $n \propto r^{12.5}$ profiles (see Table 8.3, §8), with X-ray and representative radio and optical data (selection detailed in §4.3). Without a jet break, the data is not very sensitive to an increasing density gradient; both fits provide a reasonable description to the general features of the X-ray flux. The fits are virtually identical in the optical region of the spectrum, as it is above the cooling break ν_c, and so insensitive to the density. The small difference in the X-ray is due to a small difference in the electron energy spectral index p, which becomes a small difference in the synchrotron spectral slope. The radio trend is well-fit. The model's estimated uncertainty due to interstellar scintillation at 8.46 GHz is 59%, subsiding after about four days. The non-relativistic decay is shallower with the steeper density profile, which also gives an earlier transition. This places the $n \propto r^{12.5}$ fit slightly above the last few data points, a small effect compared to the fit difficulties with the data's scatter.

Tables 8.1 and 8.2 give the spectral parameters and the spectral flux densities for the models with $n \propto r^S$. Comparing the time-dependences of spectral parameters and flux densities before the jet and after the non-relativistic transition for $S = 0$ and $S \rightarrow \infty$ gives a few noticeable changes, the strongest being

$$\nu_c(t < t_{jet}) \sim t^{-0.5} \rightarrow t^{-1.5} \quad \text{or} \quad (\nu_a < \nu_c < \nu_m,\ t < t_{jet})\ F_{\nu < \nu_a} \sim t^1 \rightarrow t^0 \,.$$

There are no radical changes in direction (unlike $S < 0$, where ν_c goes from falling to rising pre-jet). The changes in the model behaviour are not dramatic despite the great change in gradient.

As even $S \rightarrow \infty$ is not dramatically different from the ISM model, it is not surprising that very large values of the gradient index S, $S > 10$, can be accommodated by the data. It is only when parameters cannot be shuffled around to put the spectral breaks in the right places, or the model breaks down because it can no longer produce a sufficiently late non-relativistic (or jet) transition that it will cease to provide a good fit. We have shown above that it can take $S \sim 100$ to reach this point.

8.3 Density Profile Constraints

In summary, while the data may sometimes accommodate an r^{-2} CBM, it does not fit an extreme blown-out density $r^{-2.5}$. However, a shock plowing into a denser region cannot be easily excluded by the data. This is not the same as a sudden jump in density, but a gradual, continuous increase $n \propto r^S$ $S \gg 1$, which is not entirely realistic, but may roughly mimic a dense but not sharp shell of material (perhaps ejecta from the progenitor).

By examining the basic model ($S = 0$) and the reasonable fits to steep density profiles ($S \approx 10$) presented in Table 8.3, we determine that changes in the assumed density profile will greatly affect the parameters required to fit the data. Several parameters change only by small fractions for both events (energy E, electron energy distribution index p, and collimation θ); some may change by factors of ≈ 2 (electron energy fraction ϵ_e) or even ≈ 10 (the magnetic energy fraction ϵ_B). In these latter cases, the model uncertainty far dominates the apparent (statistical) parameter uncertainties once model assumptions are adopted.

We conclude that the fireball model data fits are not very sensitive to *increasing* density gradients, and that such gradients may strongly affect the inferred physical parameters of the fireball. The assumed density profile may strongly affect the inferred microphysical parameters.

Chapter 9

Improving Observational Constraints

In previous chapters (7 & 8), we found good fits to four events under different assumptions ($\epsilon_B \propto \gamma^{-1}$, γ^{+1}; $n \propto r^{-1}$, or r^S with $S \sim 10$), as reasonable as the good fits derived from the basic model of Chapter 3 (§3.1). Given the multiple suitable fits, in this chapter we examine what improvements to the data sets could resolve the degeneracies. We look to guide future observations of burst afterglows so that data sets can better constrain the model. The following discussion is largely taken from our work presented in Yost *et al.* (2003).

The data tolerates the widely differing assumptions (enumerated above) concerning the evolution of the magnetic energy fraction and the circumburst density profile, since the fits need only match up with data over a limited range of frequencies and times, and there are significant degeneracies between parameters and model assumptions. For example, the decay rate depends upon the spectral index p of the electron energy distribution as well as the assumed $n(r)$ or $\epsilon_B(\gamma)$. A change in model assumptions can be offset in a fit to data by changes in physical parameters; yet the resulting models will not have precisely the same evolution and will diverge in spectral and temporal regions far from the data.

We cross-compared different good fits to each event under the various model assumptions concerning the evolution of the magnetic energy, and the circumburst density profile, with the best fits to the basic model of §3.1. For each comparison, spectra from 0.01 to 300 days were analyzed to determine where in frequency and time the models could be distinguished, for realistic expectations

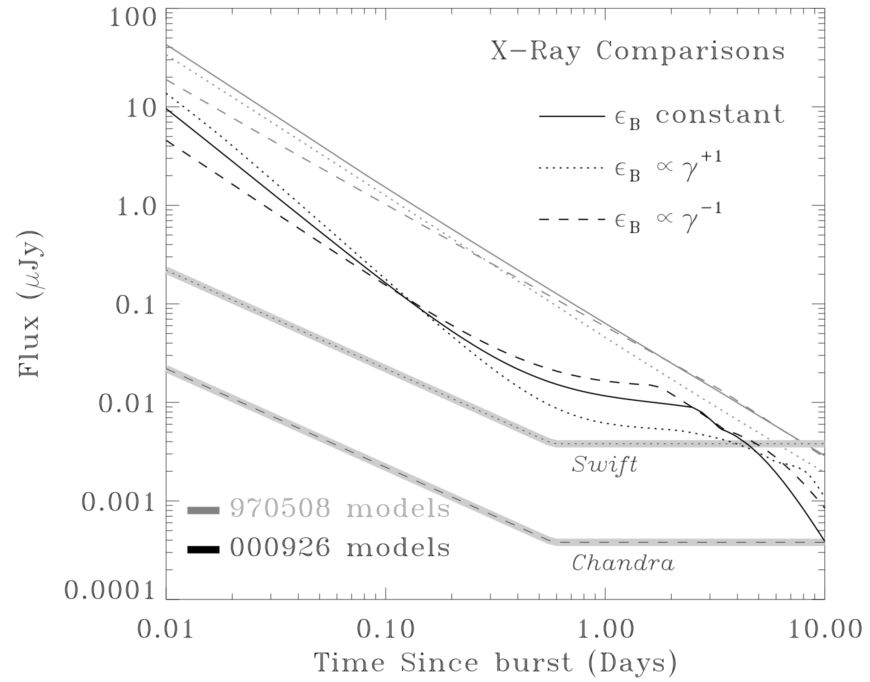

Figure 9.1: Comparison of model X-ray light curves for several equally acceptable model fits. The light curves are for a frequency of 6×10^{17}Hz (nominal for *Swift*), and show the good fits for GRBs 970508 and 000926 with the basic model as well as with the assumption that the magnetic energy fraction is proportional to $\gamma^{\pm 1}$. The pale lines with dotted and dashed centers show approximate sensitivity limits for *Swift* and *Chandra* respectively. These are the fluxes for the instruments to receive 100 1–10 keV photons during the time since the event, from a source with a ν^{-1} flux density spectrum. The sensitivity limits flatten out at 50 ksec, as longer integrations are not expected. While the models are close around the times of the X-ray observations ($\sim$ days), they diverge at early times, with a spread of several μJy at 0.01–0.03 days. Moreover, in the case of 000926, there is significant IC upscattered flux, which gives different peak passage times under the differing model assumptions. While *Chandra* cannot rapidly observe events, *Swift* is intended to observe a burst position in the X-ray within approximately a minute. *Swift*'s early light curves should be densely sampled and sensitive enough to determine if we are modelling the X-ray flux, including the upscattered IC photons, correctly.

concerning the sensitivity of the observations. The fitted models diverge in spectral and temporal regions far from the data, as shown in Figures 9.1, 9.2, and 9.3. These figures highlight the most promising areas for improved constraints: more sensitive X-ray and submillimeter observations, taken over a larger time range.

X-ray light curves of some of the acceptable fits are extended to early times for comparison in Figure 9.1. Sets of acceptable fits for two events are shown to demonstrate that the fits in all events diverge by factors of up to three at early times; fluxes of equally acceptable fits may be 3 μJy or 10 μJy at 0.01–0.03 days. The sensitivity of *INTEGRAL*'s instruments would not be able to distinguish them, but more sensitive X-ray instruments on later γ-ray missions such as *Swift* may. Figure 9.1 includes a case with an upscattered IC flux component, whose peak passage timing gives different curvatures to the light curves. X-ray light curves densely sampled over a longer temporal baseline will show any IC peak passage; multi-frequency X-ray bins could show the IC peak's addition to the synchrotron spectrum. This would break any degeneracy between synchrotron or IC as the source of X-ray flux. Under some changed model assumptions (such as $\epsilon_B \propto \gamma^x$; $x > 0$, see Figure 7.4) a fit may be pushed to lower densities and IC flux; the discrepancy if the X-ray is indeed dominated by IC flux would become obvious with improved data sets. Constraining the timing and level of any IC flux peak in the X-ray would also provide a consistency check on the model assumptions as the IC flux is calculated self-consistently from the synchrotron model's parameters and their underlying assumptions, as detailed in §3.4.

Observations of the broadband peak at frequencies greater than the radio will offer significant new information, confirming such results as the "peak flux cascades" fit by jet breaks in the 980703 and 980329 events (see §4.4, §4.5). While the cascade is indicated, the precise rate is not well determined by the small time and frequency baseline for peak observations. As seen in the examples of Figure 9.3, the data allows considerable variation in model assumptions that affect the rate of change of the peak flux. There are a variety of submillimeter peak levels in acceptable fits that subsequently match the radio peak. The peak can rise or fall for a variety of reasons (energy losses, a jet break, $n(r)$, $\epsilon_B(\gamma)$), with details such as the rate of change varying depending upon the cause. Much of this information is lacking as the peak is in the mid-IR or submillimeter for most of the observable afterglow period, from about a day to a month. A lack of sensitivity in present submillimeter instruments, which can take a substantial part of a day to reach their confusion limit of 1 mJy, has prevented submillimeter observations of the afterglow from providing any significant information about the spectral peak. Matching the peak solely to its passage through the radio leads to models diverging in submillimeter peak height by up to 10 mJy at fractions of a day ($\approx$ mJy in the mid-IR). The new, sensitive IR detectors of the *SIRTF* satellite are not of use for observing transients; the telescope positioning constraints do not allow for rapid overrides. However, improved

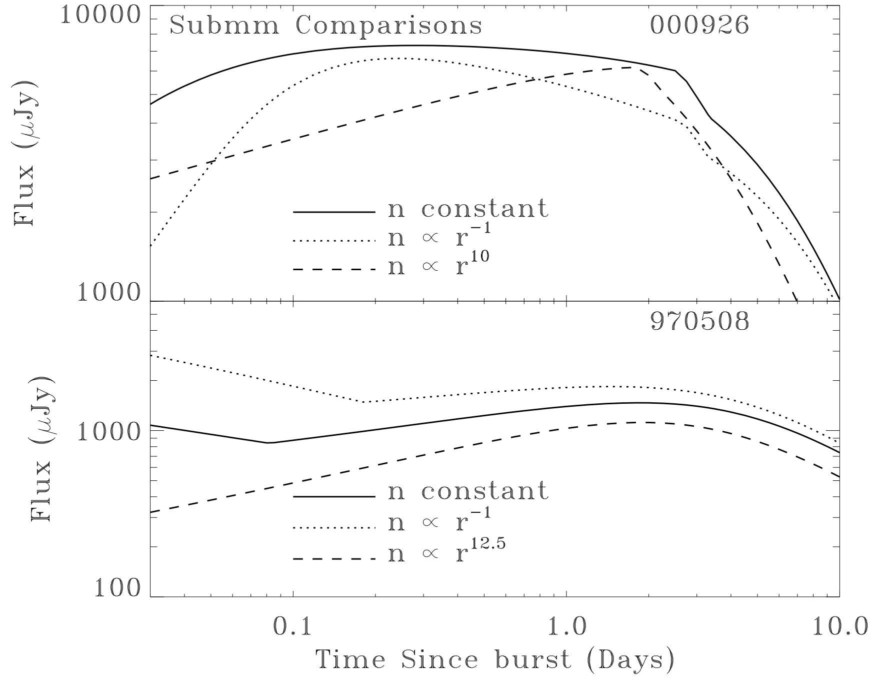

Figure 9.2: Comparison of model submillimeter light curves for several equally acceptable model fits. The light curves are for a frequency of 320 GHz (nominal center of an *ALMA* atmospheric window), and show the good fits for GRBs 970508 and 000926 with the basic model as well as with the assumption that the density is proportional to r^{-1} and r^S; $S \approx 10$. Present sensitivities of $\approx$1 mJy, attainable only on timescales $\sim$ day, are insufficient to distinguish between the variety of peak levels that subsequently match the radio peak. This spread in peak levels is due to differing peak behaviours (rising or falling) with details dependent upon factors such as energy losses, jet break, $n(r)$, or $\epsilon_B(\gamma)$. The early model divergences due to density profile are of $\sim$ 3 mJy; models with differing magnetic energy fraction ($\epsilon_B(\gamma)$) diverge by up to ten mJy. These early differences could be resolved with improved submillimeter instruments soon. The *ALMA* array, to be partially on-line by 2006 and completed by 2010, is expected to give fractional mJy sensitivity in a few minutes, which could distinguish amongst these models.

submillimeter instruments are expected to reach appropriate sensitivities soon. The *ALMA* array, to be partially on-line by 2006 and completed by 2010, is expected to give fractional mJy sensitivity in a few minutes. Its observations could seriously constrain the peak's behaviour.

In the case of model assumptions where the temporal decline is faster for the electron energy index p, a new fit may produce a flatter index p. This will also shallow the model spectrum in some regions (at high frequencies $f_\nu \propto \nu^{-(p-1)/2}$ or $\nu^{-p/2}$), generally including the optical frequencies. This can be offset by an increase in host extinction, steepening the optical spectral index, as demonstrated in Figure 7.4. The fit becomes unacceptable when the combination is no longer able to produce appropriate spectral indices both in the optical and from the optical to the X-ray. NIR data is less

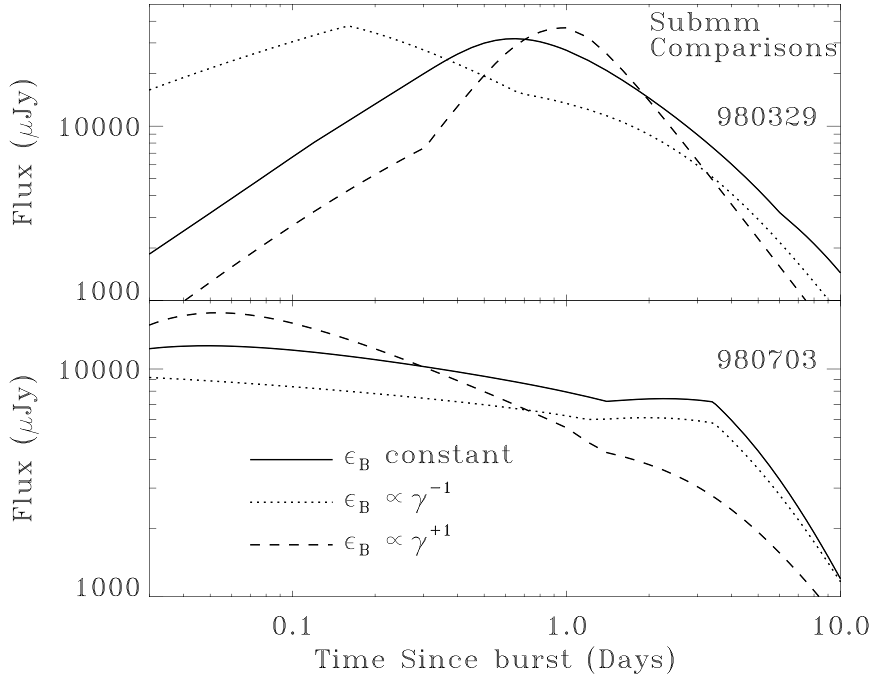

Figure 9.3: Comparison of model submillimeter light curves for several equally acceptable model fits. The light curves are for a frequency of 320 GHz (nominal center of an *ALMA* atmospheric window), and show the good fits for GRBs 980329 and 980703 with the basic model as well as with the assumption that the magnetic energy is proportional to γ^{-1}, γ^{+1}. The data for these events show a cascade in peak flux values across the radio. A cascade occurs with a variety of model assumptions such as a jet break, ϵ_B(t), $n(r)$, or $E(t)$. With only radio peak measurements, several such models can fit the data, although they will differ in their peaks at higher frequency. Present sensitivities of ≈1 mJy, attainable only on timescales ∼ day, are insufficient to distinguish between the variety of peak levels that subsequently match the radio peak. Future instruments such as *ALMA* will be able to reach fractional mJy sensitivities within a few minutes; such observations would be able to distinguish between the models shown here before approximately one week post-burst.

affected by extinction than the optical; more data at those frequencies will better measure the level of host extinction in the optical. Then the remaining spectral requirements constrain p and allowed model assumptions can be better distinguished by their temporal behaviours for that p.

Finally, earlier optical observations are becoming available now such as GRB 021004 (Fox, 2002), or GRB 021211 (Fox & Price, 2002), and will be of some use. However, at such early times the dominant optical emission should not be due to the synchrotron emission from a forward shock into the external medium; reverse shocks (as likely seen in the 990123 optical flash, Sari & Piran, 1999; Mészáros & Rees, 1999) and internal shocks may produce the early optical flux. There is evidence in the data from GRB 021004 that the forward shock dominates only after ≈ 0.1 days, and the rise of its peak may be masked by the reverse shock (Kobayashi & Zhang, 2003; Uemura *et al.*, 2003). This will allow further constraints upon the fireball model, but not necessarily to the same parameters as in our model effort. Early observations dominated by the reverse shock may constrain the thickness of the flow of ejecta rather than the forward shock parameters fitted in the models presented here.

We have shown the divergence of reasonable models beyond the presentobservations. With new instruments, densely sampled X-ray light curves and precise observations of the spectral peak above the radio will become available. In the future, such new information can better measure which possible model assumptions, as well as fit parameters, are compatible with data sets, and which may be ruled out.

Chapter 10

Conclusions

This thesis has been undertaken to better understand the physical parameters and environs of GRBs, based upon the required parameter values that produce reasonable fits to the fireball model. We have discovered degeneracies in the model fits with basic assumptions in some cases, and that the basic fireball model does not fit several event data sets. Given these difficulties, we have undertaken an examination of the extent to which the model's underlying assumptions are themselves constrained. We were interested in what, if anything, the data requires concerning the evolution of the magnetic energy and the surrounding density profile. We modified these model assumptions and produced new fits to the cases for which the basic model assumptions provided a good fit. We demonstrated how far the assumptions can change and still produce reasonable fits to those events.

We determined good fits for four well-studied bursts with extensive radio through X-ray afterglow data sets to a fireball model with simple assumptions concerning the microphysics and environment. We find a range of reasonable environmental and geometrical parameters. We find all four fit best with a constant density medium, one with a value similar to the Milky Way's ISM density, $n \approx 0.2$ cm^{-3}, the other three typical of diffuse clouds $n \approx 20$ cm^{-3}. Their kinetic energies are comparable to the total GRB γ-ray energy. The collimation varies from near-isotropy to a half-opening angle, θ, of 0.04 radians.

We also find a striking diversity in the fitted microphysical parameter values, far beyond the statistical uncertainties. The electron energy distribution index varies from $p = 2.1$–2.9 and the magnetic energy fraction varies from 0.2% to 25%. As shock physics should depend merely on shock strength, we investigated whether the spread could be due to model uncertainty, but did not find a set of assumptions which fit the data via universal microphysics parameters.

We allowed changes to be made to the model assumptions: $\epsilon_B \propto \gamma^x$ and independently $n \propto r^S$. We find considerable flexibility in the values of x and S that can still produce reasonable fits: $\epsilon_B \propto \gamma^x$ where $-2 \leq x \leq +1$ and $n \propto r^S$, with $S > -2$ through $S \gg 1$. Moreover, some parameter values change by up to an order of magnitude when the assumptions underlying the model are altered. This is not the case for all parameters. The energy E and electron energy index p tend to change by small fractions, collimation θ and density n may change by factors of a few, and in some cases magnetic and electron energy fractions may change by a factor of about ten. Clearly, even the results of very good fits are not unique and the parameters cannot be taken at face value.

The model assumptions are not strongly constrained by the data sets available to date. With this model uncertainty, the evidence for massive stellar progenitors from other sources (positions within hosts, possible supernova associations, see Mészáros, 2002) is not hard to reconcile with the lack of clear $n \propto r^{-2}$ wind signatures in the best fits. Massive stars may not produce a true r^{-2} profile, or its effect upon the spectrum could be masked by an inaccuracy in other model assumptions.

Finally, we compared the spectral evolution of the range of acceptable fits with differing assumptions to identify observational strategies that would produce better constraints. Two areas are most promising. First, a good fit currently needs only to line up with a small span of time over which X-ray observations are recorded. Thus, the X-ray light curves of the *Swift* satellite, expected to be well-sampled from early times and so extend the time range of X-ray afterglow data, will better constrain the spectral evolution, as well as the IC upscatters of photons to the X-ray band and their consistency with the synchrotron model. Moreover, the peak has only been definitively observed at radio frequencies, passing through the mid-IR and submillimeter during most of the afterglow. New submillimeter instruments such as *ALMA* should increase the reach of direct peak detections. This will constrain the peak flux evolution, which is sensitive to the model assumptions.

Future work investigating further constraints upon model assumptions may be useful. As mentioned in Chapter 6, some resolutions to the fit difficulties of certain events include energy injection, or nonstandard electron energy distributions produced by the shock acceleration (with more than one power law segment). Constraints upon variable energy $E(t)$ (under investigation in the context of events such as 021004, e.g., Heyl & Perna, 2003), in events both with and without odd deviations that suggest an $E(t)$ scenario, will be of importance. The possibility that properties of the electrons could vary with shock strength is also of interest. These interesting properties are particularly the electron energy fraction, parameterized by ϵ_e, or the electron acceleration, parameterized by the power law index p.

Acknowledgements

I almost became a rocket scientist—or at least an astrophysicist whose work relies on sounding rocket payloads. I know the smell of rocket fuel in the morning, and the tension in a bunker during a countdown. In 1996, at the start of graduate school, I joined up with Andrew Lange's research group, to work on an already ongoing project to study nearby edge-on spiral galaxies in the near-infrared. I assisted on two sounding rocket campaigns to get observations of such objects from above the Earth's atmosphere, which would otherwise absorb the light at the wavelengths of interest.

I had the opportunity to learn many things while working under the direction of Jamie Bock, and with our Japanese collaborators, Kazunori Uemizu, then the student of Professor Matsumoto, as well as Kawada-san and Watanabe-san. I am especially grateful for the hospitality of Uemizu-san and Matsumoto-sensei during a visit to ISAS.

Early on, the plan for my graduate career was that once a near-infrared halo was detected, as expected from ground-based observational hints, I would investigate the near-infrared colour index of the halo. Unfortunately, the universe is not always as expected. Any near-infrared haloes are fainter than expected, undetectable by the instrument. As a result, by the end of 1998, it was obvious that there was no viable thesis-worthy project from that point of view.

At this point, Frank Porter, as Physics Option Representative, was invaluable in guiding me through the process of finding a new project, and in my case, a new advisor. I am grateful for the opportunity provided by my advisor, Fiona Harrison, to study a field that did not yet exist when I first entered Caltech.

In my studies of gamma-ray burst afterglows, I have found Re'em Sari to be a great teacher. Along with my advisor, I am grateful for the advice and collaboration of other professors and postdocs working in the Caltech GRB team, particularly Alan Diercks, George Djorgovski, Derek Fox, Dale Frail, Shri Kulkarni, and Dan Reichart.

This work would not be possible without the observational efforts of many, particularly observers within the Caltech GRB team. I am grateful for Alan Diercks' instruction in photometry. I am indebted to my fellow graduate students who have performed observations or reduced data as part of the Caltech GRB effort, especially Edo Berger and Paul Price.

Bibliography

Abbott, D. C. and Conti, P. S. 1987, Ann. Rev. Astr. Ap., 25, 113.

Achterberg, A., Gallant, Y. A., Kirk, J. G., and Guthmann, A. W. 2001, MNRAS, 328, 393.

Akerlof, C. *et al.* 1999, Nature, 398, 400.

Asaoka, I. and Koyama, K. 1990, PASJ, 42, 625.

Atteia, J.-L. *et al.* 1987, ApJS, 64, 305.

Band, D. *et al.* 1993, ApJ, 413, 281.

Barthelmy, S. D., Butterworth, P., Cline, T. L., Gehrels, N., Fishman, G. J., Kouveliotou, C., and Meegan, C. A. 1995, Ap&SS, 231, 235.

Bednarz, J. and Ostrowski, M. 1998, Physical Review Letters, 80, 3911.

Beloborodov, A. M. 2000, ApJ, 539, L25.

Berger, E., Cowie, L. L., Kulkarni, S. R., Frail, D. A., Aussel, H., and Barger, A. J. 2003, ApJ, 588, 99.

Berger, E. *et al.* 2001a, ApJ, 556, 556.

Berger, E. and Frail, D. A. 2001, GCN notice 968.

Berger, E. *et al.* 2002, ApJ, 581, 981.

Berger, E., Kulkarni, S. R., and Frail, D. A. 2001, ApJ, 560, 652.

Berger, E. *et al.* 2000, ApJ, 545, 56.

Berger, E. *et al.* 2001b, GCN notice 1182.

Bessell, M. S. 1979, PASP, 91, 589.

Bessell, M. S. 1990, PASP, 102, 1181.

Bessell, M. S. and Brett, J. M. 1988, PASP, 100, 1134.

Best, P. and Sari, R. 2000, Physics of Fluids, 12, 3029.

Bhattacharya, D. 2001, Bulletin of the Astronomical Society of India, 29, 107.

Björnsson, G., Hjorth, J., Pedersen, K., and Fynbo, J. U. 2002, ApJ, 579, L59.

Blandford, R. D. and McKee, C. F. 1976, Physics of Fluids, 19, 1130.

Blandford, R. D. and Znajek, R. L. 1977, MNRAS, 179, 433.

Bloom, J. S. *et al.* 1998, ApJ, 508, L21.

Bloom, J. S., Frail, D. A., and Sari, R. 2001, AJ, 121, 2879.

Bloom, J. S. *et al.* 1999, ApJ, 518, L1.

Bloom, J. S. *et al.* 2000, GCN notice 661.

Boella, G., Butler, R. C., Perola, G. C., Piro, L., Scarsi, L., and Bleeker, J. A. M. 1997, A&AS, 122, 299.

Bond, H. E. 1997. IAU circular 6654.

Brainerd, J. J. 1992, ApJ, 394, L33.

Bremer, M., Krichbaum, T. P., Galama, T. J., Castro-Tirado, A. J., Frontera, F., Van Paradijs, J., Mirabel, I. F., and Costa, E. 1998, A&A, 332, L13.

Briggs, M. S. *et al.* 1999, ApJ, 524, 82.

Briggs, M. S. *et al.* 1996, ApJ, 459, 40.

Cardelli, J. A., Clayton, G. C., and Mathis, J. S. 1989, ApJ, 345, 245.

Castander, F. J. and Lamb, D. Q. 1999, ApJ, 523, 593.

Castro, S. *et al.* 2000, GCN notice 851.

Castro-Tirado, A. *et al.* 1999, GCN notice 452.

Castro-Tirado, A. J. *et al.* 2001, A&A, 370, 398.

Castro-Tirado, A. J. *et al.* 1999a, Science, 283, 2069.

Castro-Tirado, A. J. *et al.* 1999b, ApJ, 511, L85.

Chary, R. *et al.* 1998, ApJ, 498, L9+.

Chevalier, R. A. 1999, ApJ, 511, 798.

Chevalier, R. A. and Li, Z. 2000, ApJ, 536, 195.

Chevalier, R. A. and Li, Z.-Y. 1999, ApJ, 520, L29.

Coburn, W. and Boggs, S. E. 2003, Nature, 423, 415.

Cohen, E., Piran, T., and Sari, R. 1998, ApJ, 509, 717.

Corbet, R. and Smith, D. 1999, GCN notice 506.

Costa, E. *et al.* 1997a. IAU circular 6649.

Costa, E. *et al.* 1997b, Nature, 387, 783.

Covino, S. *et al.* 1999, A&A, 348.

Dai, Z. G. and Cheng, K. S. 2001, ApJ, 558, L109.

Dai, Z. G. and Lu, T. 1998, MNRAS, 298, 87.

Dai, Z. G. and Lu, T. 1999, ApJ, 519, L155.

Dai, Z. G. and Lu, T. 2001, A&A, 367, 501.

Dai, Z. G. and Lu, T. 2002, ApJ, 565, L87.

Dall, T. *et al.* 2000, GCN notice 804.

di Paola, A., Speziali, R., Antonelli, L. A., Pedichini, F., D'Alessio, F., Israel, G. L., Lorenzetti, D., and Stella, L. 2000, GCN notice 816.

Dickey, J. M. and Lockman, F. J. 1990, Ann. Rev. Astr. Ap., 28, 215.

Djorgovski, S. G., Kulkarni, S. R., Bloom, J. S., and Frail, D. 1999a, GCN notice 289.

Djorgovski, S. G., Kulkarni, S. R., Bloom, J. S., Goodrich, R., Frail, D. A., Piro, L., and Palazzi, E. 1998, ApJ, 508, L17.

Djorgovski, S. G., Kulkarni, S. R., Sievers, J., Frail, D., and Taylor, G. 1998a, GCN notice 41.

Djorgovski, S. G. *et al.* 1998b, GCN notice 139.

Djorgovski, S. G. *et al.* 1999b, GCN notice 481.

Efron, B. 1982, The Jackknife, the Bootstrap and Other Resampling Plans, (Philadelphia: Society for Industrial and Applied Mathematics).

Eichler, D., Livio, M., Piran, T., and Schramm, D. N. 1989, Nature, 340, 126.

Fenimore, E. E., Epstein, R. I., and Ho, C. 1993, A&AS, 97, 59.

Fenimore, E. E. and Galassi, M. 2001, in Gamma-ray Bursts in the Afterglow Era, 393.

Fernie, J. D. 1983, PASP, 95, 782.

Feroci, M. *et al.* 1997, in Proc. SPIE Vol. 3114, EUV, X-Ray, and Gamma-Ray Instrumentation for Astronomy VIII, 186.

Fitzpatrick, E. L. and Massa, D. 1988, ApJ, 328, 734.

Fox, D. W. 2002, GCN notice 1564.

Fox, D. W. and Price, P. A. 2002, GCN notice 1731.

Frail, D. *et al.* 1999, GCN notice 451.

Frail, D. A. *et al.* 2000, ApJ, 538, L129.

Frail, D. A. *et al.* 2002, ApJ, 565, 829.

Frail, D. A. *et al.* 2002, ApJ, 565, 829.

Frail, D. A., Halpern, J. P., Bloom, J. S., Kulkarni, S. R., and Djorgovski, S. G. 1998, GCN notice 128.

Frail, D. A., Kulkarni, S. R., Berger, E., and Wieringa, M. H. 2003a, AJ, 125, 2299.

Frail, D. A. *et al.* 2001, ApJ, 562, L55.

Frail, D. A., Waxman, E., and Kulkarni, S. R. 2000, ApJ, 537, 191.

Frail, D. A. *et al.* 2003b, Submitted to ApJ; astro-ph/0301421.

Fruchter, A., Krolik, J. H., and Rhoads, J. E. 2001, ApJ, 563, 597.

Fruchter, A., Thorsett, S., and Wijers, R. 2000, GCN notice 712.

Fruchter, A. S. 1999, ApJ, 512, L1.

Fruchter, A. S. *et al.* 1999, ApJ, 519, L13.

Fynbo, J. *et al.* 2000, GCN notice 807.

Fynbo, J. U. *et al.* 2001a, A&A, 373, 796.

Fynbo, J. U. *et al.* 2001b, A&A, 369, 373.

Galama, T. J. *et al.* 2000, ApJ, 541, L45.

Galama, T. J. *et al.* 1999, Nature, 398, 394.

Galama, T. J. *et al.* 2003, ApJ, 587, 135.

Galama, T. J. and Wijers, R. A. M. J. 2001, ApJ, 549, L209.

Galama, T. J., Wijers, R. A. M. J., Bremer, M., Groot, P. J., Strom, R. G., Kouveliotou, C., and Van Paradijs, J. 1998, ApJ, 500, L97.

Garcia, M. R. *et al.* 1998, ApJ, 500, L105.

Garnavich, P. M., Jha, S., Pahre, M. A., Stanek, K. Z., Kirshner, R. P., Garcia, M. R., Szentgyorgyi, A. H., and Tonry, J. L. 2000, ApJ, 543, 61.

Garnavich, P. M., Loeb, A., and Stanek, K. Z. 2000, ApJ, 544, L11.

Gaudi, B. S., Granot, J., and Loeb, A. 2001, ApJ, 561, 178.

Ghisellini, G. and Lazzati, D. 1999, MNRAS, 309.

Goodman, J. 1986, ApJ, 308, 47.

Gorosabel, J., Castro-Tirado, A. J., Pedrosa, A., Zapatero-Osorio, M. R., Fernades, A. J. L., Feroci, M., Costa, E., and Frontera, F. 1999, A&A, 347, L31.

Gorosabel, J. *et al.* 2000, GCN notice 803.

Granot, J., Piran, T., and Sari, R. 1999a, ApJ, 513, 679.

Granot, J., Piran, T., and Sari, R. 1999b, ApJ, 527, 236.

Granot, J. and Sari, R. 2002, ApJ, 568, 820.

Groot, P. J. *et al.* 1997. IAU circular 6584.

Guetta, D., Spada, M., and Waxman, E. 2001, ApJ, 557, 399.

Halpern, J. P., Kemp, J., Piran, T., and Bershady, M. A. 1999, ApJ, 517, L105.

Halpern, J. P. *et al.* 2000, ApJ, 543, 697.

Hanlon, L. *et al.* 2000, A&A, 359, 941.

Hanlon, L. *et al.* 1999, A&AS, 138, 459.

Harrison, F. A. *et al.* 1999, ApJ, 523, L121.

Harrison, F. A., Yost, S. A., and Kulkarni, S. R. 2001, GCN notice 1023.

Harrison, F. A. *et al.* 2001, ApJ, 559, 123.

Heise, J. *et al.* 1999. IAU circular 7099.

Henden, A. *et al.* 1999, GCN notice 473.

Henden, A. A. 2001a, GCN notice 961.

Henden, A. A. 2001b, GCN notice 962.

Heyl, J. S. and Perna, R. 2003, ApJ, 586, L13.

Holland, S., Björnsson, G., Hjorth, J., and Thomsen, B. 2000, A&A, 364, 467.

Holland, S. *et al.* 2001, A&A in press; astro-ph/0103058.

Hurley, K. *et al.* 2002, ApJ, 567, 447.

Hurley, K., Cline, T., and Mazets, E. 2000, GCN notice 642.

Hurley, K. *et al.* 2000a, ApJ, 534, L23.

Hurley, K., Mazets, E., Golenetskii, S., and Cline, T. 2000b, GCN notice 801.

In 't Zand, J. J. M. *et al.* 1998, ApJ, 505, L119.

In't Zand, J. J. M. i. *et al.* 2001, ApJ, 559, 710.

Jaunsen, A. O. *et al.* 2003, A&A, 402, 125.

Jaunsen, A. O. *et al.* 2001, ApJ, 546, 127.

Jensen, B. L. *et al.* 2001, A&A, 370, 909.

Jha, S. *et al.* 2001, ApJ, 554, L155.

Kassin, S. 1999, GCN notice 494.

Katz, J. I. 1994, ApJ, 432, L107.

Kawai, N. *et al.* 1999, A&AS, 138, 563.

Kippen, R. M. *et al.* 1998, GCN notice 143.

Kirk, J. G. and Duffy, P. 1999, Journal of Physics G Nuclear Physics, 25, 163.

Kirk, J. G., Guthmann, A. W., Gallant, Y. A., and Achterberg, A. 2000, ApJ, 542, 235.

Klebesadel, R. W., Strong, I. B., and Olson, R. A. 1973, ApJ, 182, L85.

Klose, S. 1998, GCN notice 43.

Klose, S. *et al.* 2000, GCN notice 645.

Kobayashi, S. and Sari, R. 2001, ApJ, 551, 934.

Kobayashi, S. and Zhang, B. 2003, ApJ, 582, L75.

Kouveliotou, C., Meegan, C. A., Fishman, G. J., Bhat, N. P., Briggs, M. S., Koshut, T. M., Paciesas, W. S., and Pendleton, G. N. 1993, ApJ, 413, 101.

Koyama, K., Petre, R., Gotthelf, E. V., Hwang, U., Matsuura, M., Ozaki, M., and Holt, S. S. 1995, Nature, 378, 255.

Krolik, J. H. and Pier, E. A. 1991, ApJ, 373, 277.

Kulkarni, S. R. *et al.* 1999a, Nature, 398, 389.

Kulkarni, S. R. *et al.* 1999b, ApJ, 522, L97.

Kumar, P. and Panaitescu, A. 2000, ApJ, 541, L51.

Kumar, P. and Piran, T. 2000, ApJ, 532, 286.

Kuulkers, E. *et al.* 2000, ApJ, 538, 638.

Lamb, D. Q., Castander, F. J., and Reichart, D. E. 1999, A&AS, 138, 479.

Lee, B. C. *et al.* 2001, ApJ, 561, 183.

Leibowitz, E. M., Giveon, U., Bilenko, B., Ofek, E., and Lipkin, Y. 1999, GCN notice 499.

Levine, A., Morgan, E., and Muno, M. 1998. IAU circular 6966.

Li, Z. and Chevalier, R. A. 2001a, ApJ, 551, 940.

Li, Z. and Chevalier, R. A. 2001b, ApJ, 551, 940.

Lyutikov, M., Pariev, V., and Blandford, R. 2003, astro-ph/0305410.

Mészáros, P. 2002, Ann. Rev. Astr. Ap., 40, 137.

MacFadyen, A. I. and Woosley, S. E. 1999, ApJ, 524, 262.

Masetti, N. *et al.* 2000, A&A, 359, L23.

Masetti, N. *et al.* 2001, A&A, 374, 382.

Mattox, J. 1999, GCN notice 487.

McDowell, J., Kilgard, R., Garnavich, P. M., Stanek, K. Z., and Jha, S. 2001, GCN 963.

Medvedev, M. V. and Loeb, A. 1999, ApJ, 526, 697.

Meegan, C. *et al.* 1992, Nature, 355, 143.

Mészáros, P. and Rees, M. J. 1997, ApJ, 482, L29.

Mészáros, P. and Rees, M. J. 1999, MNRAS, 306, L39.

Mészáros, P., Rees, M. J., and Wijers, R. A. M. J. 1998, ApJ, 499, 301.

Metzger, M. R., Djorgovski, S. G., Kulkarni, S. R., Steidel, C. C., Adelberger, K. L., Frail, D. A., Costa, E., and Fronterra, F. 1997, Nature, 387, 879.

Mukai, K. 1993, Legacy, 3, 21.

Nakar, E., Piran, T., and Granot, J. 2003, New Astronomy, 8, 495.

Narayan, R. 1992, Phil. Trans. Roy. Soc. London, Series A, 341, 151.

Paciesas, W. S. *et al.* 1999, Astrophys. J. Supp. Series, 122, 465.

Paczyński, B. 1998, ApJ, 494, L45.

Paczyński, B. and Rhoads, J. 1993, ApJ, 418, L5.

Palazzi, E. *et al.* 1998, A&A, 336, L95.

Panaitescu, A. 2001, ApJ, 556, 1002.

Panaitescu, A. and Kumar, P. 2001a, ApJ, 560, L49.

Panaitescu, A. and Kumar, P. 2001b, ApJ, 554, 667.

Panaitescu, A. and Kumar, P. 2002, ApJ, 571, 779.

Panaitescu, A., Mészáros, P., and Rees, M. J. 1998, ApJ, 503, 314.

Pelletier, G. and Marcowith, A. 1998, ApJ, 502, 598.

Pian, E. *et al.* 2001, A&A, 372, 456.

Piro, L. 1999, GCN notice 311.

Piro, L., Garmire, G., Garcia, M., Marshall, F., and keshima, T. T. 1999, GCN notice 500.

Piro, L. *et al.* 2001, ApJ, 558, 442.

Piro, L. *et al.* 1998, A&A, 331, L41.

Predehl, P. and Schmitt, J. H. M. M. 1995, A&A, 293, 889.

Press, W. H., Flannery, B. P., Teukolsky, S. A., and Vetterling, W. T. 1988. Numerical Recipes in C, chapter 10.5. Cambridge University Press, New York, 1st edition.

Price, P. A. *et al.* 2002a, ApJ, 573, 85.

Price, P. A. *et al.* 2002b, ApJ, 572, L51.

Price, P. A. *et al.* 2001, ApJ, 549, L7.

Price, P. A. *et al.* 2002, ApJ, submitted, astro-ph 0207187.

Ramirez-Ruiz, E., Dray, L. M., Madau, P., and Tout, C. A. 2001, MNRAS, 327, 829.

Reichart, D. E. 2001, ApJ, 553, 235.

Reichart, D. E. 2001, ApJ, in press; astro-ph/0107546.

Reichart, D. E. *et al.* 1999, ApJ, 517, 692.

Rhoads, J. E. 1997, ApJ, 487, L1.

Rhoads, J. E. 1999, ApJ, 525, 737.

Rhoads, J. E. and Fruchter, A. S. 2001, ApJ, 546, 117.

Rossi, E. and Rees, M. J. 2003, MNRAS, 339, 881.

Ruderman, M. 1975, New York Academy of Sciences Annals, 262, 164.

Rybicki, G. B. and Lightman, A. P. 1979, Radiative processes in astrophysics, (New York: Wiley-Interscience).

Sagar, R., Mohan, V., Pandey, S. B., Pandey, A. K., Stalin, C. S., and Castro Tirado, A. J. 2000, Bulletin of the Astronomical Society of India, 28, 499.

Sagar, R. *et al.* 2000, basi, 28, 15. astro-ph/0003257.

Sari, R. 1997, ApJ, 489, L37.

Sari, R. 1999, ApJ, 524, L43.

Sari, R. and Esin, A. A. 2001, ApJ, 548, 787.

Sari, R. and Mészáros, P. 2000, ApJ, 535, L33.

Sari, R. and Piran, T. 1999, ApJ, 517, L109.

Sari, R., Piran, T., and Halpern, J. P. 1999, ApJ, 519, L17.

Sari, R., Piran, T., and Narayan, R. 1998, ApJ, 497, L17.

Schaefer, B. E. 1999, GCN notice 517.

Schlegel, D. J., Finkbeiner, D. P., and Davis, M. 1998, ApJ, 500, 525.

Smith, I. A. *et al.* 1999, A&A, 347, 92.

Sokolov, V. V. *et al.* 2001, A&A, 372, 438.

Sokolov, V. V., Kopylov, A. I., Zharikov, S. V., Feroci, M., Nicastro, L., and Palazzi, E. 1998, A&A, 334, 117.

Spada, M., Panaitescu, A., and Mészáros, P. 2000, ApJ, 537, 824.

Stanek, K. Z. *et al.* 2001, ApJ, 563, 592.

Stanek, K. Z., Garnavich, P. M., Kaluzny, J., Pych, W., and Thompson, I. 1999, ApJ, 522, L39.

Stanek, K. Z. *et al.* 2003, ApJ, 591, L17.

Strong, I. B., Klebesadel, R. W., and Evans, W. D. 1975, New York Academy of Sciences Annals, 262, 145.

Takeshima, T., Markwardt, C., Marshall, F., and an d R. M. Kippen, T. G. 1999, GCN notice 478.

Taylor, G. B., Beasley, A. J., Frail, D. A., and Kulkarni, S. R. 1997. IAU circular 6670.

Taylor, G. B., Frail, D. A., and Kulkarni, S. R. 1998, GCN notice 40.

Taylor, G. B. *et al.* 1998, ApJ, 502, L115.

Taylor, J. H. and Cordes, J. M. 1993, ApJ, 411, 674.

Tokunaga, A. T. 2000. Allen's Astrophysical Quantities, chapter 7. AIP, New York, 4th edition.

Uemura, M., Kato, T., Ishioka, R., and Yamaoka, H. 2003, Accepted for publication in PASJ; astro-ph 0303119.

Uglesich, R., Mirabal, N., Halpern, J., Kassin, S., and Novati, S. 1999, GCN notice 472.

van Paradijs, J., Kouveliotou, C., and Wijers, R. A. M. J. 2000, Ann. Rev. Astr. Ap., 38, 379.

Vanderspek, R., Villaseñor, J., Doty, J., Jernigan, J. G., Levine, A., Monnelly, G., and Ricker, G. R. 1999, A&AS, 138, 565.

Vrba, F. J. *et al.* 2000, ApJ, 528, 254.

Vreeswijk, P., Rol, E., Kouveliotou, C., Pian, E., Castro-Tirado, A., Pedersen, H., and Greiner, J. 1999, GCN notice 492.

Vreeswijk, P. M. *et al.* 1999, ApJ, 523, 171.

Vreeswijk, P. M. *et al.* 1999a, GCN notice 496.

Vreeswijk, P. M. *et al.* 1999b, GCN notice 310.

Vreeswijk, P. M. *et al.* 1999c, GCN notice 324.

Wainscoat, R. J. and Cowie, L. L. 1992, AJ, 103, 332.

Walker, M. A. 1998, MNRAS, 294, 307.

Wang, X. and Loeb, A. 2000, ApJ, 535, 788.

Waxman, E. 1997, ApJ, 489, L33.

Waxman, E. and Draine, B. T. 2000, ApJ, 537, 796.

Weingartner, J. C. and Draine, B. T. 2001, ApJ, 548, 296.

Wijers, R. A. M. J. and Galama, T. J. 1999, ApJ, 523, 177.

Wijers, R. A. M. J., Rees, M. J., and Mészáros, P. 1997, MNRAS, 288, L51.

Wijers, R. A. M. J. *et al.* 1999, ApJ, 523, L33.

Yost, S. A. *et al.* 2002, ApJ, 577, 155.

Yost, S. A., Harrison, F. A., Sari, R., and Frail, D. A. 2003, ApJ, in press; astro-ph/0307056.

Zhang, B. and Mészáros, P. 2001, ApJ, 552, L35.

Zharikov, S. V., Sokolov, V. V., and Baryshev, Y. V. 1998, A&A, 337, 356.

Appendix A

Self-Absorption for All Spectral Break Orderings

This appendix presents calculations for the synchrotron self-absorption frequency, ν_a, for any ordering of spectral break frequencies. In Chapter 3, we presented a calculation of ν_a for the canonical ordering of break frequencies $\nu_a < \nu_m < \nu_c$. The results from this break frequency ordering will be referred to as the *simple self-absorption* case, ν_{as}, in this section. The evolving spectrum may also present other break frequency orderings. We compute the model's self-absorption for these cases by first calculating ν_m, ν_c, and ν_{as}, and then adjusting ν_a accordingly as needed.

The position of the self-absorption frequency is determined by matching the flux density that would be produced by optically thick emission to the emitted optically thin density. At each time, this depends upon the emitted spectrum, and the expected optically thick emission, not upon its evolution over time. The method can be used for any synchrotron spectrum produced from a power law distribution of electron energies, regardless of such assumptions as the environment's density profile.

We consider the following possible orderings, apart from the canonical case:

$\boldsymbol{\nu_{a2}}$**:** $\nu_a < \nu_c < \nu_m$

$\boldsymbol{\nu_{a3}}$**:** $\nu_c < \nu_a < \nu_m$

$\boldsymbol{\nu_{a4}}$**:** $\nu_m < \nu_a < \nu_c$

$\boldsymbol{\nu_{a5}}$**:** $\nu_m < \nu_c < \nu_a$ and $\nu_c < \nu_m < \nu_a$

For the last case, we note that above both ν_m and ν_c, both the electron distribution and the optically thin spectrum have the same form regardless of the relative ordering of the minimum acceleration and cooling break frequencies. This result is evident in Tables 7.2 and 8.2, and can be easily verified by by calculating the high-frequency flux density's dependence upon the break frequencies under both break frequency ordering schemes. Thus the point at which self-absorption is important, when above the other break frequencies, will not depend upon the ordering of ν_m and ν_c; these two orderings can be treated as a single case.

The following calculations show how each of these cases can be determined from ν_{as}, ν_m, and ν_c.

A.1 $\nu_{a2}(\nu_{as}, \nu_m, \nu_c)$

First, we consider the optically thick flux density in the canonical case (see §3.2). This is equated to the spectrum's flux density:

$$2\,\frac{\nu_{as}^2}{c^2}\,\gamma_m m_e c^2\,\gamma\,A = F_{max}\,(\frac{\nu_{as}}{\nu_m})^{1/3} \tag{A.1}$$

where γ is the shock Lorentz factor, and A is the effective area of the shock. This is compared to the result for the ν_{a2} ordering,

$$2\,\frac{\nu_{a2}^2}{c^2}\,\gamma_c m_e c^2\,\gamma\,A = F_{max}\,(\frac{\nu_{a2}}{\nu_c})^{1/3}. \tag{A.2}$$

By division, the two self-absorption cases relate by

$$(\frac{\nu_{as}}{\nu_{a2}})^2\,\frac{\gamma_m}{\gamma_c} = (\frac{\nu_{a2}}{\nu_{as}})^{1/3}\,(\frac{\nu_c}{\nu_m})^{1/3}.$$

Since $\nu(\gamma_e) \propto \gamma_e^2$, the ratio of Lorentz factors can be replaced by the square root of the ratio of break frequencies. The net result is:

$$\nu_{a2} = \nu_{as}\,\sqrt{\frac{\nu_m}{\nu_c}} \tag{A.3}$$

A.2 $\nu_{a3}(\nu_{as}, \nu_m, \nu_c)$

We again relate the optically thick emission to the synchrotron spectrum (as in Equation A.2), and compare this to the equation relating the optically thick simple self-absorption case to the spectrum (as in Equation A.1). The difference is that in this case there are electrons emitting with their peak frequency in the self-absorbed region. The relevant electron energy for the optically thick emission at the self-absorption break ν_{a3} is $\gamma_{a3} m_e c^2$. Here γ_{a3} is the Lorentz factor of the electrons whose peak emission frequency is ν_{a3}, and $\gamma_{a3} \propto \sqrt{\nu_{a3}}$. Thus,

$$2\,\frac{\nu_{a3}^2}{c^2}\,\gamma_{a3} m_e c^2\,\gamma\,A = F_{max}\,(\frac{\nu_{a3}}{\nu_c})^{-1/2} \tag{A.4}$$

where the fluxes are equated above the optically thin peak, where the spectrum is proportional to $\nu^{-1/2}$.

By dividing Equations A.1 and A.4 and substituting the square root of the frequency ratio for the ratio in Lorentz factors, we obtain

$$(\frac{\nu_{a3}}{\nu_{as}})^2\sqrt{\frac{\nu_{a3}}{\nu_m}} = (\frac{\nu_{a3}}{\nu_c})^{-1/2}\,(\frac{\nu_{as}}{\nu_m})^{-1/3}.$$

The net result is:

$$\nu_{a3} = \nu_{as}^{5/9}\nu_m^{5/18}\nu_c^{1/6}. \tag{A.5}$$

A.3 $\nu_{a4}(\nu_{as}, \nu_m, \nu_c)$

We perform the same calculations and comparisons as for ν_{a3}. In this case there are again electrons emitting with their peak frequency in the self-absorbed region, so the Lorentz factor γ_{a4} is relevant. As well, the optically thick flux at ν_{a4} is equated to the spectrum above the optically thin peak, where the spectrum is proportional to $\nu^{(1-p)/2}$. Thus,

$$2\,\frac{\nu_{a4}^2}{c^2}\,\gamma_{a4} m_e c^2\,\gamma\,A = F_{max}\,(\frac{\nu_{a4}}{\nu_m})^{(1-p)/2}. \tag{A.6}$$

By dividing Equations A.1 and A.6 and substituting the square root of the frequency ratio for the ratio in Lorentz factors, we obtain

$$(\frac{\nu_{a4}}{\nu_{as}})^2 \sqrt{\frac{\nu_{a4}}{\nu_m}} = (\frac{\nu_{a4}}{\nu_m})^{(1-p)/2} (\frac{\nu_{as}}{\nu_m})^{-1/3}.$$

The net result is:

$$\nu_{a4} = \nu_{as}^{10/(3p+12)} \nu_m^{(3p+2)/(3p+12)}. \tag{A.7}$$

A.4 $\nu_{a5}(\nu_{as}, \nu_m, \nu_c)$

Finally, we calculate the self-absorption for the case where electrons are emitting in the optically thick region above both the cooling and minimum electron energy breaks, ν_m and ν_c. The flux in this high-frequency region is

$$F_{max} (\frac{\nu_m}{\nu_c})^{-1/2} (\frac{\nu}{\nu_m})^{-p/2}$$

and electrons emit with a peak frequency in the self-absorbed region, so the Lorentz factor γ_{a5} is relevant. Thus,

$$2 \frac{\nu_{a5}^2}{c^2} \gamma_{a5} m_e c^2 \gamma A = F_{max} (\frac{\nu_m}{\nu_c})^{-1/2} (\frac{\nu_{a5}}{\nu_m})^{-p/2}. \tag{A.8}$$

By dividing Equations A.1 and A.8 and substituting the square root of the frequency ratio for the ratio in Lorentz factors, we obtain

$$(\frac{\nu_{a5}}{\nu_{as}})^2 \sqrt{\frac{\nu_{a5}}{\nu_m}} = (\frac{\nu_m}{\nu_c})^{-1/2} (\frac{\nu_{a5}}{\nu_m})^{-p/2} (\frac{\nu_{as}}{\nu_m})^{-1/3}.$$

The net result is:

$$\nu_{a5} = \nu_{as}^{10/3(p+5)} \nu_m^{(3p+2)/3(p+5)} \nu_c^{1/(p+5)}. \tag{A.9}$$

The model code first calculates the simple self-absorption ν_{as} as well as the other break frequencies and the spectral peak. If the result is not the canonical order $\nu_{as} < \nu_m < \nu_c$, the code computes other possible self-absorption breaks (Equations A.2, A.4, A.6, A.8). The appropriate self-absorption frequency is the one that satisfies its required break frequency ordering.

Appendix B

Solving for E(t)

This appendix explains the method we use to calculate radiative corrections to the energy as a function of time. The following deals with the ISM-like density profile case. We performed similar calculations for other density profiles, and for an evolving magnetic energy fraction, which changes $E(t)$.

First, we consider the work of Cohen, Piran & Sari (1998), with a fraction of radiated energy ϵ, thus

$$dE/E = -\epsilon \, dt/t \, .$$

The fraction of radiated energy will depend upon both the fraction of energy imparted to the electrons (ϵ_e) and the fraction of the electron energy that can radiate efficiently, 1 for fast cooling ($\nu_c < \nu_m$), and $(\nu_c/\nu_m)^{(2-p)/2}$ for slow cooling ($\nu_c > \nu_m$).

We calculate ϵ by interpolating between the results of Cohen, Piran & Sari (1998). As $\epsilon_e \to 1$, $\epsilon \to 9/13$. The limit as $\epsilon_e \to 0$ depends upon the density profile; for the ISM-like density profile $\epsilon \to 17\epsilon_e/12$ as $\epsilon_e \to 0$. We interpolate using a simple $ax/(1+bx)$ formula, so that for this case:

$$\epsilon = (17/12) \, \epsilon_e / (1. + 113 \, \epsilon_e / 108) \, . \tag{B.1}$$

Then the solution for $E(t)$ is particularly simple during fast cooling, before $t = t_{cm}$ (when $\nu_c = \nu_m$), and

$$E(t) = E(t_{cm}) (t/t_{cm})^{-\epsilon} \, . \tag{B.2}$$

We scale the energy in the fit model to $E_{cm} = E(t_{cm})$. The calculation then consists of determining the time t_{cm} in the model, and the behaviour of $E(t)$ for $t > t_{cm}$. At that time, the radiative losses depend upon the break frequency ratio ν_c/ν_m. As the ratio grows, they become less important. Therefore for simplicity we consider only the break frequency ratio above t_{cm} as if synchrotron cooling were the only cooling method determining ν_c, regardless of the potential presence of IC cooling.

The break frequency ratio evolves differently before and after the jet break, so the first step after determining ϵ is to calculate consistently t_{cm} and t_{jet}. If $t_{cm} < t_{jet}$, t_{cm} is determined by calculating when the break frequency ratio equals 1 according to Equations 3.4, and adjusting ν_c appropriately for IC cooling effects as we do in §3.4. However, the jet break t_{jet} is energy-dependent and so is only analytically determined when $t_{jet} < t_{cm}$, using Equation B.2 for the energy at t_{jet}. Therefore, we first calculate t_{cm} as if $t_{cm} < t_{jet}$ and t_{jet} as if $t_{cm} > t_{jet}$, and then compare them.

If the calculation for t_{cm} places it above t_{jet}, then t_{jet} is determined and t_{cm} can be analytically adjusted based upon the change due to the break frequency ratio's post-jet behaviour. We calculate this as

$$t_{cm}(t_{jet} < t_{cm}) = t_{cm}(t_{jet} > t_{cm})^{1/D} t_{jet}(t_{cm} > t_{jet})^{(D-1)/D}$$

where $D = 2 + \epsilon/3$. The resulting t_{cm} will remain above t_{jet}.

If the calculation for t_{cm} places it below t_{jet}, it is the correct t_{cm}, and the value of t_{jet} can be adjusted by calculating the difference from the slower energy losses post-t_{cm}. This will always result in t_{jet} remaining above t_{cm}, but requires a numerical calculation to find the time at which the condition for t_{jet} is satisfied. This is done by taking the previous t_{jet} as a first estimation and performing a calculation for t_{jet} with the energy at the estimated t_{jet}, continuing until the results are consistent.

With a consistent set of t_{cm} and t_{jet}, $E(t)$ is then calculated. For $t > t_{cm}$, we solve an equation of the form

$$dE/E = -K\, E^I t^J\, dt/t$$

with a suitable constant prefactor K, energy dependence I, and time dependence J, from the break frequency ratio ν_c/ν_m and p. We note that for times $t > t_{jet}$, we need to include the energy dependence of $t_{jet} \propto E^{1/3}$ to get the correct I and J.

The final result is

$$E(t) = E_{cm}(t/t_{cm})^{-\epsilon}$$

for $t < t_{cm}$. For the case where $t_{jet} < t_{cm}$, when $t > t_{cm} > t_{jet}$

$$E(t) = E_{cm}\,(1 - (2\,\epsilon/3)\,(\,(t/t_{cm})^{(2-p)} - 1)\,)^{-1.5/(p-2)}\ . \tag{B.3}$$

When $t_{jet} > t_{cm}$, there are two segments. First, for $t_{cm} < t < t_{jet}$

$$E(t) = E_{cm}\,(1 - \epsilon\,(\,(t/t_{cm})^{(2-p)/2} - 1)\,)^{2/(2-p)}\ . \tag{B.4}$$

And then finally, for $t_{cm} < t_{jet} < t$, the energy $E_{jet} = E(t_{jet})$ is calculated from Equation B.4 and then

$$E(t) = E_{jet}\,(1 - (2\,\epsilon/3)\,(E_{jet}/E_{cm})^{(p-2)/2}(t_{jet}/t_{cm})^{(2-p)/2}(\,(t/t_{jet})^{(2-p)} - 1\,)\,)^{-1.5/(p-2)}\ . \tag{B.5}$$

These equations for $E(t)$ are also used for the numerical calculation of t_{jet} when $t_{jet} > t_{cm}$.

Appendix C

Fit Code Input Template

The following is a text file used as input to run the fitting code for the fireball forward shock model, implemented in the C executable *fit_cl* with the Perl script *rungrb.pl.* A file of the same structure should be in the directory where the fits are to be performed, and called as *rungrb.pl filename* (or *rungrb.pl*, which prompts for the filename).

```
# Input file to run the C code for the fireball model of afterglows,
# as expressed in grbsubot_cl.c. Run with Perl script "rungrb.pl" as >
# rungrb.pl filename (name of this file). Add comments with
# "#". Options desired to be THE ONLY ITEM on the line after the
# all-caps keywords. Lines of comments may be placed between them but
# should NOT be after the option/parameter value. Move around the
# commented and uncommented options as desired.

# SECTION: code version - give name of C executable
CCODE
fit_cl

# SECTION: type of model: ism or wind
MODELTYPE
ism
# wind

# CAUTION: CODE EXTENSIONS
# If you want to play with epsilon_B~gamma^x, uncomment these
#
EPBTYPE
noepbofgamma # block this
#epbofgamma # to permit this
#
EPBINDEX # give a floating-point number (generally between -4 and +4)
1.0
#
EPBLIMIT  # =n if desire a growing epB to NOT top out at 100% for some reason
y
```

```
#n
# If you want to play with n~r^S, uncomment these
#
DENSITYPROFILE
n # block any n(r) other than the constant ISM or r^-2 wind
#y
# give a floating-point number > -3. NOT -2 (use Wind option,
# the equations reach a limit here)
NOFRINDEX
0.

# SECTION: model 1st-order corrections

# calculate the inverse Compton cooling and upscattered flux
ICCORR
y
#n

# calculate energy radiative corrections and E(t). Iterated energy is
# at the transition to slow cooling when nu_c = nu_m
NRGCORR
y
#n

# Dealing with the possibility of p < 2. This unbounds the electron
# energy integration at large energies. "epsilon_e" becomes the
# "averaged" value linking the shock Lorentz factor to the electrons'
# average Lorentz factor; average is no longer
# (p-2)*epsilon_e*gamma/(p-1), with epsilon_e the total energy. This
# therefore requires an estimate of the total epsilon_e (fractional,
# <1), and whether it is allowed to be fit. (Not recommended as it
# will only be used in the correction factors for IC cooling and
# E(t)).
EPSELOWP  # value < 1.
0.3
EPELOWPISFIXED
y
#n

# SECTION: fit statistic

# default: on -ln(Probability) = TOTAL( ALOG(sig) + 0.5*( (flux -
# model)/sig )^2 ), sig the uncertainties including interstellar
# scintillation (which is a fraction of the _model_). Proportional to
# chi-squared when there is no scintillation, suppressing the tendency
# to overestimate the model (to get a larger uncertainty and bring
# down chi-squared) when there is scintillation
NEGLNP # overrides below
y
#n

# Otherwise, TOTAL(  ( (flux - model)/sig )^FITINDEX )
FITINDEX
1.7
```

```
# SECTION: extinction law. LMC=roughly LMC's, SMC=steep based on SMC
# bar, MW=from Milky way data.
EXTTYPE
lmc
# smc
# mw


# SECTION: filenames for use by the program

# be sure if two runs are going in the same directory that they are
# kept distinct, or read/write errors will occurs on all save the data
# files.

OUTFILE # parsed output; outname.tmp may be used in an intermediate step
outname

MODFILE # temporary compiled model file to input to the C code
modfile

PARFIXFILE # temporary file to indicate which parameters are fixed
parfixfile

# Data files that must exist in directory used. each is a single column.

NUFILE # frequencies in Hz
nufile

TDFILE # t-tGRB in days
tdfile

FLFILE # fluxes in microJy
flfile

DFFILE # delta-flux
dffile

SCINTFILE # scintillation RMS fractions (of freq, t)
scintfile

SIZEFILE # file to hold sizes of model fit parameter initial stepsizes
sizefile

# to allow finetuned fit statistic, each element can be multiplied by
# its weight from this file. "n" will just give a set of 1's
WGTS
n
#y
WGTFILE # will be used, so have a name
wgtfile

# SECTION: Forward Shock fit parameters. Values must be > 0 in most
# cases, >=0 for such things as host flux, extinction
```

```
# NOTE: will read 2 lines following each allcaps parameter. First must
# be the number, 2nd whether it's fitted

# Following each parameter is then the list of the parameter's initial
# step size in the gradient search - roughly the estimated
# uncertainty you have in your guess.

# Energetics
E52 # isotropic-equivalent, in 10^52 ergs
12.2391
n
#y
# Place ESTEP for each E52
9.79128

THETA # collimation half-angle, radians
0.161635
n
# Place THSTEP for each theta
0.0808175

# Microphysics

PP # electron energy distribution index (< 3.5)
2.78623 2.5
n
# place PSTEP for each p
0.628984 0.1

EPSE # electron energy fraction <= 1.
0.148351 0.3
n
# place EPESTEP for each epe
0.118681 0.15

EPB,PCT # magnetic energy fraction, in %, <= 100
2.18575 5 4
n
# Place EPBSTEP for each epb
1.74860 1 1

# Host properties

ZZ # redshift
2.0369 1.9
n
#y
# place ZSTEP for each z
0.001 0.05

DENSITY # density (for ISM), or A* scale (for wind) or at 1e18 cm (for nofr)
16.2684 3 50
n
```

```
# Place NSTEP for each density scale
13.0147 1 10

HOSTEXT # A(V) magnitudes at host redshift
0.0217765 0.5
n
# place EXTSTEP for each Av
0.0108882 0.1

# Submm host flux: 3 components: flux at 350 GHz (observer frame),
# effective dust temperature T/(1+z), alpha (from 1-2, shape
# parameter) and nuzero (>> submm, sets where the shape is effective)

SUBHOST
0. 10.
n
#y
# Place SUBHSTEP for each submm host flux
1. 5.

TEFF
40.
n
#y
# Place TSTEP for each T/(1+z)
1.

ALPHA
1.5
n
#y
# Place ALPHASTEP for each Alpha
0.1

NUZERO
1e15
n
#y
# Place NUZSTEP for each nuzero
1e14

# Radio host: flux at 1.43 GHz (VLA low frequency band), observer
# frame and spectral index beta (expected < 0, -0.8 fairly canonical)

RADHOST
0.
n
#y
# Place RADHSTEP for each radio host flux
1.

BETA
-0.8
n
```

```
#y
# Place BETASTEP for each beta
0.1

# Optical host components - a more complicated section. First, Y or
# N. Second, lines following OPTHFREQ - the frequencies at which host
# components are desired. Third, lines following OPTHVAL - the
# estimates, Fourth, following OPTHSTEP - the corresponding step
# sizes. Fifth, after OPTHFIT - ys or ns for fitting. if the last 4 do
# not have the same number of lines, an error will occur.


OPTHOST
y
#n
OPTHFREQ
6.871e14
5.499e14
4.673e14
OPTHVAL
0.25 0.211355
0.5
0.224568 0.5 1
#0.205807
OPTHFIT
n
n
n
OPTHSTEP
0.0211355 0.05
0.0205807
0.0224568 0.1 0.1

# cross-calibration uncertainty. Fraction of flux to be added to df's
# for broadband crosscalibration uncertainty

CALUNCERT
0.05
n
#y
# Place CALSTEP for each calib. uncert.
0.01
```

Who cares? It's only a thesis.

—Fiona A. Harrison (1993)